

**MATHEMATICAL MODELS OF AN ELASTOMERIC  
MATERIAL FOR NON-UNIFORM AND  
MULTIAXIAL DEFORMATION CONDITIONS**

By

**DAN LI**

M. Eng., Beijing University of Aeronautics and Astronautics, China, 2002

B. Eng., Beijing University of Aeronautics and Astronautics, China, 1999

A THESIS SUBMITTED IN PARTIAL FULFILLMENT OF  
THE REQUIREMENTS FOR THE DEGREE OF

**MASTER OF APPLIED SCIENCE**

in

THE FACULTY OF GRADUATE STUDIES

(Department of Materials Engineering)

THE UNIVERSITY OF BRITISH COLUMBIA

February 2005

© Dan Li, 2005

## **ABSTRACT**

The goal of this research project is to develop mathematical constitutive models to predict the stable mechanical behaviour of elastomeric materials for non-uniform and/or multiaxial deformation conditions at low or medium strain (<100%) and with a low strain rate.

This study required a series of characterization tests for elastomers in standard deformations modes. These experimental data were used to fit the standard Mooney-Rivlin strain energy function. A series of characterization tests for a silicone elastomer were completed at UBC and correlated to material characterization data provided by Ballard Power Systems, Inc. The experimental data showed that material response changes with the maximum strain experienced and deformation mode. The material constants in the Mooney-Rivlin strain energy function were fitted by regression analysis according to the results of the characterization tests. For each individual strain level and deformation mode, the resulting material constants are unique.

A constitutive model was developed by applying the standard Mooney-Rivlin constitutive model with novel techniques incorporating the maximum strain experienced and the deformation mode. The techniques are a non-uniform strain and a strain partitioning technique. The non-uniform strain technique was expected to give better results for a component experiencing non-uniform strain conditions. The strain partitioning technique eliminates the need of determining the deformation mode before an analysis. Together, these techniques were expected to provide more realistic deformation predictions for elastomeric materials experiencing non-uniform and multiaxial deformation.

Two mechanical tests were designed to provide the data necessary to validate the non-uniform strain and strain partitioning techniques. The first test, a tapered dogbone sample, exhibited varying amounts of uniaxial tension deformation within the gauge-length area, when stretched. The second test, a cross sample, exhibited varying multiaxial deformations when loaded in two perpendicular directions with different amounts of

displacements. The predictions from the mechanical models incorporating the proposed constitutive models as an input agree with experimental data in these two tests, which validates the applicability of the proposed techniques. These techniques will aid in understanding the stable response of elastomeric materials used for seals in fuel cells. Developing an improved understanding of the deformation response will help in predicting seal integrity and improve the overall reliability of PEM fuel cells.

# Table of Contents

ABSTRACT .....	II
TABLE OF CONTENTS.....	IV
LIST OF TABLES .....	VII
LIST OF FIGURE .....	VIII
ACKNOWLEDGMENTS.....	XIII
<b>1 INTRODUCTION.....</b>	<b>1</b>
1.1 PROPERTIES OF ELASTOMERS.....	1
1.2 USE OF ELASTOMERS IN FUEL CELLS .....	2
<b>2 LITERATURE REVIEW .....</b>	<b>4</b>
2.1 MECHANICAL DEFORMATION BEHAVIOUR .....	4
2.1.1 <i>Basic Behaviour of Elastomeric Material</i> .....	4
2.1.2 <i>Effects of Loading Variables</i> .....	6
2.1.2.1 Multi-Cycle Behaviour.....	7
2.1.2.2 Temperature.....	8
2.1.2.3 Time-dependent Behaviour .....	8
2.2 CONSTITUTIVE MODELS OF ELASTOMERIC MATERIAL DEFORMATION .....	10
2.2.1 <i>Statistical Constitutive Models</i> .....	11
2.2.1.1 Gaussian Statistics.....	11
2.2.1.2 Non-Gaussian Statistics.....	12
2.2.2 <i>Phenomenological Constitutive Models</i> .....	16
2.2.3 <i>Other Considerations for Constitutive Models</i> .....	19
2.2.3.1 Compressibility .....	19
2.2.3.2 Mullins Effect and Time-dependence.....	20
2.2.3.3 Model Stability.....	21
2.3 SUMMARY .....	22
<b>3 SCOPE AND OBJECTIVES.....</b>	<b>23</b>
3.1 SCOPE OF THE RESEARCH PROJECT .....	23
3.2 OBJECTIVES OF THE RESEARCH PROJECT .....	24
<b>4 ELASTOMER CHARACTERIZATION.....</b>	<b>25</b>
4.1 INDUSTRIAL EXPERIMENTAL MEASUREMENT.....	25
4.1.1 <i>Uniaxial Tension</i> .....	25

4.1.2	<i>Equibiaxial Tension</i> .....	28
4.1.3	<i>Planar Tension</i> .....	29
4.1.4	<i>Material Constant Evaluation for Industrial Characterization Tests</i> .....	31
4.1.4.1	Material Constant Evaluation for Uniaxial Tension .....	31
4.1.4.2	Material Constant Evaluation for Equibiaxial Tension.....	34
4.1.4.3	Material Constant Evaluation for Planar Tension.....	36
4.2	ON-SITE EXPERIMENTAL MEASUREMENTS.....	39
4.2.1	<i>Uniaxial Tension</i> .....	39
4.2.2	<i>Material Constant Evaluation for UBC Experimental Measurement</i> .....	42
4.2.2.1	Material Constant Evaluation for Uniaxial Tension .....	42
4.2.2.2	Material Constant Estimation for Equibiaxial Tension and Planar Tension.....	45
4.3	SUMMARY .....	50
<b>5</b>	<b>EXPERIMENTAL MEASUREMENTS.....</b>	<b>51</b>
5.1	UNIAXIAL TENSION TEST FOR TAPERED DOG-BONE SAMPLE .....	51
5.1.1	<i>Testing Method</i> .....	51
5.1.2	<i>Experimental Results</i> .....	53
5.2	BIAXIAL TENSION TEST FOR CROSS SAMPLE.....	56
5.2.1	<i>Testing Method</i> .....	56
5.2.2	<i>Experimental Results</i> .....	60
5.3	SUMMARY .....	65
<b>6</b>	<b>MODEL DEVELOPMENT.....</b>	<b>66</b>
6.1	GENERAL MECHANICAL MODEL FORMULATION .....	67
6.2	NON-UNIFORM STRAIN TECHNIQUE .....	68
6.3	STRAIN PARTITIONING TECHNIQUE .....	70
6.3.1	<i>Multiple Partitioned Results</i> .....	73
6.3.2	<i>Equivalent Deformation Modes</i> .....	74
6.3.3	<i>Example Application of Strain Partitioning Technique</i> .....	75
6.4	SUMMARY .....	77
<b>7</b>	<b>MODEL APPLICATION AND VALIDATION .....</b>	<b>78</b>
7.1	TENSILE TEST OF A TAPERED DOGBONE SAMPLE .....	78
7.1.1	<i>Mesh</i> .....	78
7.1.2	<i>Initial and Boundary Conditions</i> .....	79
7.1.3	<i>Predictions and Comparisons to Measured Data</i> .....	79
7.2	BIAXIAL TEST OF A CROSS SAMPLE .....	85
7.2.1	<i>Mesh</i> .....	85
7.2.2	<i>Initial and Boundary Conditions</i> .....	86

7.2.3	<i>Predictions and Comparisons to Measured Data</i> .....	86
7.2.4	<i>Discussion of Cross Sample Results</i> .....	91
7.2.4.1	Effect of Crosswise Displacement.....	91
7.2.4.2	Effect of Crosswise Grip .....	93
7.3	SUMMARY .....	97
<b>8</b>	<b>SUMMARY AND CONCLUSIONS</b> .....	<b>98</b>
8.1	RECOMMENDATIONS FOR FUTURE WORK.....	100
	<b>REFERENCES</b> .....	<b>102</b>
	<b>APPENDIX</b> .....	<b>105</b>

## *List of Tables*

Table 4-1 Mooney-Rivlin material constants for the Ballard uniaxial tension tests at different strain levels.....	32
Table 4-2 Comparison of the comparative importance of strain energy components (Ballard uniaxial tension).....	32
Table 4-3 Mooney-Rivlin material constants for the Ballard equibiaxial tension tests at different strain levels.....	34
Table 4-4 Comparison of the comparative importance of strain energy components (Ballard equibiaxial tension).....	35
Table 4-5 Mooney-Rivlin material constants for the Ballard planar tension tests of at different strain levels.....	37
Table 4-6 Mooney-Rivlin material constants for UBC uniaxial tension tests at different strain levels.....	43
Table 4-7 Comparison of the comparative importance of strain energy components (UBC uniaxial tension) .....	43
Table 4-8 Scale factor for Ballard – UBC uniaxial tension data conversion at different strain levels.....	46
Table 4-9 Estimated Mooney-Rivlin equibiaxial tension material constants at different strain levels for silicone tested at UBC .....	48
Table 4-10 Estimated Mooney-Rivlin planar tension material constants at different strain levels for silicone tested at UBC.....	49
Table 5-1 Summary of accomplished tests in biaxial tension of cross sample.....	61

## *List of Figures*

Figure 1-1 Basic repeating structural unit for a silicone elastomer .....	1
Figure 1-2 A typical PEM fuel cell <sup>5</sup> .....	2
Figure 2-1 Schematic illustrations of deformation modes <sup>7</sup> .....	5
Figure 2-2 Typical elastomer stress-strain data sets under different deformation modes <sup>8</sup> .....	6
Figure 2-3 Cyclic Loading of Filled Natural Rubber <sup>8</sup> .....	7
Figure 2-4 Temperature effects on repeat loading data <sup>12</sup> .....	8
Figure 2-5 Building an equilibrium stress-strain curve from viscoelastic decay data at multiple strain levels <sup>12</sup> .....	9
Figure 2-6 Strain rate effects on an elastomer <sup>15</sup> .....	10
Figure 2-7 Network structure of three-chain constitutive model in undeformed state, uniaxial state, and equibiaxial tension <sup>17</sup> .....	13
Figure 2-8 Network structure of four-chain constitutive model in undeformed state, uniaxial state, and equibiaxial tension <sup>17</sup> .....	13
Figure 2-9 Network structure of eight-chain constitutive model in undeformed state, uniaxial state, and equibiaxial tension <sup>17</sup> .....	14
Figure 2-10 Comparison of the nominal stress-stretch correlations of the Gaussian constitutive model and the non-Gaussian eight-chain constitutive model to uniaxial experimental data <sup>1,17</sup> .....	15
Figure 2-11 Comparison of the nominal stress-stretch correlations of the Mooney-Rivlin constitutive model and experimental data for an elastomer in uniaxial tension <sup>17</sup> .....	17
Figure 2-12 Comparison between nominal stress – stretch ( $\bar{I}_1 - \lambda_1$ ) predictions and experimental data for a natural rubber under cyclic uniaxial tension.....	20
Figure 2-13 Comparison between predictions and experimental data for a Chloroprene rubber with 15 vol% carbon black under cyclic uniaxial compression at different strain rates <sup>16</sup> .....	21
Figure 4-1 Example of a uniaxial tension experiment setup <sup>8</sup> .....	26
Figure 4-2 Cyclic behaviour of a sample in uniaxial tension tests provided by	

Ballard.....	27
Figure 4-3 Stable stress-strain curves for different strain levels in the Ballard uniaxial tension tests.....	27
Figure 4-4 Example of an equibiaxial tension experiment setup <sup>8</sup> .....	28
Figure 4-5 Stable loading curves for different strain levels in the Ballard equibiaxial tension tests.....	29
Figure 4-6 Example of a planar tension experiment setup <sup>8</sup> .....	30
Figure 4-7 Stable loading curves for different strain levels in Ballard planar tension tests.....	30
Figure 4-8 Comparison of measured stress – strain correlations and calculations with the Mooney-Rivlin constitutive model for Ballard uniaxial tension tests at different strain levels.....	33
Figure 4-9 Comparison of measured stress – strain correlations and calculations with the Mooney-Rivlin constitutive model for Ballard equibiaxial tension tests at different strain levels.....	36
Figure 4-10 Comparison of measured stress – strain correlations and calculations with the Mooney-Rivlin constitutive model for Ballard planar tension tests at different strain levels.....	38
Figure 4-11 Material constants evaluated for different testing conditions for the silicone tested by Ballard.....	39
Figure 4-12 Profile of dogbone sample in UBC uniaxial tension tests (unit: mm, sample thickness=1.0mm).....	40
Figure 4-13 Photograph of a uniaxial tension experiment setup at UBC.....	40
Figure 4-14 Marked dogbone sample for the UBC uniaxial tension tests.....	42
Figure 4-15 Stable stress-strain curves for different strain levels in the UBC uniaxial tension tests.....	42
Figure 4-16 Comparison of measured stress – strain correlations and calculations with the Mooney-Rivlin constitutive model for UBC uniaxial tension tests at different strain levels.....	44
Figure 4-17 Comparison of UBC and Ballard measurements for uniaxial tension at 1.0 maximum strain.....	45

Figure 4-18 Comparison of measured UBC data and the scaled Ballard data using the global scale factor in uniaxial tension tests.....	47
Figure 4-19 Material constants evaluated or estimated for different testing conditions for the silicone tested at UBC .....	49
Figure 5-1 Geometry of tapered dogbone sample in UBC uniaxial tension test (unit: mm, Sample thickness=1.0mm).....	52
Figure 5-2 Marked tapered dogbone sample for UBC uniaxial tension tests .....	53
Figure 5-3 Locations of reference lines from where the distances were measured in uniaxial tension of tapered dogbone sample.....	53
Figure 5-4 Force-time profile for a 2.5mm gauge-length displacement in uniaxial tension of tapered dogbone sample.....	54
Figure 5-5 Measured reaction force – displacement results for uniaxial tension of tapered dogbone sample.....	55
Figure 5-6 Measured distances between different reference lines throughout the deformed tapered dogbone sample .....	56
Figure 5-7 Photograph of deformed tapered dogbone sample in uniaxial tension with a 15mm displacement applied to the gauge-length area (marked as g5 in Figure 5-3).....	56
Figure 5-8 Geometry of cross sample in UBC biaxial tension test (unit: mm, Sample thickness=1.0mm).....	57
Figure 5-9 Assembly of the pre-loading grips and the cross sample before testing by the testing machine (unit: inch).....	58
Figure 5-10 Photograph of the biaxial tension experiment setup at UBC .....	59
Figure 5-11 Marked cross sample in biaxial tension .....	59
Figure 5-12 Sample failure in progress in biaxial tension tests .....	62
Figure 5-13 Measured reaction force – displacement results for biaxial tension of cross sample.....	62
Figure 5-14 Photograph of a deformed cross sample in biaxial tension.....	63
Figure 5-15 Measured distances across different reference points throughout the deformed cross samples .....	65
Figure 6-1 Comparison of the measured and the calculated stress-strain curves in	

Ballard uniaxial tension tests .....	69
Figure 6-2 Comparison of measured and calculated stress-strain curves in the Ballard equibiaxial tension tests .....	71
Figure 6-3 Stretch component directions (the subscript U refers to uniaxial tension, B refers to equibiaxial tension and S refers to planar tension) .....	72
Figure 6-4 Equivalent deformation modes .....	75
Figure 7-1 Tapered dogbone sample simplified to a 1/8 <sup>th</sup> section and meshed with 8- node brick elements .....	79
Figure 7-2 Predicted strain distribution employing the non-uniform strain technique within the deformed tapered dogbone sample .....	80
Figure 7-3 Comparison of the predicted deformed tapered dogbone sample profile and the picture.....	81
Figure 7-4 Comparison of the measured deformation and the predicted deformation employing the modified Mooney-Rivlin constitutive model with the non- uniform strain technique for the tapered dogbone sample.....	82
Figure 7-5 Comparison of the measured deformation and the predicted deformation employing the standard and modified Mooney-Rivlin constitutive models for the tapered dogbone sample.....	83
Figure 7-6 Comparison of the measured reaction force and the predicted reaction force employing the standard and modified Mooney-Rivlin constitutive model for the tapered dogbone sample .....	84
Figure 7-7 Cross sample simplified to a 1/4 <sup>th</sup> section and meshed with 8-node brick elements .....	85
Figure 7-8 Predicted strain distribution within the deformed cross sample employing the strain partitioning technique (x-displacement=6mm, y-displacement=30mm) .....	87
Figure 7-9 Comparison of the predicted deformed cross sample profile and the picture (x-displacement=6mm, y-displacement=30mm).....	88
Figure 7-10 Comparison of the measured deformation and the predicted deformation employing the modified Mooney-Rivlin constitutive model with the strain partitioning technique for the cross sample .....	89

Figure 7-11 Comparison of the measured deformation and the predicted deformation employing the different modified Mooney-Rivlin constitutive models for the cross sample .....	90
Figure 7-12 Comparison of the measured reaction force and the predicted reaction force employing the different modified Mooney-Rivlin constitutive models for the cross sample .....	91
Figure 7-13 Comparison of the measured reaction forces and the predicted reaction forces employing the strain partitioning technique for different x-displacements for the cross sample .....	92
Figure 7-14 Geometry of the desired cross sample .....	94
Figure 7-15 Comparison of the predicted reaction forces employing the modified Mooney-Rivlin constitutive models with the non-uniform strain and the strain partitioning techniques individually for the cross sample (x-displacement=6mm) .....	94
Figure 7-16 Predicted strain distribution within the deformed desirable cross sample (x-displacement=6mm, y-displacement=6mm) .....	95
Figure 7-17 Comparison of the predicted reaction forces employing the modified Mooney-Rivlin constitutive models with the non-uniform strain and the strain partitioning techniques individually for the cross sample (x-displacement=6mm) .....	96
Figure A-1 A half of crosswise grip with smooth holes (unit: inch).....	105
Figure A-2 A half of crosswise grip with threaded holes (unit: inch).....	106

## *Acknowledgments*

It is a pleasure to offer my grateful appreciation to many people who have generously assisted in various ways during the completion of my thesis. I would like to thank my supervisor, Dr. Daan Maijer, for his continual guidance and support throughout this project. I am grateful that he participated so diligently in my undertaking. It was wonderful working with him.

I am thankful to MITACS (Mathematics of Information Technology and Complex systems), a Network of Centres of Excellence (NCE), for providing financial support for this research.

I would also like to thank Warren Williams and Robert Artibise from Ballard Power Systems Inc. for their technical support and assistance. I am grateful to Dr. Chad Sinclair and Dr. Rizhi Wang for their help in performing experimental measurements. Without their help, this research will not have been completed.

I would also like to thank my parents and grandparents for their love and encouragement at every stage of my educational career. I am thankful to all my friends. Special thanks to Penglong for his support, patience and love. My family and friends' active role in my development throughout my lifetime has been an inspiration and words cannot begin to fully express my heartfelt gratitude towards them.

# **1 INTRODUCTION**

## ***1.1 PROPERTIES OF ELASTOMERS***

The term “elastomer” is employed when referring to materials having rubber-like properties. The original elastomer was natural rubber obtained in the form of latex from the tree *Hevea Braziliensis*<sup>1</sup>. Elastomers are polymers consisting of interlinked, long chain, flexible macromolecules. Frequently, elastomers are used where toughness or resistance to impact is desired or where elasticity during stretching and recoil are needed. An elastomer can be stretched to many times its original length and will return to its original shape without permanent deformation. The typical applications of elastomers include: tires, mounts and bumpers for vibration and shock prevention, roof and tank linings, curing bladders, soft feed rolls for copiers, automotive engine and transmission seals, gaskets and O-rings weather strips, etc<sup>2</sup>.

This investigation is focused on elastomers used in sealing applications, specifically a candidate silicone seal material for use in fuel cells produced by Ballard Power Systems Inc, where the operational strain is generally low or medium, usually lower than 100% nominal strain. The silicone elastomer has repeating units of silicon and oxygen as shown in Figure 1-1. X and X' may be hydrogen atoms or groups such as methyl (CH<sub>3</sub>-) or phenyl (C<sub>6</sub>H<sub>5</sub>-)<sup>3</sup>. Silicone based elastomers are resistant to high temperature extremes, chemical attack and oxidation which contribute to silicone's attractiveness for the seal applications.

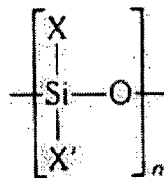


**Figure 1-1 Basic repeating structural unit for a silicone elastomer**

## 1.2 USE OF ELASTOMERS IN FUEL CELLS

Fuel cells are electrochemical devices that convert chemical energy directly into electrical energy, without combustion as an intermediate step<sup>4</sup>. The first practical fuel cell was developed by a Welsh scientist William Grove<sup>4</sup>. In 1839, he discovered that electricity and water were produced by mixing hydrogen and oxygen in the presence of an electrolyte. But fuel cells did not see practical application until 1959, when a practical five-kilowatt fuel cell stack was demonstrated by Bacon<sup>4</sup>. Since then, constant development has led to fuel cells being used in a wide variety of applications.

It should be noted that Canada is one of the world's leading countries in research and development of fuel cell systems. Ballard Power Systems Inc, based in Burnaby, B.C., specializes in research and development of polymer electrolyte membrane (PEM) fuel cells for a diverse range of applications, including buses, cars, and power back-up systems for residential and industrial use. Creating electricity by combining hydrogen and oxygen taken from the air, PEM fuel cells require a membrane, including a catalyst and diffusion media which are layered between two conductive plates. Figure 1-2 shows the structure of a typical fuel cell.

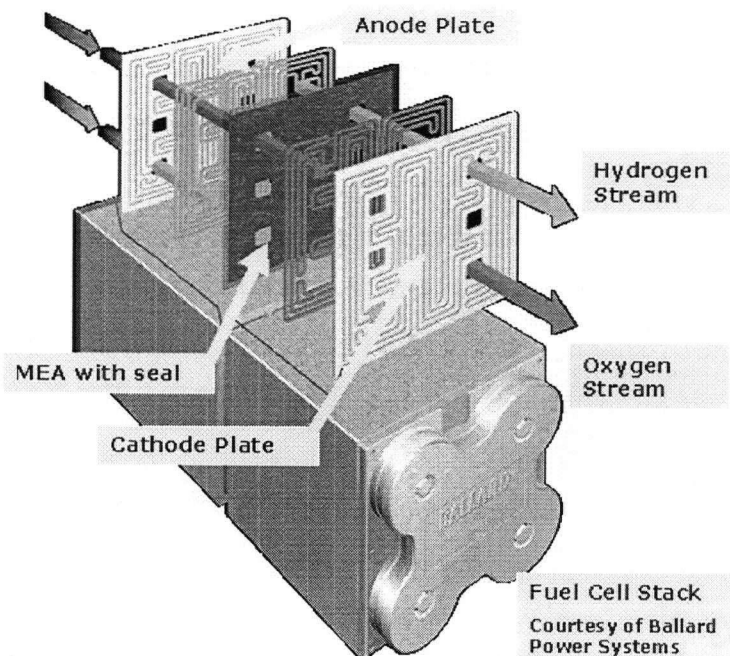


Figure 1-2 A typical PEM fuel cell<sup>5</sup>

In PEM fuel cells, hydrogen is channelled to the anode (which in practice is a thin layer of catalyst on the MEA surface) and oxygen is channelled to the cathode (which is on the other side of the MEA surface). At the anode, hydrogen is split into protons and negatively charged electrons. The membrane allows only protons to pass through it to the cathode, where water is formed as the product. Electrons travel to the cathode via an external circuit, creating an electrical current<sup>6</sup>. Typically PEM fuel cells operate at a temperature of 80°C and a gas pressure of 0.285MPa nominally, and a range of 0.1 to 1.0 MPa<sup>5</sup>.

Hydrogen is a difficult gas to store and contain. Fuel leakage could be extremely dangerous if hydrogen pools around potential sources of ignition. Consequently, seals are a critical component of fuel cells because they separate the gas streams (fuel and exhaust) and prevent venting of gas to the environment. Their performance affects the lifetime of a fuel cell and is an important factor in commercializing fuel cells.

One of the challenges facing fuel cell designs is predicting seal integrity under long-term cyclic operational conditions. Since the deformation behavior of elastomeric materials is very complex, this long term goal must be preceded by an initial goal to understand the stable (or equilibrium) response of seals to mechanical loading, where time dependence is not considered. Once the basic deformation behaviour is understood, the time-dependent response of seal materials to mechanical loading can be considered. Finally the mechanism of seal mechanical failure should be investigated. In this investigation, the equilibrium response of seal materials to mechanical loadings is studied as the initial step towards the long term goal.

## **2 LITERATURE REVIEW**

Mechanical deformation of elastomers under arbitrary loading conditions is complicated by the fact that loading variables such as deformation mode, maximum strain experienced, number of loading cycles at a strain level, relaxation, strain rate and temperature will affect the overall elastomer behaviour. A review of the literature relevant to the mechanical deformation of elastomeric materials is presented in this chapter, followed by constitutive material models pertinent to the material deformation.

### ***2.1 MECHANICAL DEFORMATION BEHAVIOUR***

In order to characterize constitutive properties of elastomeric materials, usually several simple standard tests are performed. The constitutive material properties obtained from these simple characterization tests are extrapolated to more complicated cases. In this section, the basic behaviour of elastomer materials in standard tests is presented and followed by a discussion of the effects of specific loading variables.

#### ***2.1.1 Basic Behaviour of Elastomeric Material***

It is often impractical or impossible to characterize an elastomeric material under loading conditions which are identical to those experienced during operation. Instead, the material response is typically characterized via a small number of simple mechanical tests. There are four standard test configurations for elastomeric material behaviour characterization:

- Uniaxial test
- Equibiaxial test
- Planar test
- Volumetric test

Each of these tests can be run in tension or compression as shown in Figure 2-1. For incompressible elastomers, the basic tests are simple tension, equibiaxial tension and planar tension<sup>7</sup>. Usually data from these three tests are combined to characterize the elastomeric material behaviour.

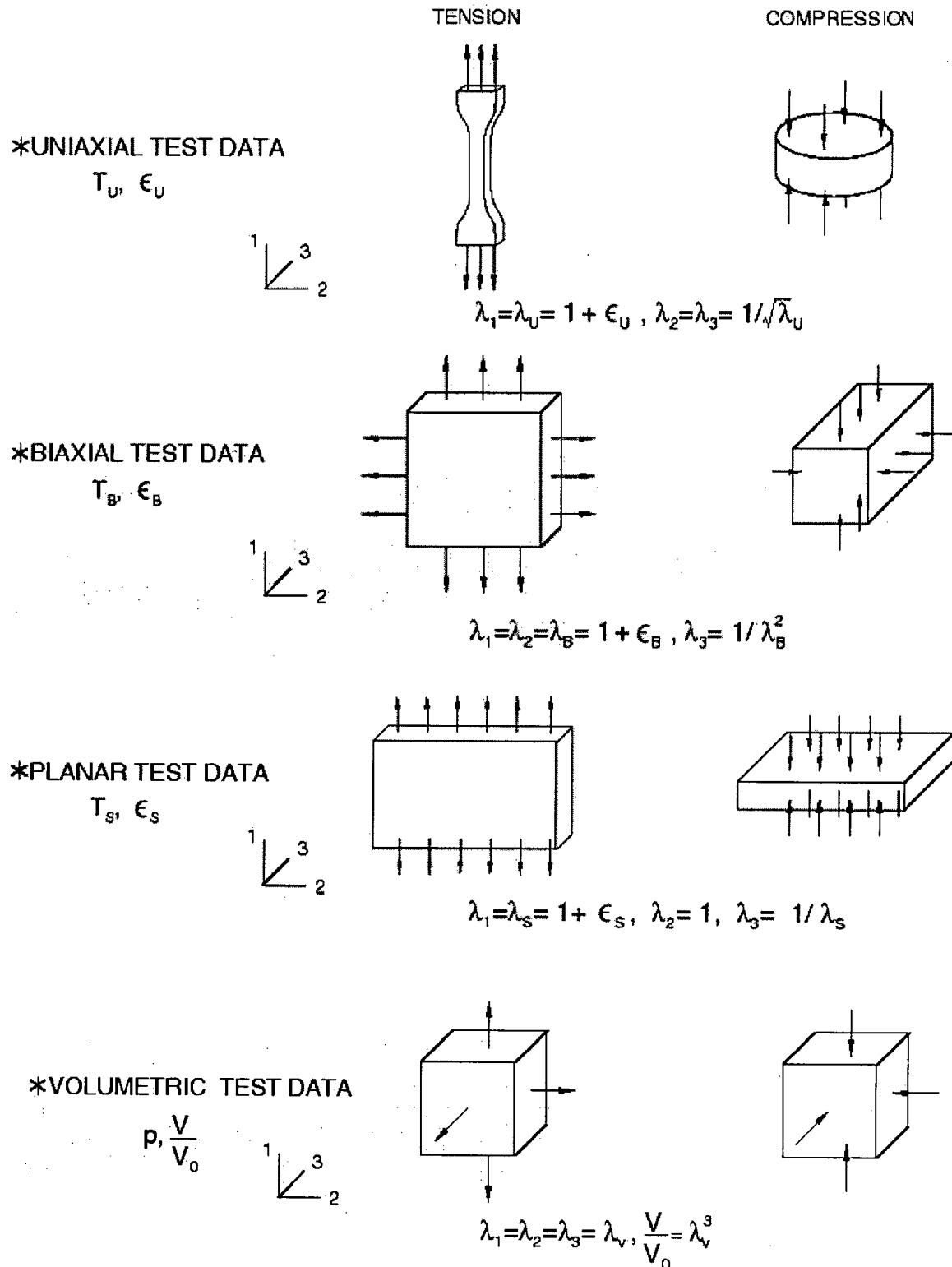


Figure 2-1 Schematic illustrations of deformation modes<sup>7</sup>

In Figure 2-1, the principal stretches,  $\lambda_1$ ,  $\lambda_2$ , and  $\lambda_3$ , are the ratios of current length to

original length in the principal directions of a material sample. The principal stretches are related to the nominal principal strains,  $\varepsilon_i$ , by

$$\lambda_i = 1 + \varepsilon_i \quad i=1, 2, 3 \quad \text{Eq 2-1}$$

In the three standard tests, elastomeric materials exhibit hyperelastic material behaviour, which refers to large, fully recoverable elastic deformation. When loaded, shown in Figure 2-2, elastomeric materials exhibit large elastic deformations and a nonlinear stress-strain relationship as. The impact of deformation mode on elastomeric material response is also shown in Figure 2-2. At the same strain level, an elastomeric material will show the highest stress in the equibiaxial tension test, followed by planar tension and uniaxial tension.

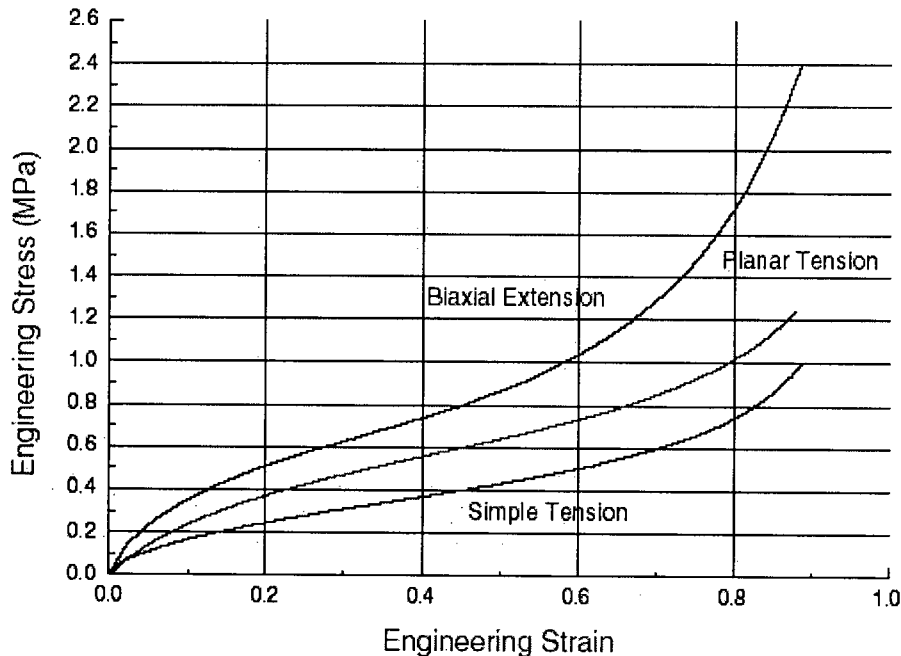


Figure 2-2 Typical elastomer stress-strain data sets under different deformation modes<sup>8</sup>

### 2.1.2 Effects of Loading Variables

The effects of loading variables on elastomeric material behaviour are discussed in this section. These effects must be considered in order to construct general constitutive models for elastomeric materials valid for specific deformation states.

### 2.1.2.1 Multi-Cycle Behaviour

The stress-strain curves demonstrated in Figure 2-2 are examples of stable material behaviour. Under cyclic loading, the stress-strain response of elastomeric materials evolves as a function of the number of cycles. A stable behaviour is eventually achieved after a number of loading cycles, i.e. loading a sample to a particular strain level followed by complete unloading to zero stress several times. The properties of elastomers change significantly during the first several repetitions. This behaviour is commonly referred to as the Mullins effect<sup>9</sup>. As an elastomeric material is loaded and unloaded, the cycle to strain="8.0">EndNote</source-app><rec-number>4</rec-number><ref-type name="Electronic Journal">43</ref-type><contributors><authors><author><style face="normal" font="default" size="100%">Mikko Mikkola</style></author></authors></contributors><titles><terial response. Figure 2-3 demonstrates a typical multi-cycle behaviour, where a filled natural rubber is strained to 40% strain

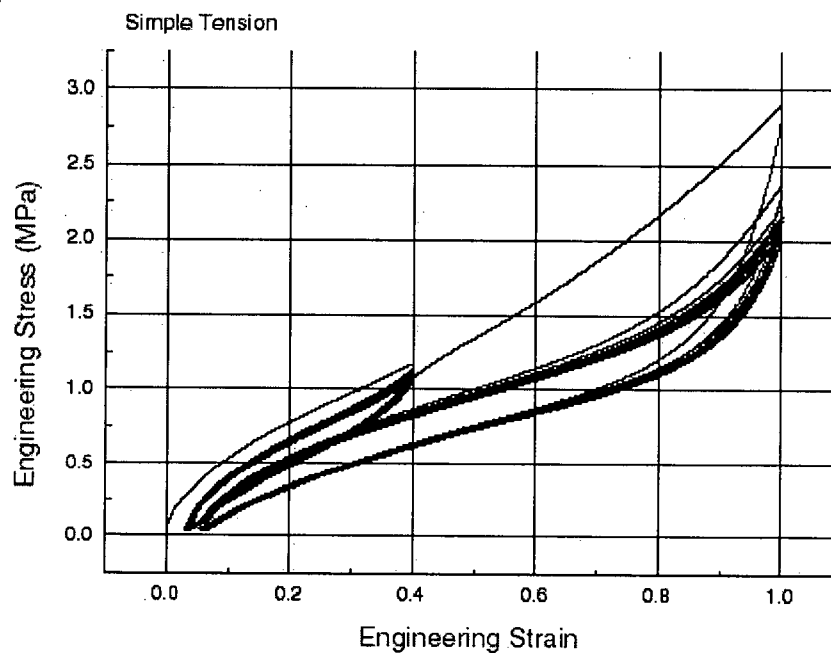


Figure 2-3 Cyclic Loading of Filled Natural Rubber<sup>8</sup>

There is no unanimous explanation of the physical causes of the Mullins effect in elastomeric materials. Mullins and Tobin<sup>10</sup> assumed that the material consists of two phases, soft and hard. During deformation, hard regions are broken down and

transformed into soft regions. However, they did not provide a physical interpretation for this reasoning. The physical justification for the two phase assumption was discussed by Johnson and Beatty<sup>11</sup>. They suggested that the hard phase could be interpreted as clusters of molecular chains held together by short chain segments, entanglements or intermolecular forces. As the material is deformed, chains are pulled from clusters and hard regions are transformed into soft regions.

### 2.1.2.2 Temperature

Temperature affects molecular motion and therefore affects the mechanical behaviour of elastomers. Elastomeric material responses at different temperatures can be dramatically different. The stress-strain behaviour for an elastomeric material, commonly used in an automotive power train, experiencing the same uniaxial loading sequence at two different temperatures is shown in Figure 2-5. At 23°C, the material exhibits a typical elastomeric material response. However, at -40°C, this material stops behaving like an elastomer as it experiences localized plastic straining and shows virtually no recovery.

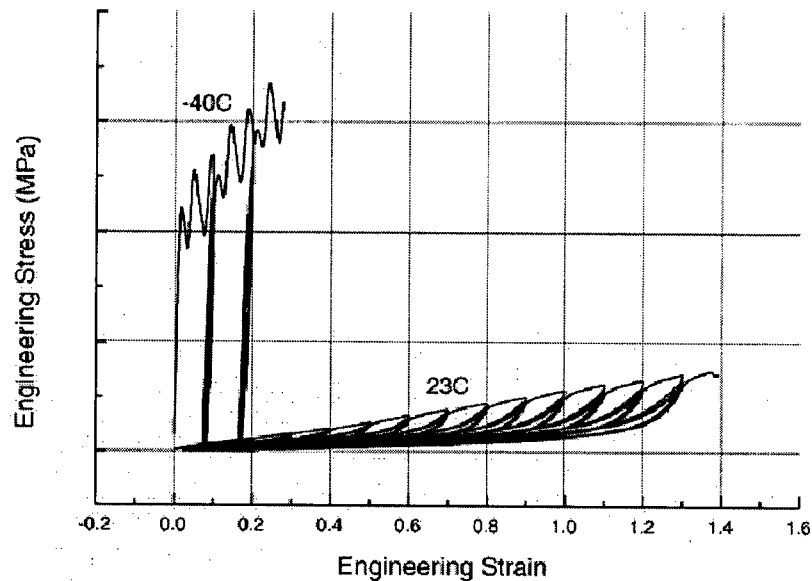


Figure 2-4 Temperature effects on repeat loading data<sup>12</sup>

### 2.1.2.3 Time-dependent Behaviour

For an elastomeric material, complicated molecular rearrangements underlie any macroscopic mechanical deformation<sup>13</sup>. Rearrangements on a local scale are relatively

rapid and on a long range scale very slow. The stress-strain behavior of elastomeric materials is strongly dependent on time. The time dependence results in numerous experimentally observed phenomena. The hysteresis during cyclic loading shown in Figure 2-3 is an example. Stress relaxation and rate-dependence are also observed in experimental investigations as time-dependent behaviours.

When an elastomeric material sample is stretched to a particular strain and the deformation is held, the stress will decrease with time, which is called stress relaxation. This response is described as viscoelastic decay. Figure 2-5 shows a group of stress-time data sets showing the change in stress over time for a series of silicone samples at different strain levels in uniaxial tension. The equilibrium stress at each strain level, shown in the insert graph of Figure 2-5, is defined by the final relaxed stress level. An equilibrium stress-strain curve can be developed from the viscoelastic decay data. Usually the equilibrium material response is desirable to characterize stable material response independent of time.

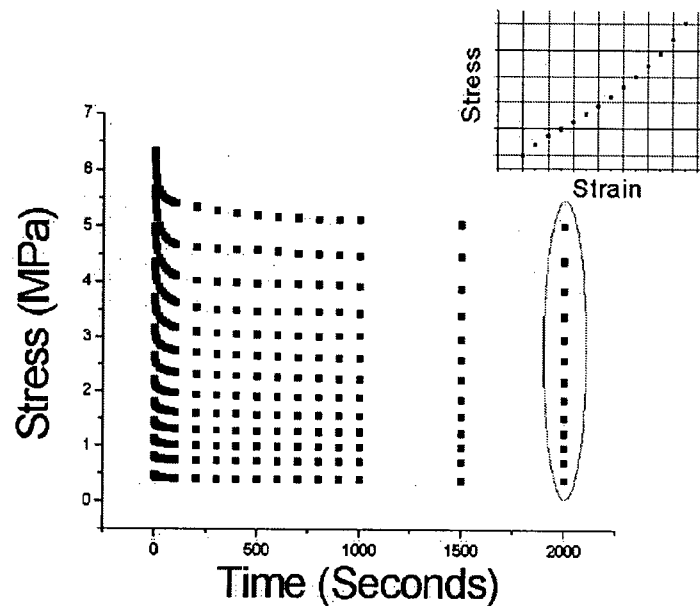


**Figure 2-5 Building an equilibrium stress-strain curve from viscoelastic decay data at multiple strain levels<sup>12</sup>**

Elastomeric materials exhibit strain rate sensitivity which can be related to a time-

dependent behaviour. Figure 2-6 shows the effect of strain rate on a rubber experiencing simple shear deformation. Higher strain rates limit the time for molecular motion, resulting in higher forces for a given strain and larger hysteresis loops. The magnitude of the hysteresis loop strongly depends on strain rate<sup>14</sup>.

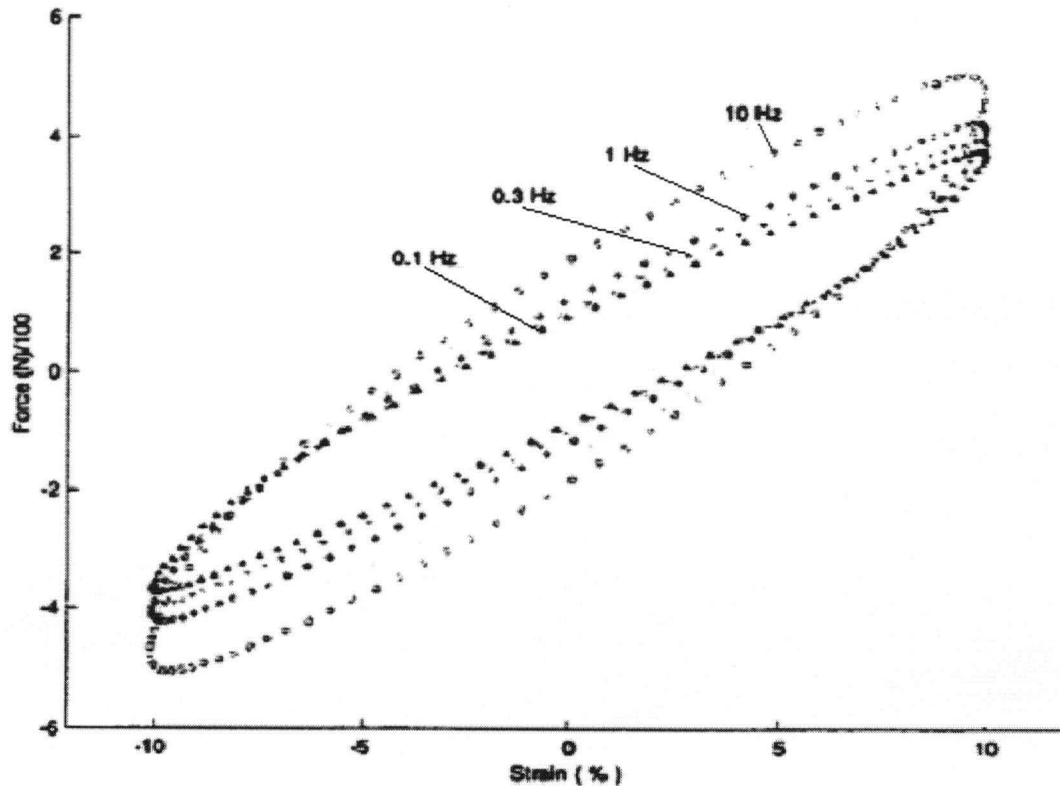


Figure 2-6 Strain rate effects on an elastomer<sup>15</sup>

## 2.2 CONSTITUTIVE MODELS OF ELASTOMERIC MATERIAL DEFORMATION

The stress-strain behavior of elastomeric materials is strongly dependent on time. However, few models attempt to quantify the time-dependence perhaps due to the complex nature of this behaviour. Most proposed models are equilibrium models, corresponding to equilibrium material response at infinitely slow loading rate<sup>16</sup>. Though equilibrium material response is related to infinitely slow loading rate, in practice slow loading rate is used to obtain equilibrium material behaviour.

As elastomeric materials exhibit highly nonlinear behaviour, the application of Hooke's law is inappropriate. Instead, equilibrium elastomeric material behaviour is typically characterized by energy based constitutive models. Most equilibrium constitutive models for elastomeric materials are described in terms of a "strain energy function",  $W$ , which defines the strain energy stored in the material per unit of reference volume (volume in the initial configuration)<sup>7</sup>. The equilibrium constitutive models can be classified into two categories<sup>17</sup>: statistical and phenomenological constitutive models.

Usually the constitutive models are expressed using the principal stretches, which can be obtained from the principal strains. Given a general strain tensor, the principal strains are the three eigenvalues of the strain tensor.

### 2.2.1 Statistical Constitutive Models

This group of constitutive models was developed by considering the physics of the elastomer network<sup>1</sup>. First, conformations of a single polymer chain are determined; then, the behaviour of the whole network is derived using statistical methods. If only moderate extensions are involved, Gaussian statistics is sufficient. But for the higher range of extensions this method is inadequate as the distance between the two ends of the chain approaches the fully extended length, and a more elaborate non-Gaussian statistics should be used.

#### 2.2.1.1 Gaussian Statistics

Considering only moderate extensions, it is assumed that an elastomer consists of randomly-oriented long molecular chains. The chains have  $n$  links of equal length  $l$ . The distance  $r$  between the ends of the chain is not comparable with the maximum or fully extended length of the chain  $nl$  (i.e.  $r \ll nl$ ). Then, based on Gaussian statistics<sup>1</sup>, distribution of  $r$  is given by  $P(r)$ :

$$P(r) = (4b^3 / \pi^2)^{1/2} r^2 \exp(-b^2 r^2) \quad \text{Eq 2-2}$$

where  $b^2 = 3/2nl^2$

Considering the general case of a homogeneous strain applied to an assembly of  $N$  chains,  $W$ , is derived from the change in configurational entropy, which is related to the distribution of  $r$ :

$$W = \frac{1}{2} NkT(\lambda_1^2 + \lambda_2^2 + \lambda_3^2 - 3) \quad \text{Eq 2-3}$$

where  $k$  is Boltzmann's constant ( $1.38 \times 10^{-23} \text{ J K}^{-1}$ ) and  $T$  is absolute temperature.

Once the form of the strain energy function is determined, the stress-strain correlations can be found. For an incompressible material, the principal true stress,  $\sigma_i$ , can be derived by differentiating with respect to the principal stretch,  $\lambda_i$ :

$$\sigma_i = \lambda_i \frac{\partial W}{\partial \lambda_i} + p \quad i=1, 2, 3 \quad \text{Eq 2-4}$$

where  $p$  is the pressure determined by satisfying boundary conditions. The corresponding nominal stress is given by

$$f_i = \frac{1}{\lambda_i} \sigma_i \quad i=1, 2, 3 \quad \text{Eq 2-5}$$

### 2.2.1.2 Non-Gaussian Statistics

In the Gaussian statistics, chains are assumed to be randomly-oriented. However, this assumption is not valid for networks experiencing large extensions or with short chains. For these cases, a non-Gaussian statistics becomes essential. The non-Gaussian statistics takes into account the finite extensibility of the network. The solution of this method was first investigated in the 1940's<sup>1</sup>. For a single chain, the distribution  $P(r)$  of an end-to-end distance  $r$  irrespective of direction in space is obtained:

$$P(r) = 4\pi r^2 \exp(\text{constant} - n(\frac{r}{nl} \beta + \ln \frac{\beta}{\sinh \beta})) \quad \text{Eq 2-6}$$

where  $\beta$  is equal to  $\mathcal{L}^{-1}(\frac{r}{nl})$ . The inverse Langevin function,  $\mathcal{L}^{-1}(\frac{r}{nl})$ , is defined as follows:

$$\frac{r}{nl} = \coth \beta - \frac{1}{\beta} = \mathcal{L}(\beta) \quad \text{Eq 2-7}$$

In order to relate the individual chain statistics to a network, it is necessary to define the network structure. The simplest is the three-chain network structure<sup>1,18</sup> shown in Figure 2-7. The network structure of the three-chain constitutive model does not provide a cooperative deformation as the three chains are independent. A more realistic network structure is the four-chain structure<sup>1,19</sup>. In this structure, four chains are linked from a common junction point as shown in Figure 2-8. The tetrahedron deforms more cooperatively as the chains stretch and rotate with the imposed deformation on the tetrahedron. Unfortunately, the change of structural entropy in this network must be calculated using an iterative numerical method to satisfy equilibrium. Thus, there is not a simple expression to define the strain energy function.

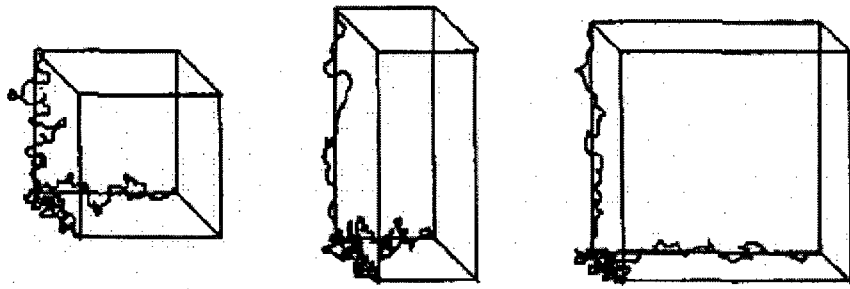


Figure 2-7 Network structure of three-chain constitutive model in undeformed state, uniaxial state, and equibiaxial tension<sup>17</sup>

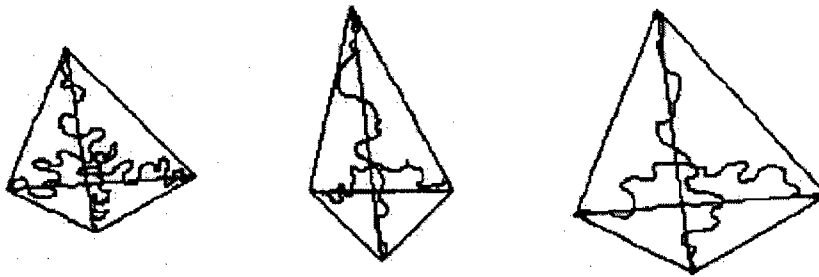


Figure 2-8 Network structure of four-chain constitutive model in undeformed state, uniaxial state, and equibiaxial tension<sup>17</sup>

More recently, an eight chain network structure was developed<sup>17,20</sup>. As demonstrated in Figure 2-9, the eight chains are linked at the center of a cubic cell. The interior junction point remains at the centroid during deformation and the stretch of each chain is the root

mean-square of the applied stretches. This structure deforms cooperatively and symmetry results in a very simple expression for the strain energy function:

$$W = NkT\sqrt{n}[\beta_{chain}\lambda_{chain} + \sqrt{n}\ln(\frac{\beta_{chain}}{\sinh\beta_{chain}})] \quad \text{Eq 2-8}$$

where

$$\lambda_{chain} = (\frac{1}{3}(\lambda_1^2 + \lambda_2^2 + \lambda_3^2))^{\frac{1}{2}}$$

$$\beta_{chain} = \mathcal{L}^{-1}(\frac{\lambda_{chain}}{\sqrt{n}})$$

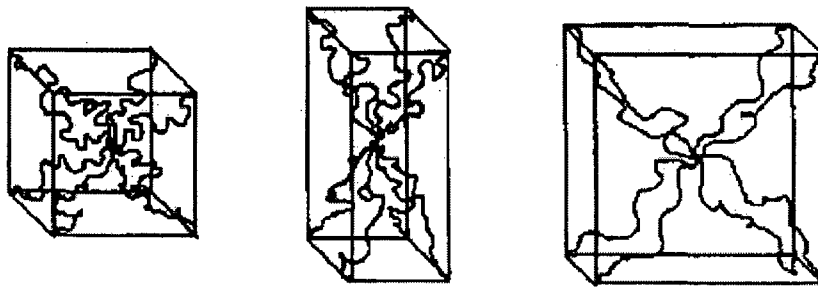


**Figure 2-9 Network structure of eight-chain constitutive model in undeformed state, uniaxial state, and equibiaxial tension<sup>17</sup>**

The theoretical nominal stress-stretch correlations given by the Gaussian statistics and the non-Gaussian eight-chain statistics are compared with uniaxial tension experimental data in Figure 2-10. The Gaussian statistics gives acceptable agreement with the experimental data only at low strains. The eight-chain model provides a much better representation of the experimental data, capturing the S-shape of the actual stress-stretch behaviour over the entire test range.

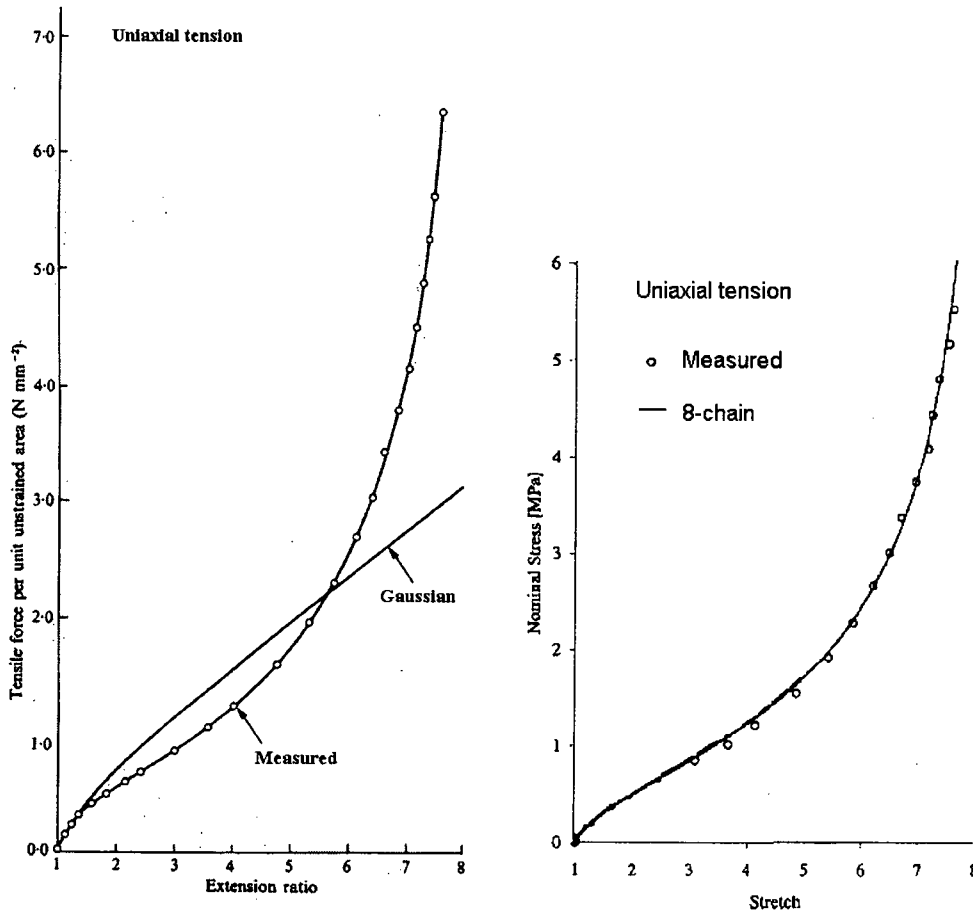


**Figure 2-10** Comparison of the nominal stress-stretch correlations of the Gaussian constitutive model and the non-Gaussian eight-chain constitutive model to uniaxial experimental data <sup>1,17</sup>

The use of these statistical constitutive models reduces the number of relevant material parameters because of their physical foundations, but their mathematical derivations are very complicated. Though the constitutive models based on the non-Gaussian statistics give a satisfactory representation of the experimental data compared with the Gaussian constitutive model, they have an inherent drawback in their use of the inverse Langevin function in the strain energy function expression. The function,  $\mathcal{L}^{-1}\left(\frac{r}{nl}\right)$ , may be expanded in series form to give<sup>1</sup>:

$$\mathcal{L}^{-1}\left(\frac{r}{nl}\right) = 3\left(\frac{r}{nl}\right) + \frac{9}{5}\left(\frac{r}{nl}\right)^3 + \frac{297}{175}\left(\frac{r}{nl}\right)^5 + \frac{1539}{875}\left(\frac{r}{nl}\right)^7 + \dots \quad \text{Eq 2-9}$$

When strains approach the limiting extension of the network, i.e.  $r$  approaching  $nl$ , the

higher order terms in Equation 2-9 can not be omitted. With increasing strain, computation expense increases rapidly owing to the number of terms necessary to describe the behaviour adequately.

### 2.2.2 Phenomenological Constitutive Models

Phenomenological constitutive models are developed with experimental observations and phenomenological considerations. These constitutive models are both mathematically simple and quite efficient. Most phenomenological constitutive models<sup>1, 21-26</sup> assume that the material is isotropic and that a strain energy,  $W$ , can be defined of the form:

$$W = f(I_1, I_2, I_3), \quad \text{Eq 2-10}$$

where  $I_1$ ,  $I_2$  and  $I_3$  are the strain invariants defined as:

$$I_1 = \lambda_1^2 + \lambda_2^2 + \lambda_3^2, \quad I_2 = \lambda_1^2 \lambda_2^2 + \lambda_2^2 \lambda_3^2 + \lambda_3^2 \lambda_1^2, \quad I_3 = \lambda_1^2 \lambda_2^2 \lambda_3^2.$$

For an incompressible material,  $I_3$  is equal to 1, thus  $I_2$  can be rewritten as  $I_2 = \lambda_1^{-2} + \lambda_2^{-2} + \lambda_3^{-2}$ .

In theory, the strain energy function may be any one of a number of possible mathematical functions<sup>1</sup>. Several forms for the strain energy function of elastomeric materials have been proposed since 1940. One general representation proposed by Rivlin<sup>27</sup> is given by:

$$W = \sum_{i+j=1}^N C_{ij} (I_1 - 3)^i (I_2 - 3)^j \quad \text{Eq 2-11}$$

where  $C_{ij}$  are material constants. When only the first term is retained, this general expression is referred to as the neo-Hookean constitutive model:

$$W = C_{10} (I_1 - 3) \quad \text{Eq 2-12}$$

It should be noted that the neo-Hookean constitutive model is equivalent to the Gaussian constitutive model expressed as Equation 2-3 where  $C_{10} = \frac{1}{2} NkT$ .

Mooney<sup>23</sup> developed a constitutive model commonly referred to as the Mooney-Rivlin constitutive model by using two terms in the general Rivlin expression.

$$W = C_{10}(I_1 - 3) + C_{01}(I_2 - 3) \quad \text{Eq 2-13}$$

The Mooney-Rivlin constitutive model has been extensively applied in studies of elastomer deformation. A comparison of Mooney-Rivlin constitutive model predictions and experimental data for an elastomer in uniaxial tension is shown in Figure 2-11. Up to 200% stretch, the Mooney-Rivlin prediction provides a good agreement with the experimental data. While the Gaussian prediction, as shown in Figure 2-10 for the same material, is good only up to 150% stretch. However, for higher strains, this constitutive model fails in representing the S-shape constitutive behaviour exhibited by most elastomers.

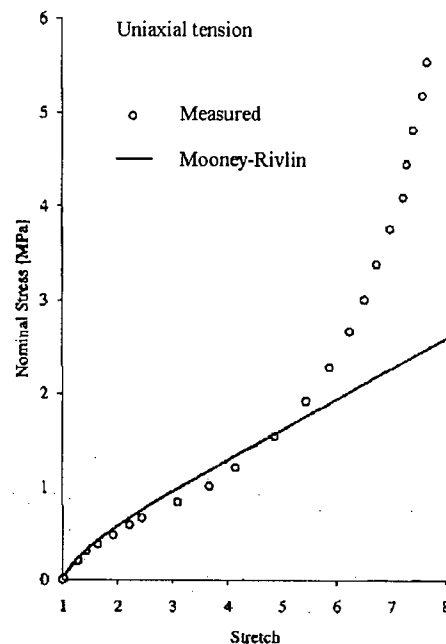


Figure 2-11 Comparison of the nominal stress-stretch correlations of the Mooney-Rivlin constitutive model and experimental data for an elastomer in uniaxial tension<sup>17</sup>

One drawback of the Mooney-Rivlin constitutive model is the resulting constant shear modulus. Yeoh<sup>26</sup> developed a higher order strain energy function with a shear modulus that varies with deformation. This model is referred as the Yeoh constitutive model:

$$W = C_{10}(I_1 - 3) + C_{20}(I_1 - 3)^2 + C_{30}(I_1 - 3)^3 \quad \text{Eq 2-14}$$

Taking the Yeoh constitutive model, the shear modulus decreases with increasing strain at small strains, while it increases with increasing strain at higher strains. Compared with the neo-Hookean and Mooney-Rivlin constitutive models, this constitutive model is applicable over a wide range of strains.

Gent<sup>21</sup> proposed another strain energy function form based on  $I_1$ , which has the following expression:

$$W = -\frac{E}{6} J_m \ln(1 - (J_1 / J_m)) \quad \text{Eq 2-15}$$

where  $J_1 = I_1 - 3$  and  $J_m$  is a maximum value of  $J_1$ . This form empirically includes the effect of the maximum strain that a network molecular chain can undergo, which makes it suitable for use over a large range of strains. If the natural logarithm term in the Gent constitutive model is expanded<sup>17</sup>, the Gent constitutive model is transformed into a form of the Rivlin expression:

$$W = \frac{E}{6} \left[ (I_1 - 3) + \frac{1}{2J_m} (I_1 - 3)^2 + \frac{1}{3J_m^2} (I_1 - 3)^3 + \dots + \frac{1}{(n+1)J_m^n} (I_1 - 3)^{n+1} \right] \quad \text{Eq 2-16}$$

Equation 2-16 also shows that this form has a similar drawback as the inverse Langevin function: excessive terms.

Instead of being a function of the stretch invariants, some strain energy function forms were developed in terms of principal stretches<sup>24, 25</sup>. Ogden<sup>24</sup> proposed a specific form of strain energy function:

$$W = \sum_n \frac{\mu_n}{\alpha_n} (\lambda_1^{\alpha_n} + \lambda_2^{\alpha_n} + \lambda_3^{\alpha_n} - 3) \quad \text{Eq 2-17}$$

where  $\mu_n$  and  $\alpha_n$  are material constants.

The Ogden constitutive model also captures the nonlinear behaviour at high strains and can be applied to a wide strain range.

Most of the constitutive models reviewed are available to be used in commercially available finite element analysis codes, for example, ABAQUS<sup>†</sup>. Utilizing the finite element codes as a platform, these models can be applied to solve problems involving complex geometry and loading conditions.

Among all constitutive models reviewed, the eight-chain constitutive model is the most predictive. The Mooney-Rivlin constitutive model is quite popular in industrial use. The Mooney-Rivlin constitutive model has a much simpler form and provides satisfactory predictions for elastomeric materials at low or medium strain level.

### 2.2.3 Other Considerations for Constitutive Models

#### 2.2.3.1 Compressibility

All the strain energy functions mentioned previously are based on the assumption that elastomeric materials are incompressible. In reality, these materials are nearly incompressible. In cases where the material is highly confined, the compressibility must be modeled correctly to obtain accurate results. Constitutive models have been proposed to include the effects of compressibility in order to provide more accurate deformation representations. One approach that has been proposed is to divide the strain energy function into two separate parts, a deviatoric part and a hydrostatic part. The resulting strain energy function is:

$$W = W_D(\bar{I}_1, \bar{I}_2) + W_H(J) \quad \text{Eq 2-18}$$

where  $\bar{I}_1$  and  $\bar{I}_2$  are invariants of the deviatoric principal stretches,  $J$  is the volume ratio,  $\bar{I}_1 = J^{-2/3} I_1$ ,  $\bar{I}_2 = J^{-4/3} I_2$ . One possible expression for  $W_H$  is given by<sup>28</sup>

$$W_H = \sum_{i=1}^N \frac{1}{D_i} (J - 1) \quad \text{Eq 2-19}$$

where  $D_i$  are material constant.

---

<sup>†</sup> ABAQUS is a registered trademark of Hibbitt, Karlsson & Sorensen, Inc.

### 2.2.3.2 Mullins Effect and Time-dependence

Though the mechanical behavior of elastomeric materials is known to be rate-dependent and to exhibit Mullins effect upon cyclic loading, few attempts have been made to quantify these aspects of response.

Recently Marckmann *et al.*<sup>29</sup> proposed a model incorporating the Mullins effect by modifying the eight-chain constitutive material model. The Mullins effect has to be considered in specific cases such as the prediction of fatigue life in elastomeric parts, for example, automotive engine mounts. Their work assumes that the Mullins effect is a consequence of the inter-chain link breakage inside the material. The accuracy of the resulting constitutive equation was demonstrated with cyclic uniaxial experiments as shown in Figure 2-12. Other researchers have also developed purely phenomenological constitutive models without physical interpretations for the Mullins effect<sup>30, 31</sup>.

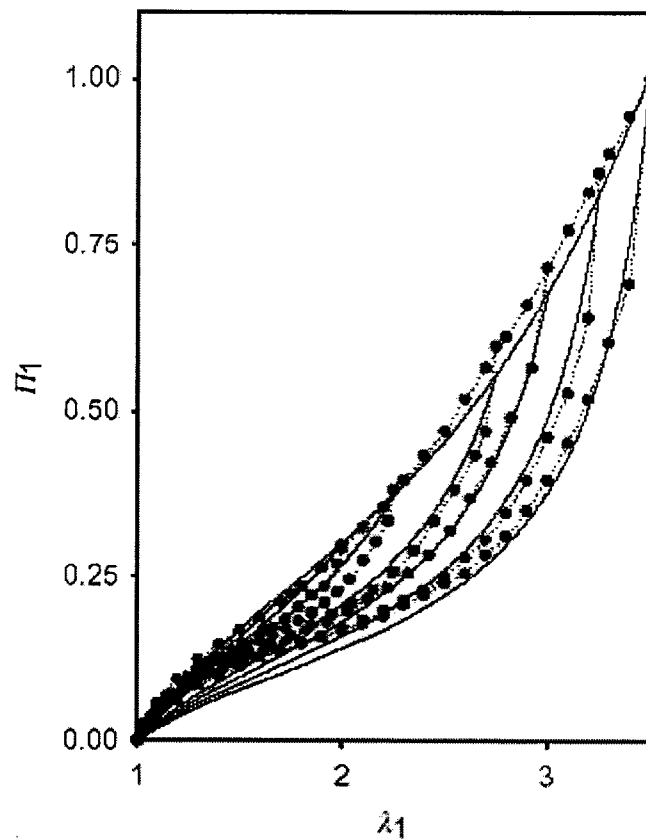


Figure 2-12 Comparison between nominal stress – stretch ( $\Pi_I - \lambda_I$ ) predictions and experimental data for a natural rubber under cyclic uniaxial tension

Bergstrom and Boyce<sup>16, 32, 33</sup> developed a time-dependent model to capture hysteresis upon cyclic loading. Their model decomposed the mechanical behaviour into two parts: an equilibrium network corresponding to the equilibrium state and a second network capturing the non-linear rate-dependent deviation from the equilibrium state. The time-dependence of the second network is assumed to be governed by the repetitive motion of molecules having the ability to significantly change conformation and thereby relaxing the overall stress state. Figure 2-13 shows their model predictions for filled rubber in uniaxial compression.

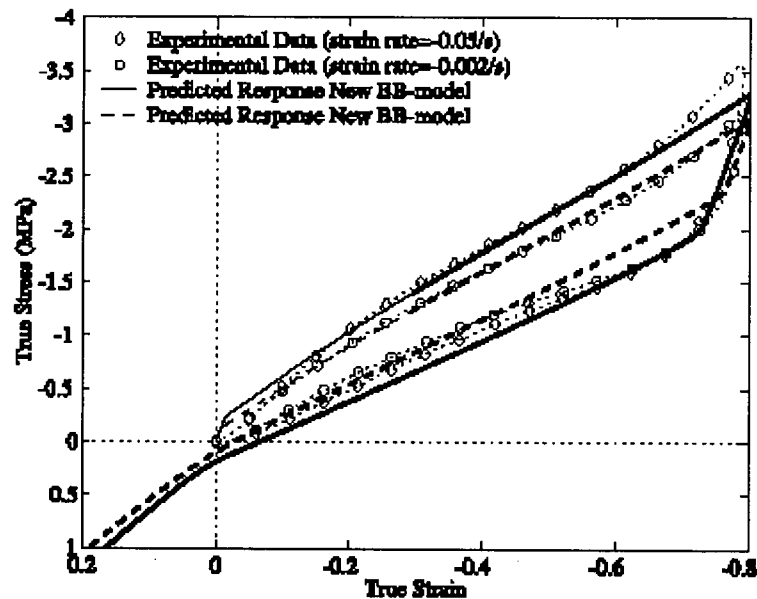


Figure 2-13 Comparison between predictions and experimental data for a Chloroprene rubber with 15 vol% carbon black under cyclic uniaxial compression at different strain rates<sup>16</sup>

### 2.2.3.3 Model Stability

In order to evaluate the phenomenological models, it should be ensured that the material constants in these models result in physically realistic and stable responses in all deformation states. A stable material must satisfy Drucker's stability postulates<sup>34</sup>: "1) the work done by the external agency during the application of the added set of forces on the changes in displacements it produces is positive, and 2) the net work performed by the external agency over the cycle of application and removal of the added set of forces and the changes in displacements it produces is nonnegative." The Drucker stability criterion requires that the Hessian matrix of the strain energy function be positive definite. The

components of the Hessian matrix can be written as:

$$H_{ijkl} = \frac{\partial^2 W}{\partial \varepsilon_{ij} \partial \varepsilon_{kl}} \quad \text{Eq 2-20}$$

For the general Rivlin strain energy form, one judicious choice would be to choose all positive coefficients for the stable constants<sup>17, 35</sup>. The constants in the statistical mechanics models are unconditionally stable.

### 2.3 SUMMARY

Mechanical deformation of elastomers under arbitrary loading conditions is complicated by the fact that loading variables such as deformation mode, maximum strain experienced, number of loading cycles at a strain level, relaxation, strain rate and temperature will affect the overall elastomer behaviour.

Most constitutive models for elastomeric materials are equilibrium models and are based on a strain energy function. These models can be classified into two categories: statistical constitutive models and phenomenological constitutive models. Statistical constitutive models reduce the number of relevant material parameters because of their physical foundations, but their mathematical derivations are very complicated. Phenomenological constitutive models provide another option. These constitutive models are developed based on experimental observations and phenomenological considerations. They are both mathematically simple and quite efficient.

Though loading variables affect the behaviours of elastomeric materials, only a few constitutive models incorporate loading variable as parameters. Most of these models are developed by modifying a particular form of basic constitutive model, usually the eight-chain constitutive model<sup>16, 29, 32, 33</sup>, so they have complicated forms. It is always difficult to utilize these constitutive models to commercial finite element codes. Therefore, their capability to solve problems with complex geometry and non-standard strain state is restricted.

### **3 SCOPE AND OBJECTIVES**

#### ***3.1 SCOPE OF THE RESEARCH PROJECT***

The goal of this research project is to develop mathematical constitutive models to predict the stabilized mechanical behaviour of elastomeric materials in non-uniform and/or multiaxial (i.e. none of the three standard types) deformation at low or medium strains (<100%). When these models are incorporated in a mechanical model as an input, they improve its accuracy and adaptability in non-uniform and/or multiaxial deformations. These constitutive models will aid in understanding the stable response of seal materials used in fuel cells.

To achieve this goal, the commercial finite element software package, ABAQUS, is used as a platform for predicting mechanical behaviour of an elastomeric material. The nonlinear solution capabilities and well documented user-defined subroutines in ABAQUS make it well suited to solve non-linear mechanical problems. ABAQUS also provides a specific module and user-subroutine interface for modeling properties of elastomeric materials.

The prediction of the mechanical deformation of a component under operational loading conditions requires first determining the constitutive material behaviour for use as a model input. The constitutive stress-strain behaviour of elastomers is nonlinear and sensitive to loading variables. Usually the constitutive material behaviour is defined through the use of a strain energy function. ABAQUS provides several standard strain energy functions to describe the hyperelastic properties of elastomers. However, none of these standard strain energy functions provide a means to alter the constitutive stress-strain behaviour according to the maximum strain or the deformation mode present during an analysis. This limitation poses an issue for the use of these constitutive models in applications exhibiting non-uniform and/or multiaxial deformations. By utilizing the user-defined-subroutine interface in ABAQUS, a constitutive model was developed using a novel way to take into account the maximum strain and the deformation mode. The Mooney-Rivlin strain energy function was chosen for use in this investigation as it has a

very simple form, gives acceptable results at moderate strains and is currently in use at Ballard. It should be noted that this methodology could be used to modify any of the standard strain energy functions.

Characterization tests were performed at UBC and correlated to material characterization data supplied by Ballard to provide experimental data for determining the material constants in the Mooney-Rivlin strain energy function. For verification of the model predictions, two material tests were designed and employed to demonstrate non-uniform and multiaxial deformation. Mechanical models were constructed for the two components using the proposed constitutive model as an input and were compared with the experimental data.

### **3.2 OBJECTIVES OF THE RESEARCH PROJECT**

The overall research objective of this research project is to develop, and verify constitutive models capable of predicting stable mechanical response of elastomers under non-uniform and multiaxial strain at moderate strains.

To satisfy this overall objective, the following sub-objectives were identified:

- To determine, experimentally, the stress – strain behaviour in simple deformation modes, including uniaxial tension, equibiaxial tension, and planar tension.
- To fit the standard Mooney-Rivlin strain energy function to the experimental stress – strain pairs by regression analysis.
- To develop constitutive models by modifying the standard Mooney-Rivlin strain energy function with novel techniques to describe non-uniform and/or multiaxial strain state.
- To develop mechanical models for two sample elastomer components, using the proposed constitutive models, as an input in an ABAQUS finite element analysis.
- To measure the experimental load and deformation characteristics of the elastomer components being designed for comparison with mechanical model predictions.

## **4 ELASTOMER CHARACTERIZATION**

A set of characterization data was provided by Ballard Power Systems Inc. for a candidate seal material, silicone elastomer. The data included experimental results for a complete set of elastomer characterization tests (uniaxial tension, equibiaxial tension and planar tension). The batch of material used for these tests is designated Lot A.

In addition to providing the characterization test data, Ballard also provided sheets of silicone elastomer to make samples for on-site experimental measurements conducted at UBC. However, the elastomer sheets provided by Ballard were taken from a different batch of material, designated Lot B. Uniaxial tension tests were conducted with this material to examine whether the silicone from Lot B had similar properties to the silicone from Lot A. Unfortunately, it was not possible to perform equibiaxial tension or planar tension tests at UBC.

All these tests were conducted with a low strain rate and the material response was considered to be the equilibrium response. In the following sections, the measured material responses for the material characterization tests provided by Ballard are summarized. The procedure to characterize a standard Mooney-Rivlin constitutive model is summarized for the Ballard data. Then, the on-site characterization tests for the new silicone (Lot B) are presented followed by constitutive model fitting from experimental data.

### ***4.1 INDUSTRIAL EXPERIMENTAL MEASUREMENT***

Data of three characterization tests for silicone from Lot A was provided by Ballard including uniaxial tension, equibiaxial tension and planar tension. These tests were performed with low strain rates at room temperature.

#### ***4.1.1 Uniaxial Tension***

The Ballard uniaxial tension tests were performed on an Instron material testing machine. Crosshead load was recorded as reaction force and a video extensometer was used to

measure sample deformation. The measured crosshead load and displacement were converted to nominal stress and nominal strain for output. An example of setup of a uniaxial tension test is shown in Figure 4-1.

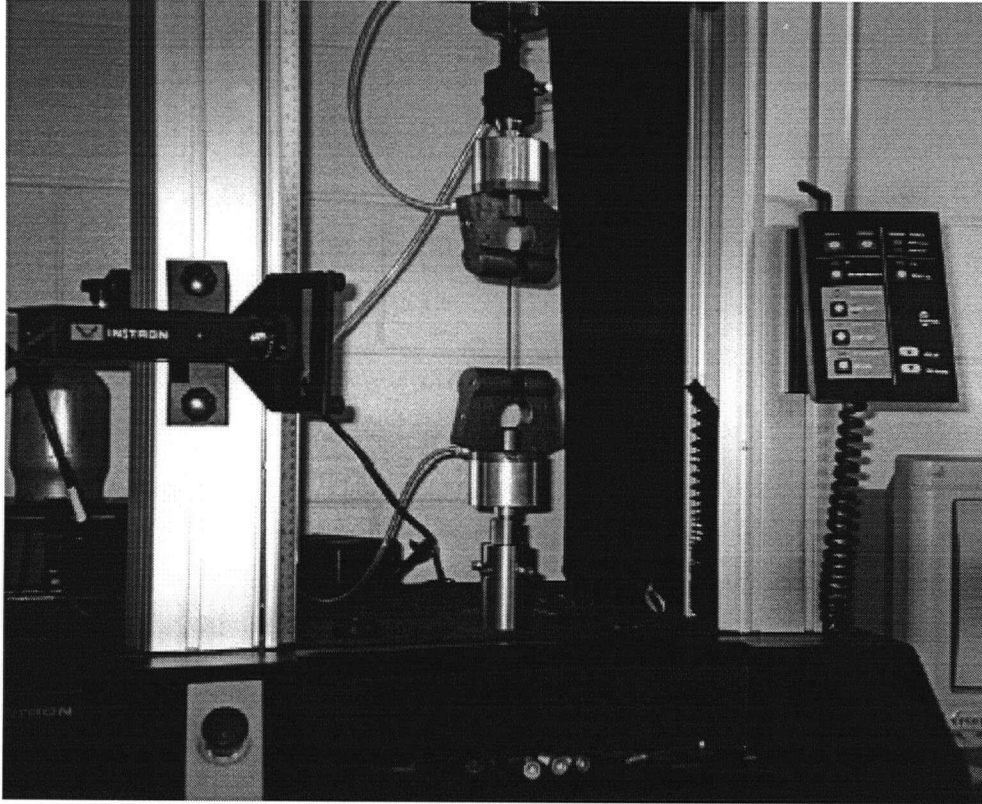


Figure 4-1 Example of a uniaxial tension experiment setup<sup>8</sup>

In the Ballard uniaxial tension tests, samples were deformed with a series of displacements corresponding to strains of 20%, 40%, 60%, 80%, 100% and 200%. At each strain level, samples were loaded to the particular strain followed by complete unloading to zero stress five times. The sample was then taken to a new higher strain level. A total of three samples were tested, each of which experienced incrementally increasing strain from 20% up to 200%.

The cyclic behaviour of a sample loaded to 20% and 40% strains for five repetitions is shown in Figure 4-2. As discussed in Chapter 2, the material response changes significantly during the first several loading cycles that the material experiences, which is known as the Mullins effect<sup>36</sup>. The fifth loading curve at each strain level was taken as the stable response for the strain level. The stable stress-strain curves for each strain level

tested are presented in Figure 4-3. The test set up and permanent (and/or viscoelastic) deformation resulted in stress and strain offsets in the unloaded state. The raw data was shifted by subtracting the stress and strain offsets to give actual stress – strain behaviour in Figure 4-3.

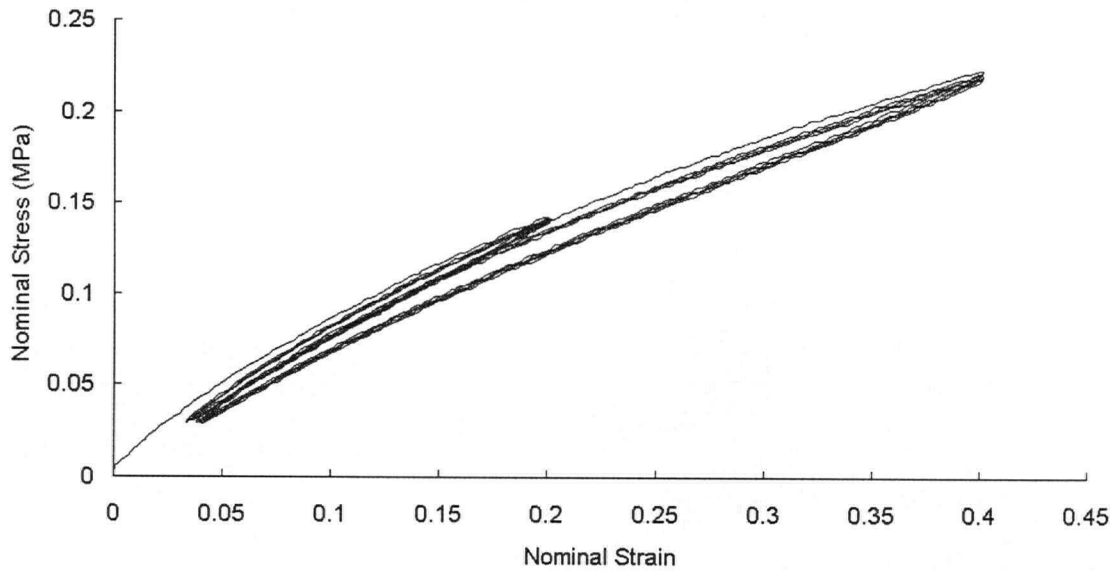


Figure 4-2 Cyclic behaviour of a sample in uniaxial tension tests provided by Ballard

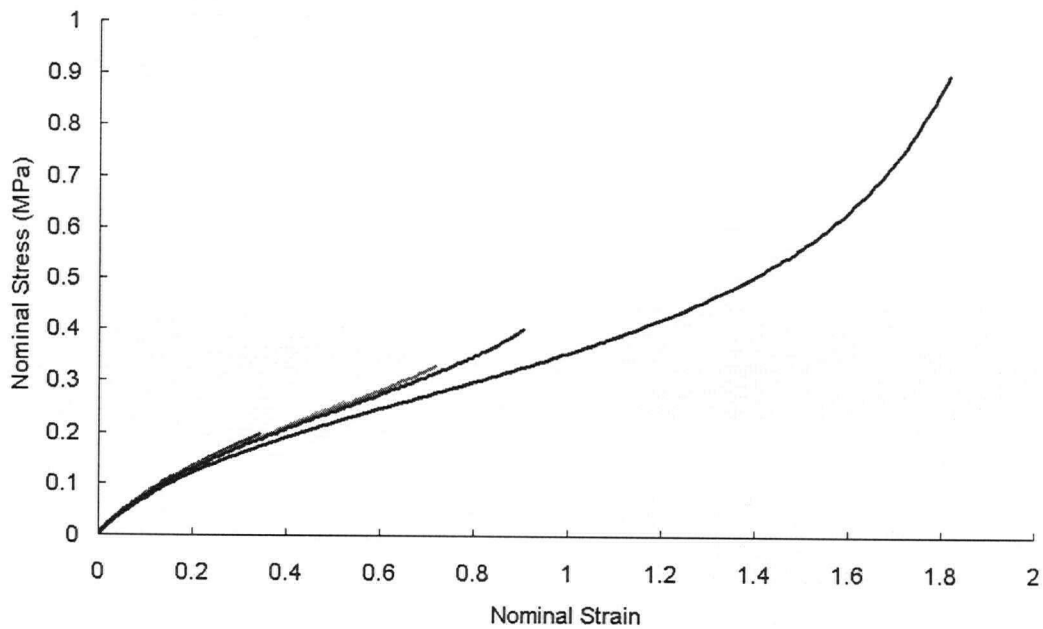


Figure 4-3 Stable stress-strain curves for different strain levels in the Ballard uniaxial tension tests

Figure 4-3 shows that the material response changes with the maximum strain experienced by the sample. Loading to higher strain levels induces more softening in the material response. The stress strain curve is highly nonlinear at high strains, demonstrating the characteristic S-shape.

#### 4.1.2 Equibiaxial Tension

The testing procedure for the equibiaxial tension tests was similar to that for uniaxial tension. Nominal stress and nominal strain were calculated from force and displacement measurements and recorded as output. Strain levels of 10%, 20%, 40%, 60%, 80% and 100% were used for these tests. Three samples were tested, each of which experienced the entire series of strain levels. However, for each strain level, the loading and unloading cycles were repeated ten times instead of five times. The tenth loading curve at each strain level was taken as the stable response for the strain level. An example of an equibiaxial tension setup is shown in Figure 4-4. Similar to the procedure used with the uniaxial tension data, the stress and strain were corrected by subtracting the remaining stress and strain offset from the raw data. The shifted stable loading curves for each strain level are given in Figure 4-5.

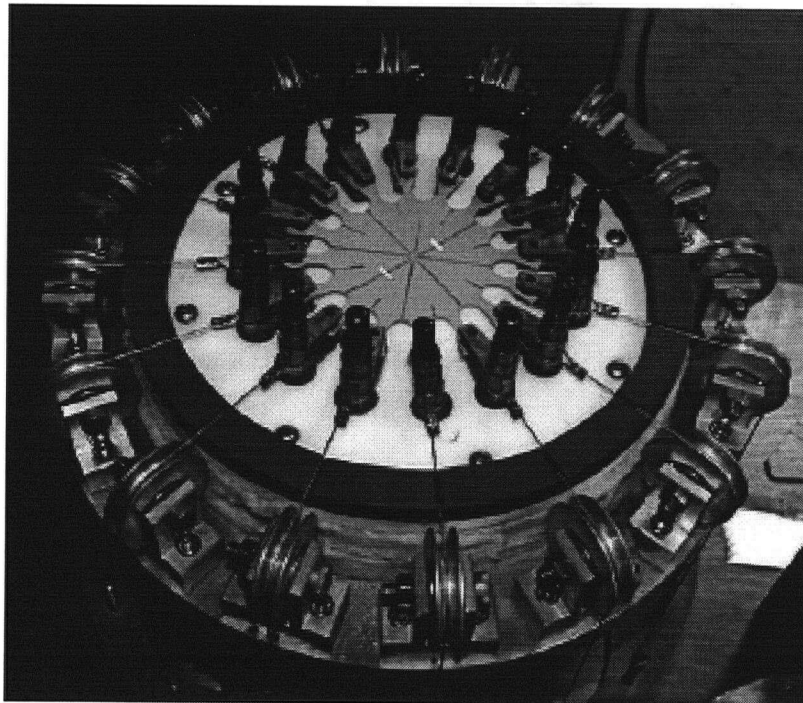
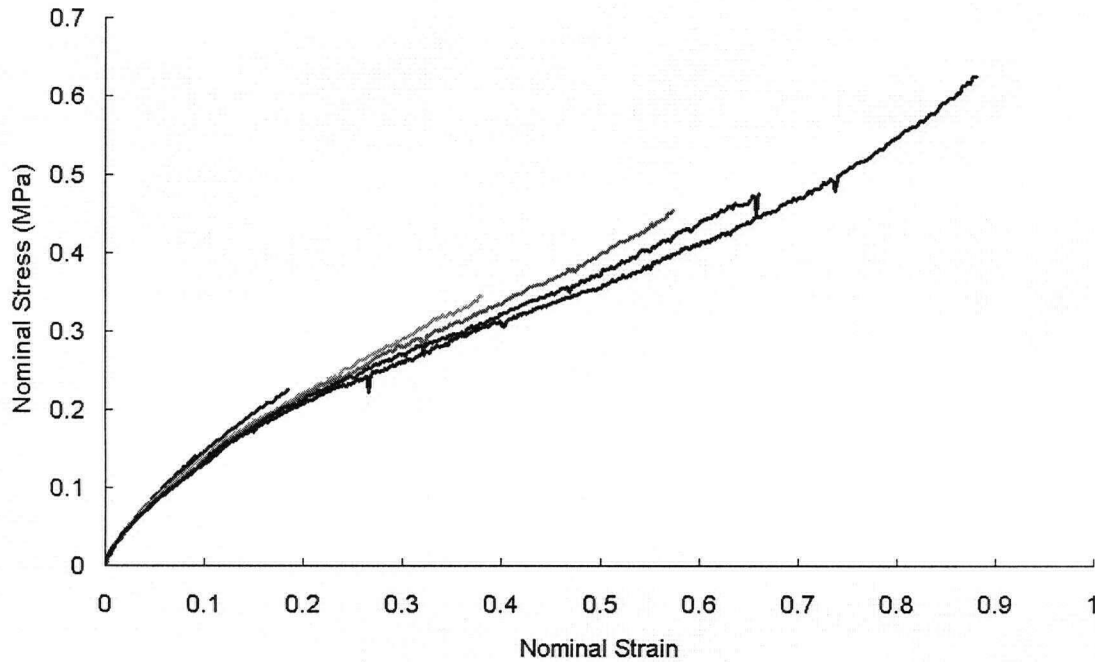


Figure 4-4 Example of an equibiaxial tension experiment setup<sup>8</sup>



**Figure 4-5 Stable loading curves for different strain levels in the Ballard equibiaxial tension tests**

As shown in Figure 4-5, straining the sample to a higher strain level induced softening. Once a sample was conditioned to a higher strain level, its behaviour changed and never went back to the previous stage. The S-shape of stress-strain curve was not very distinct here, considering the maximum strain was only 100%.

### **4.1.3 Planar Tension**

An example of a planar tension test setup is shown in Figure 4-6. The testing procedure for the planar tension tests was also similar to that for uniaxial tension. Nominal stress and nominal strain were calculated from force and displacement measurements and recorded as output. The samples were tested at a series of strain levels, including 20%, 40%, 60%, 80%, 100% and 200%. Four samples were tested, each of which experienced the entire strain series. For each strain level, the loading and unloading cycles were repeated five times. The fifth loading curves were taken as the stable behaviour. By subtracting the remaining stress and strain offset, stable stress-strain correlations for each strain level were extracted and are given in Figure 4-7.



Figure 4-6 Example of a planar tension experiment setup<sup>8</sup>

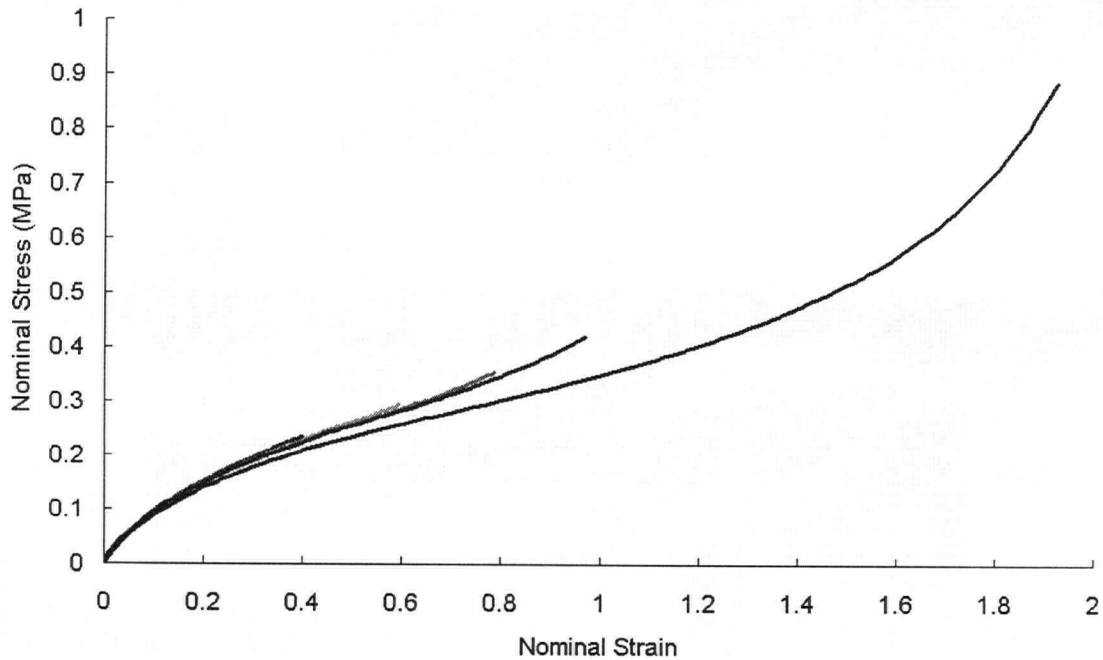


Figure 4-7 Stable loading curves for different strain levels in Ballard planar tension tests

Figure 4-7 demonstrates similar material response trends to those shown in Figures 4-3 and 4-5: straining the sample to a higher strain level induced irreversible changes in material behaviour. The stress-strain correlation was nonlinear.

#### 4.1.4 Material Constant Evaluation for Industrial Characterization Tests

Assuming the expected in-service straining of an elastomer seal is in the low to medium strain range (<100%), a material constitutive model using the Mooney-Rivlin strain energy formulation should provide an adequate representation of the material response. Constants in the Mooney-Rivlin constitutive model can be evaluated using the measured nominal stress-strain data. As discussed in Chapter 2, material response changes with the maximum strain experienced and the deformation mode. In order to investigate the impact of these effects, material constants were evaluated separately for each strain level and deformation mode. The material constant evaluation procedure incorporated the experimental results from each of the samples tested at each loading condition. The material constants were determined using a least-square fitting procedure. In order to ensure model stability<sup>17, 35</sup>, the material constants were constrained to be positive values. The commercial data analysis package Origin 6.0 (Microcal Software Inc.) was used to complete the data fitting.

##### 4.1.4.1 Material Constant Evaluation for Uniaxial Tension

Recalling Equations 2-4 and 2-5 in Chapter 2, based on the Mooney-Rivlin constitutive model, the stress – strain relationship for uniaxial tension can be expressed as:

$$f_U = 2(1 - \lambda_U^{-3})(\lambda_U C_{10} + C_{01}) \quad \text{Eq 4-1}$$

where  $\lambda_U$  is the stretch in the loading direction. The nominal uniaxial strain is defined by  $\varepsilon_U = \lambda_U - 1$ ,  $f_U$  is the nominal uniaxial stress and  $C_{10}$  and  $C_{01}$  are the material constants that must be determined.

The measured nominal stress – strain pairs were used with Equation 4-1 to derive material constants,  $C_{10}$  and  $C_{01}$ , for the Mooney-Rivlin constitutive model in the uniaxial tension loading mode. Table 4-1 gives the resulting constants for the different strain levels.

**Table 4-1 Mooney-Rivlin material constants for the Ballard uniaxial tension tests at different strain levels**

Strain Level	$C_{10}$ (MPa)	$C_{01}$ (MPa)	$R^2$
0.2	3.50E-16	0.1533	0.9951
0.4	0.0386	0.1062	0.9936
0.6	0.0691	0.0653	0.9950
0.8	0.0914	0.0332	0.9914
1	0.1090	0.0049	0.9888
2	0.1192	4.92E-17	0.8873

As expected, Table 4-1 shows that the material constants change with strain level. As discussed earlier, material behavior changes with the maximum strain experienced.  $C_{10}$  increases with increasing strain level, while  $C_{01}$  decreases with increasing strain level. In order to evaluate the comparative importance of the material constants, the strain energy component  $W_{ij}$  for each term has been calculated as

$$W_{ij} = C_{ij} (I_1 - 3)^i (I_2 - 3)^j \quad \text{Eq 4-2}$$

The ratios of strain energy components  $W_{ij}$  to the total strain energy  $W$  in uniaxial tension test are compared in Table 4-2. As shown in Table 4-2, for the uniaxial tension tests, the strain energy component,  $W_{01}$ , plays an important role in the Mooney-Rivlin constitutive model at low strain levels (<60%). When strain is increased above this level,  $W_{10}$  became a predominant factor.

**Table 4-2 Comparison of the comparative importance of strain energy components (Ballard uniaxial tension)**

Strain Level	$W_{10} / W$	$W_{01} / W$
0.2	2.58E-15	1
0.4	0.3130	0.6870
0.6	0.5922	0.4078
0.8	0.8039	0.1961
1.0	0.9726	0.0274
2.0	1	1.93E-16

The material constants, determined by least-square fit, can be used to evaluate the stress-strain response using Equation 4-2. Figure 4-8 gives a comparison between measured and estimated stress-strain correlations. As shown in Figure 4-8, at low or medium strain levels (<100%), the Mooney-Rivlin constitutive model response gives an acceptable representation of the measured data. At higher levels, the constitutive model response shows a large deviation from the measured data. A constitutive model using a higher order polynomial strain energy form or another advanced form may give a better representation. Since this research programme is focused on a low or medium strain deformation application, the Mooney – Rivlin constitutive model will provide satisfactory accuracy and its simplicity is preferable for industrial use.

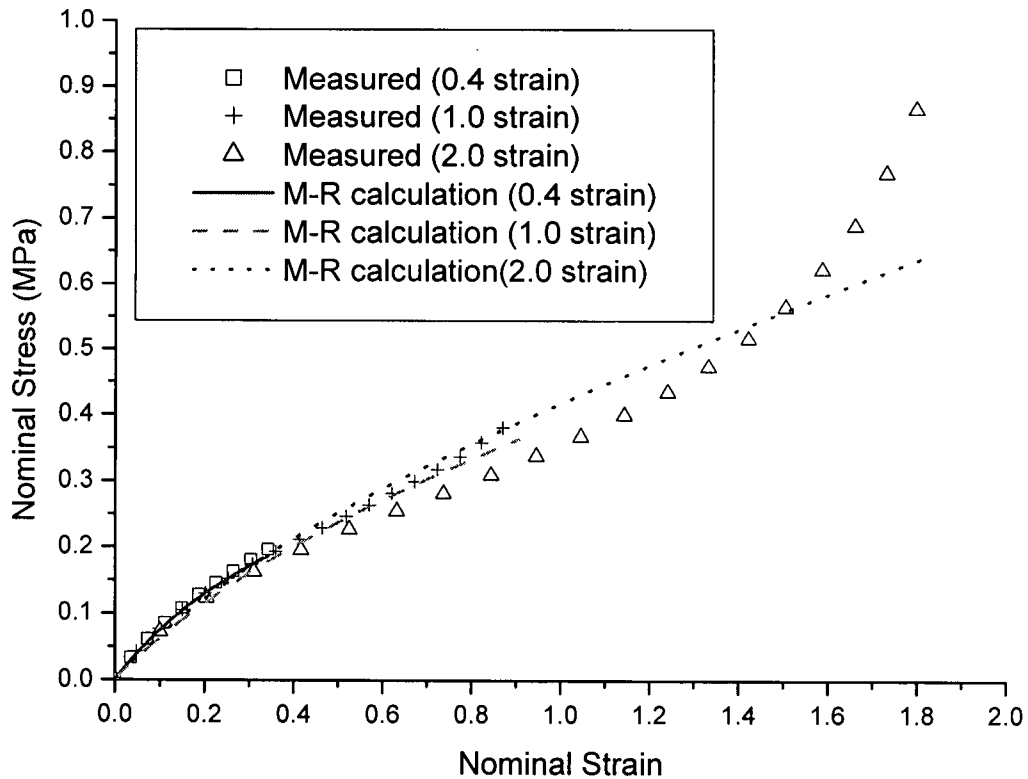


**Figure 4-8 Comparison of measured stress – strain correlations and calculations with the Mooney-Rivlin constitutive model for Ballard uniaxial tension tests at different strain levels**

#### 4.1.4.2 Material Constant Evaluation for Equibiaxial Tension

Recalling Equations 2-4 and 2-5 in Chapter 2, based on the Mooney-Rivlin constitutive model, the stress – strain relationship for equibiaxial tension can be expressed as:

$$f_B = 2(\lambda_B - \lambda_B^{-5})(C_{10} + \lambda_B^2 C_{01}) \quad \text{Eq 4-3}$$

where  $\lambda_B$  is the stretch in the two perpendicular loading directions, the nominal equibiaxial strain is defined as  $\varepsilon_B = \lambda_B - 1$ .  $f_B$  is nominal equibiaxial stress.

Following a similar procedure to that used with the uniaxial tensile data, the measured nominal stress – strain pairs for the equibiaxial tests were used with Equation 4-3 to determine the Mooney-Rivlin material constants,  $C_{10}$  and  $C_{01}$ . Table 4-3 gives the resulting constants for the different strain levels. Similar to the uniaxial tension constant data, Table 4-3 shows that material constants change with strain level in equibiaxial tension. Generally speaking,  $C_{10}$  decreases with increasing strain level, while  $C_{01}$  increases with increasing strain level. This trend is different from that discussed in the uniaxial tension tests.

**Table 4-3 Mooney-Rivlin material constants for the Ballard equibiaxial tension tests at different strain levels**

Strain level	$C_{10}$ (MPa)	$C_{01}$ (MPa)	$R^2$
0.1	0.1544	5.84E-16	0.9836
0.2	0.1467	6.55E-16	0.9839
0.4	0.1360	1.00E-18	0.9863
0.6	0.1165	0.0095	0.9850
0.8	0.0985	0.0165	0.9834
1.0	0.0970	0.0176	0.9911

Following a similar procedure to that used with the uniaxial constant data, the ratios of strain energy components  $W_{ij}$  to the total strain energy  $W$  for different strain levels in equibiaxial tension test are compared to evaluate the comparative importance of material constants in Table 4-4.

**Table 4-4 Comparison of the comparative importance of strain energy components (Ballard equibiaxial tension)**

Strain Level	$W_{10} / W$	$W_{01} / W$
0.1	1	4.30E-15
0.2	1	5.70E-15
0.4	1	1.16E-17
0.6	0.8658	0.1342
0.8	0.7241	0.2759
1	0.6743	0.3257

Unlike in uniaxial tension, Table 4-4 shows for the equibiaxial tension test, the strain energy component  $W_{10}$  is always predominant for all strain levels. This comparison also shows that  $W_{10}$  begins to have an impact at higher strains and based on this trend, may be significant at high strain levels.

Once material constants are determined by least-square fit, the stress-strain response can be calculated using Equation 4-3. Figure 4-9 shows a comparison between the measured and calculated stress-strain correlations. For equibiaxial tension, the Mooney-Rivlin constitutive model calculations give an acceptable representation of the measured data at low and medium strain levels (<100%).

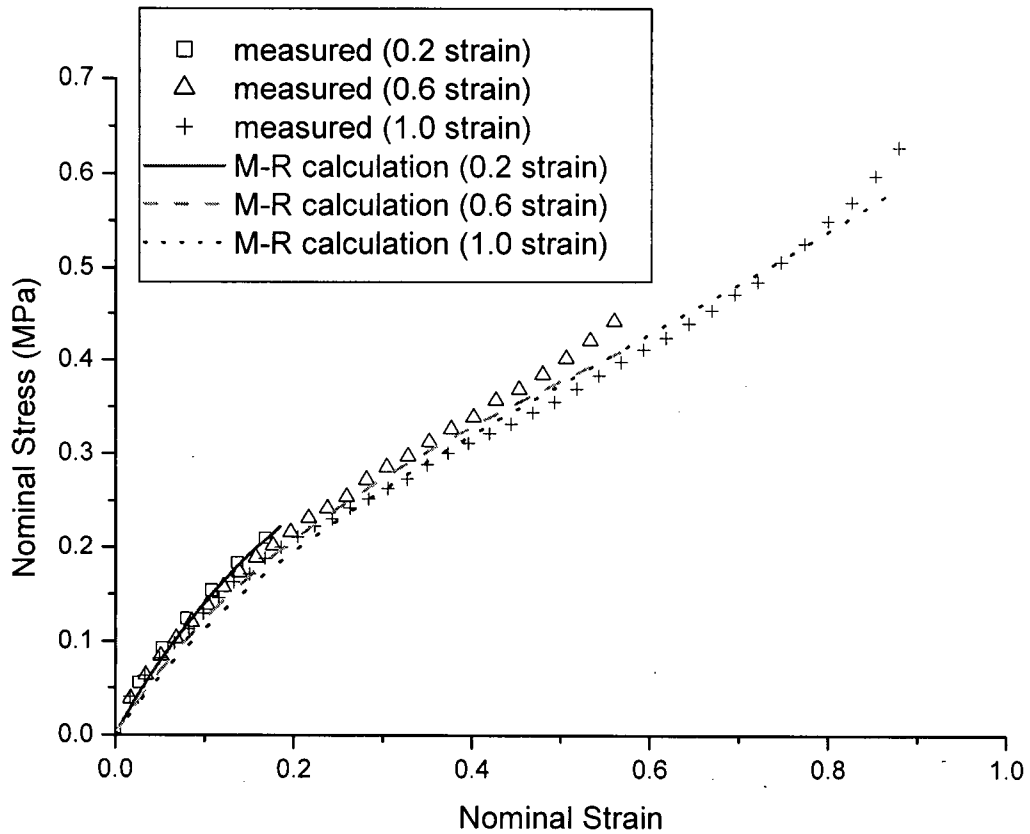


Figure 4-9 Comparison of measured stress – strain correlations and calculations with the Mooney-Rivlin constitutive model for Ballard equibiaxial tension tests at different strain levels

#### 4.1.4.3 Material Constant Evaluation for Planar Tension

Recalling Equations 2-4 and 2-5 in Chapter 2, based on the Mooney-Rivlin constitutive model, the stress – strain relationship for planar tension can be expressed as:

$$f_s = 2(\lambda_s - \lambda_s^{-3})(C_{10} + C_{01}) \quad \text{Eq 4-4}$$

where  $\lambda_s$  is the stretch in the loading direction, the nominal planar strain is defined by  $\varepsilon_s = \lambda_s - 1$  and  $f_B$  is the nominal planar stress.

Considering the format of Equation 4-4, employing a similar procedure to that used with

the uniaxial tensile data and the equibiaxial tensile data does not give independent  $C_{10}$  and  $C_{01}$  values. Instead, the sum of  $C_{10}$  and  $C_{01}$  may be calculated. Table 4-5 gives the resulting combined constants for the different strain levels. In planar tension, Table 4-5 indicates that the material constants show little change with strain level. The sum of  $C_{10}$  and  $C_{01}$  decreases slightly with increasing strain level.

**Table 4-5 Mooney-Rivlin material constants for the Ballard planar tension tests of at different strain levels**

Strain level	$C_{10} + C_{01}$ (MPa)	$R^2$
0.2	0.1318	0.9054
0.4	0.1165	0.9664
0.6	0.1120	0.9732
0.8	0.1086	0.9857
1.0	0.1074	0.9893
2.0	0.1118	0.9061

Once material constants are determined using the least-square fit, stress-strain correlations can be calculated taking Equation 4-4. A comparison between measured and calculated stress-strain correlations is given in Figure 4-10. For planar tension, the Mooney-Rivlin constitutive model evaluations gives an acceptable representation of the measured data at low or medium strain level (<100%). However, at higher strain levels, the material shows a highly nonlinear response which is not described by the Mooney-Rivlin constitutive model.

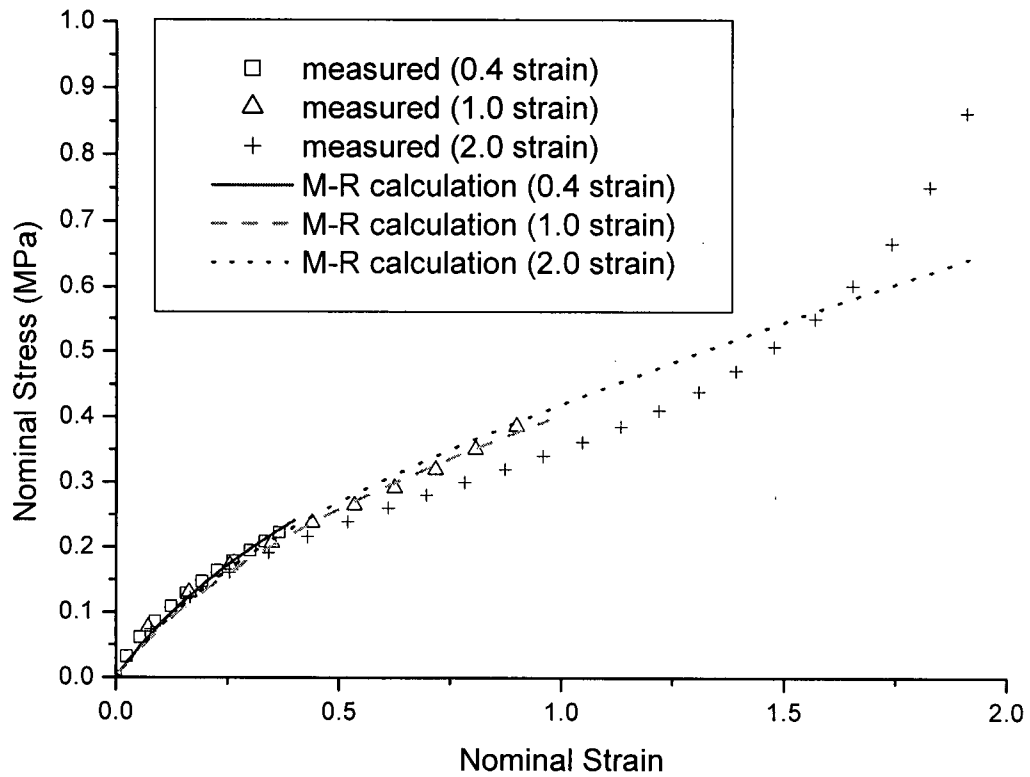


**Figure 4-10 Comparison of measured stress – strain correlations and calculations with the Mooney-Rivlin constitutive model for Ballard planar tension tests at different strain levels**

Material constants evaluated for different testing conditions are compared in Figure 4-11 for the silicone tested by Ballard. The material constants obtained for the three different loading modes show dependencies on testing conditions, including deformation modes and loading history.

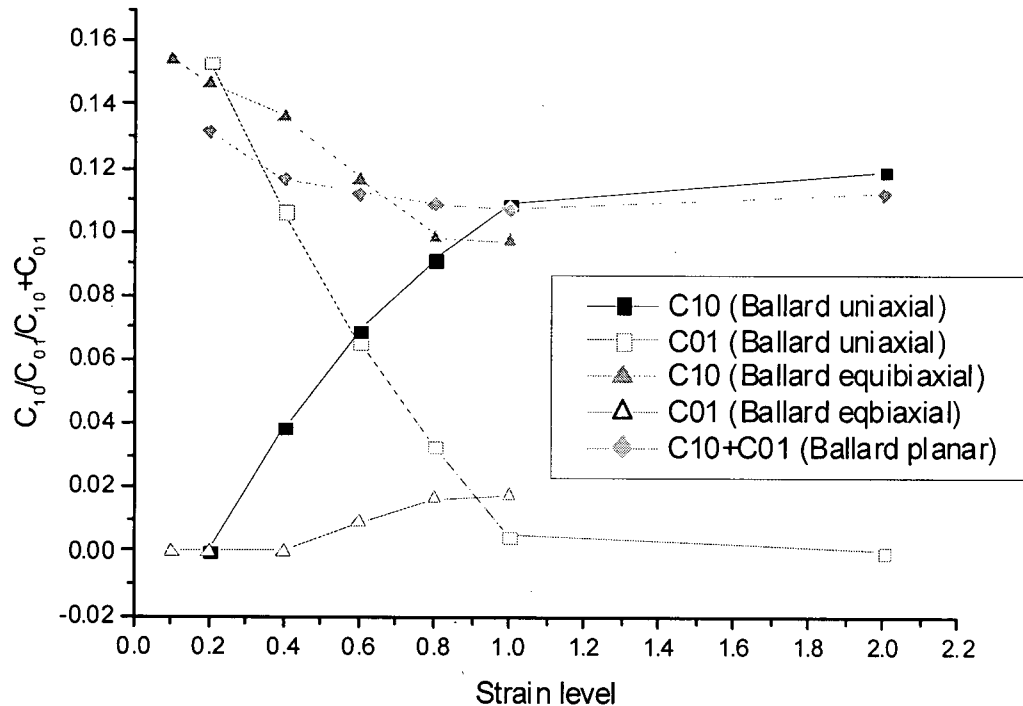


Figure 4-11 Material constants evaluated for different testing conditions for the silicone tested by Ballard

## 4.2 ON-SITE EXPERIMENTAL MEASUREMENTS

Uniaxial tension tests were conducted at UBC, using samples cut from silicone sheets (Lot B) provided by Ballard Power Systems Inc. The material provided by Ballard was from a different lot.

### 4.2.1 Uniaxial Tension

A rule die was used to cut standard dogbone test samples from the silicone sheets with the profile shown in Figure 4-12. The dogbone samples were tested on a Minimat 2000 materials testing machine (Rheometrics Scientific, Inc.). Figure 4-13 shows a photograph of a uniaxial tension test sample being tested on the Minimat. A 20N load cell was used considering the estimated force needed to strain the dogbone samples. The force resolution of the Minimat is 0.02 N (0.1% of the maximum load). The strain rate used was 0.004/s (crosshead speed of 1mm/s). Tests were conducted at room temperature.

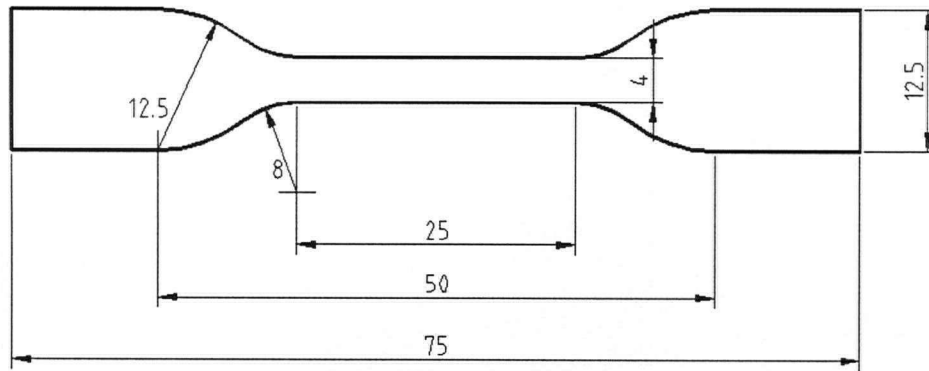


Figure 4-12 Profile of dogbone sample in UBC uniaxial tension tests (unit: mm, sample thickness=1.0mm)

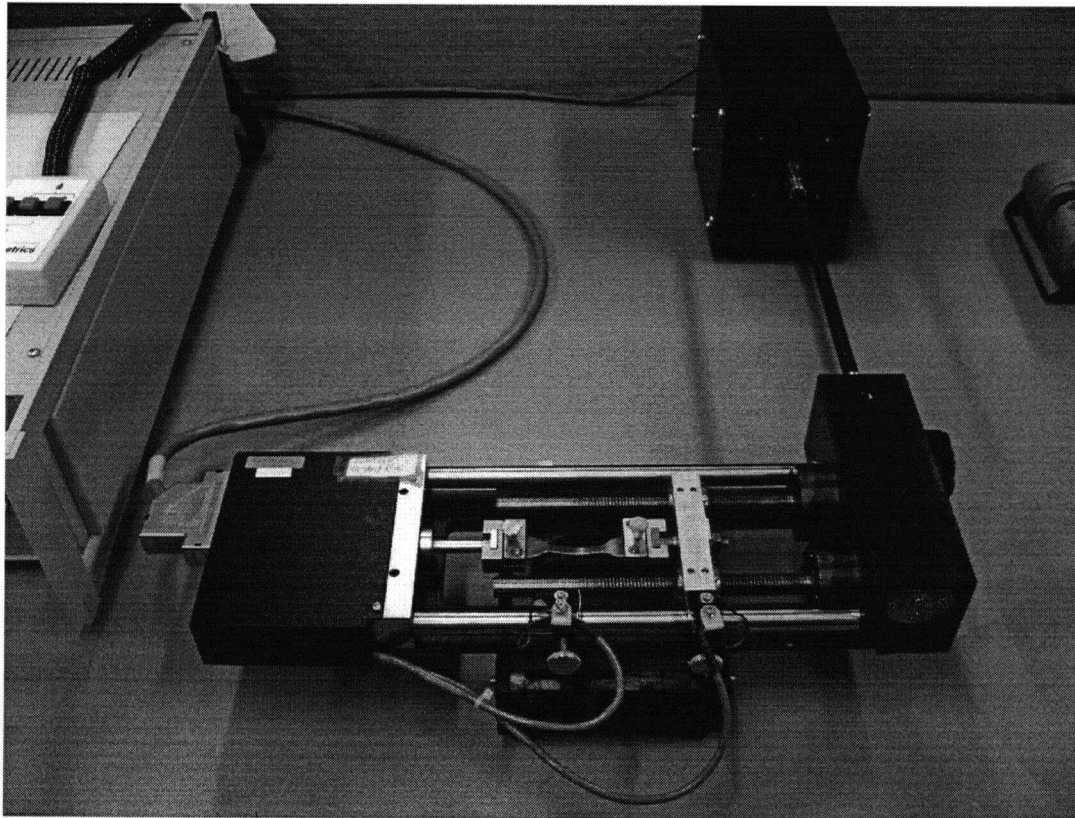


Figure 4-13 Photograph of a uniaxial tension experiment setup at UBC

Following the same procedure used in the Ballard tests, samples were loaded to a particular strain level followed by complete unloading to zero displacement five times. Samples were then loaded to a higher strain level. The strain levels tested were 20%, 40%, 60%, 80% and 100%. The highest strain level of 200% tested during the Ballard uniaxial tests could not be attained using the Minimat due to the frame dimension. In total, five samples were tested, each of which experienced the entire series of strain levels from 20% up to 100%.

For Ballard tests, a video extensometer was used to measure displacement. A similar video extensometer was not available for the experiments performed at UBC. Considering the geometry of the sample is small and the testing instrumentation is also compact, it was impractical to use a mechanical extensometer either. Instead, a Mitutoyo caliper was used to measure the displacement at each strain level by hand. The gauge-length was marked with reference lines using a special template with 11 evenly spaced parallel lines. The distance between each adjacent line was 2.5mm. The dogbone samples were marked using the template before testing as shown in Figure 4-14. When the sample was strained to a particular strain level for the fifth time, the strain was held and the displacement between the two exterior lines was measured using the caliper. It is assumed that the stretch in the gauge-length increased uniformly with time. Therefore, according to the displacement measured at each strain level and the time needed to reach the maximum strain, the correlation between the instantaneous gauge-length displacement and time was established. Crosshead load was recorded as a function of time by the Minimat. The correlation between instantaneous force and displacement was established via time. The nominal stress-strain correlation was then calculated from the force-displacement correlation.

An example of the stable loading curves for the series of strain levels is given in Figure 4-15. The plotted stable stress-strain curves were shifted to the origin followed a similar procedure to that used to shift the Ballard data. Figure 4-15 shows that the material response changes with the maximum strain experienced, which is similar to the trend in the Ballard uniaxial tension tests. However, the stress-strain correlations measured at

UBC exhibit more noise compared with the Ballard data, especially at low strain levels.

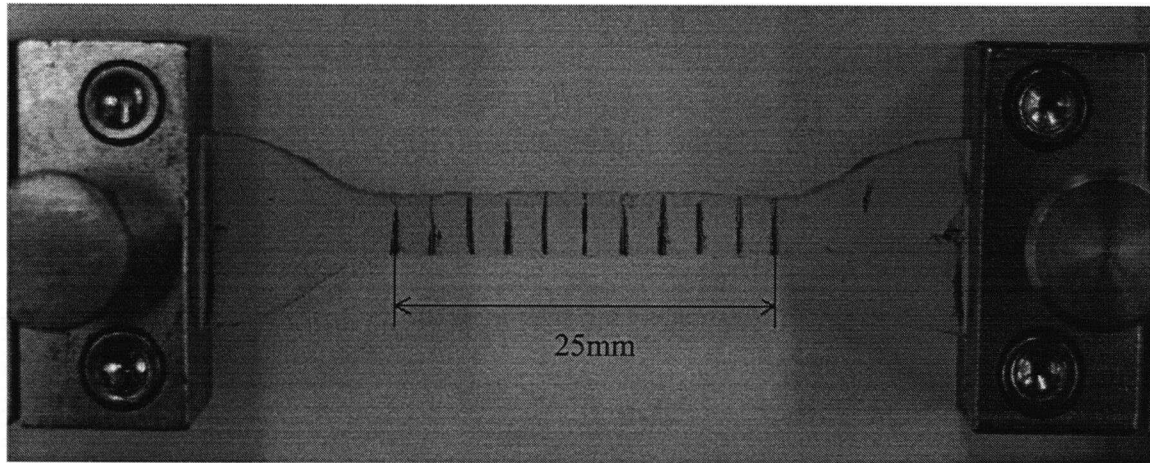


Figure 4-14 Marked dogbone sample for the UBC uniaxial tension tests

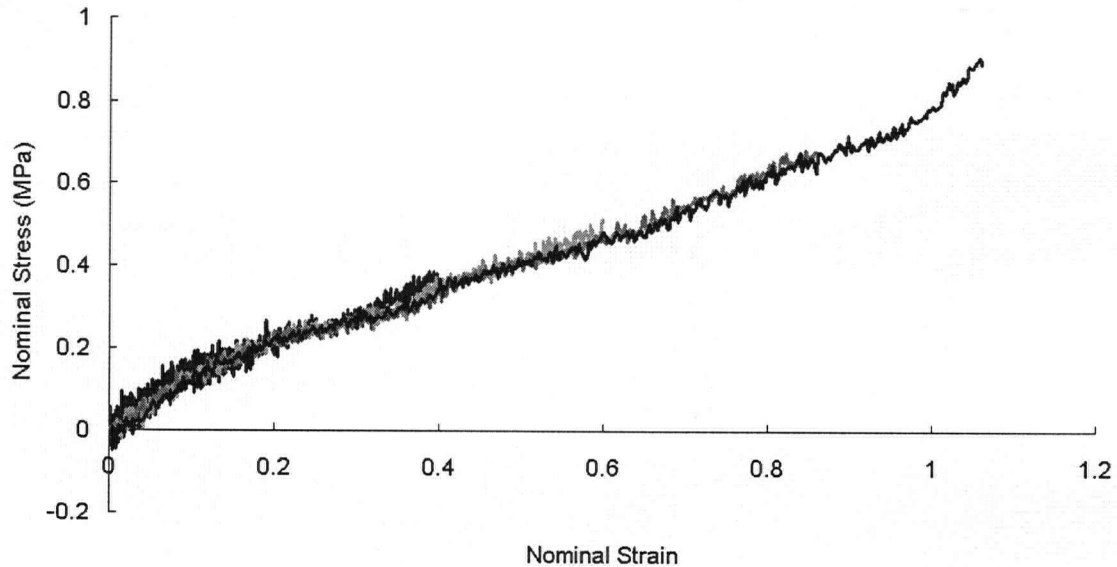


Figure 4-15 Stable stress-strain curves for different strain levels in the UBC uniaxial tension tests

## 4.2.2 Material Constant Evaluation for UBC Experimental Measurement

### 4.2.2.1 Material Constant Evaluation for Uniaxial Tension

The same procedure used to fit the material constants for the Ballard uniaxial data was used for the UBC data to derive the Mooney-Rivlin material constants,  $C_{10}$  and  $C_{01}$ . Table 4-6 gives the resulting constants at the different strain levels. Similar to the Ballard

uniaxial tension constant data, Table 4-6 shows that the material constants change with strain level in the UBC uniaxial tension tests. The  $R^2$  at the 0.2 strain level was notably smaller than the  $R^2$ s at the other strain levels. The smaller  $R^2$  resulted from the higher noise ratio at 0.2 strain. Table 4-5 shows that generally speaking,  $C_{10}$  increased with increasing strain level while  $C_{01}$  decreased with increasing strain level. The ratios of strain energy components  $W_j$  to the total strain energy  $W$  in the uniaxial tension test are compared in Table 4-7. For the UBC uniaxial tension tests, the strain energy component  $W_{01}$  plays an important role in the Mooney-Rivlin constitutive model at low strain levels (<60%). When strains increase above this level,  $W_{10}$  becomes predominant. This trend is similar to that found in the Ballard uniaxial tension tests.

**Table 4-6 Mooney-Rivlin material constants for UBC uniaxial tension tests at different strain levels**

Strain Level	$C_{10}$ (MPa)	$C_{01}$ (MPa)	$R^2$
0.2	1.45E-14	0.2661	0.8235
0.4	0.0883	0.1539	0.9592
0.6	0.1511	0.0740	0.9753
0.8	0.2037	2.41E-16	0.9777
1	0.2078	7.31E-16	0.9663

**Table 4-7 Comparison of the comparative importance of strain energy components (UBC uniaxial tension)**

Strain Level	$W_{10} / W$	$W_{01} / W$
0.2	6.18E-14	1
0.4	0.4182	0.5818
0.6	0.7368	0.2632
0.8	1	7.96E-16
1.0	1	2.20E-15

Once material constants were determined, the stress-strain correlation can be calculated

using Equation 4-1. Figure 4-16 shows a comparison between the measured and calculated stress-strain correlations. For the UBC uniaxial tension tests, the Mooney-Rivlin constitutive model evaluations also give an acceptable representation of the measured data at low and medium strain levels (<100%).

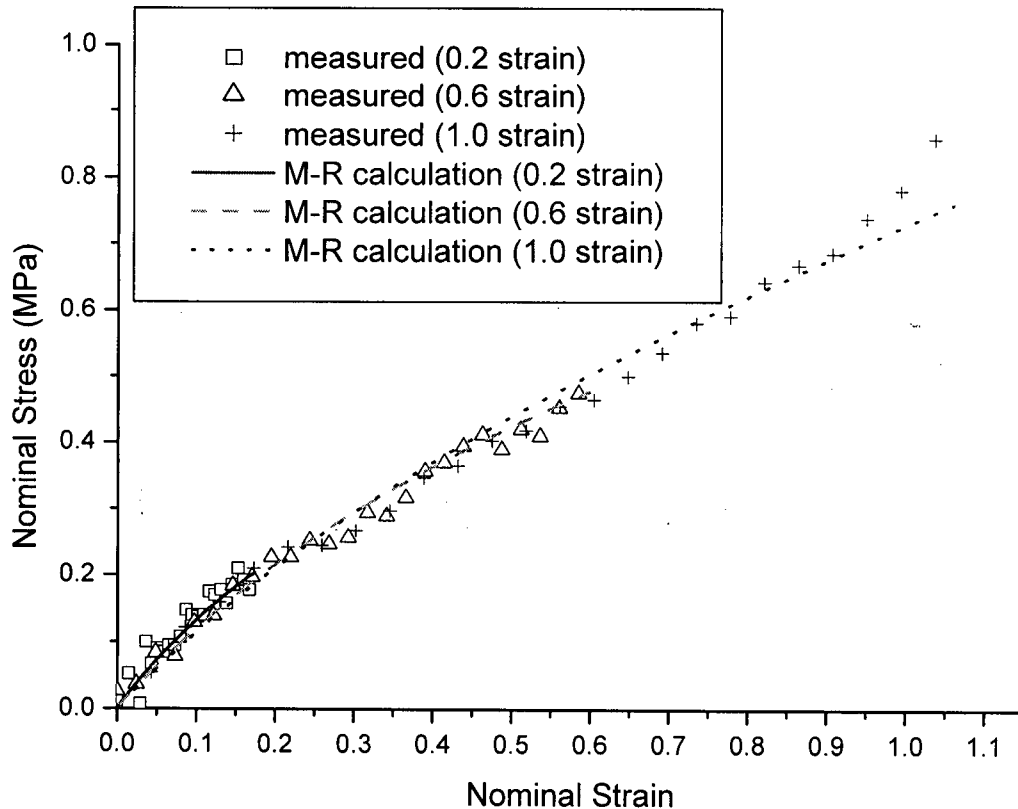


**Figure 4-16 Comparison of measured stress – strain correlations and calculations with the Mooney-Rivlin constitutive model for UBC uniaxial tension tests at different strain levels**

When Figures 4-8 and 4-16 are compared, at the same strain level, the measured stress of the UBC uniaxial tests was much higher than that of the Ballard tests. The difference between Ballard and UBC measurements is demonstrated in Figure 4-17 for 1.0 strain level. Although the materials came from different lots, this large variation in behaviours was unexpected. The difference may be partially due to the different testing conditions. Unfortunately, the detailed testing conditions for the Ballard tests were not available, thus

could not be repeated exactly at UBC. However, it is known that the Ballard tests were conducted with a low strain rate at room temperature. The UBC tests were also conducted with very low strain rate (0.004/s) at room temperature. There may be other sources of errors, including machine calibration and displacement measurement with/without a video extensometer. However, none of these reasons should be sufficient to account for the large difference between the Ballard and UBC uniaxial tension test data. The conclusion drawn was that the properties of the silicone change significantly from lot to lot.

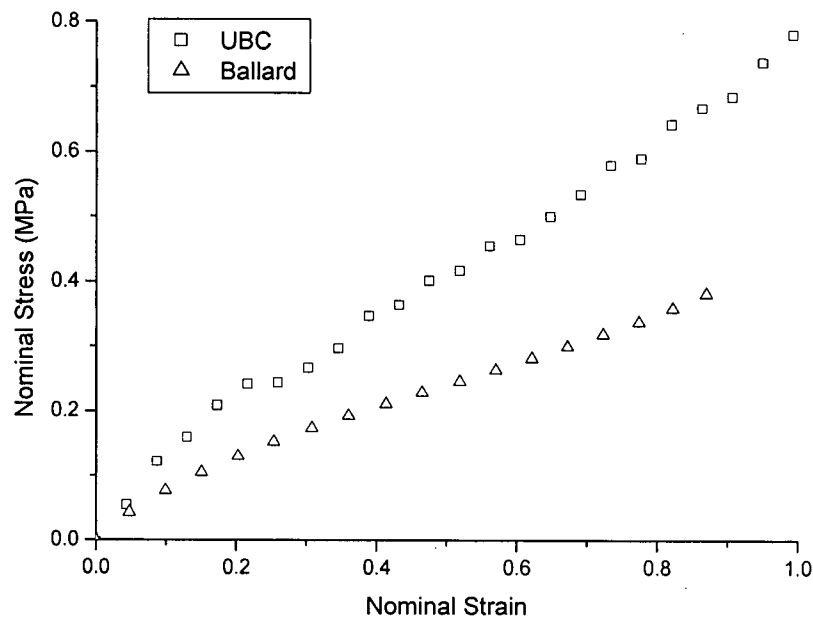


**Figure 4-17 Comparison of UBC and Ballard measurements for uniaxial tension at 1.0 maximum strain**

#### **4.2.2.2 Material Constant Estimation for Equibiaxial Tension and Planar Tension**

Based on the difference in the uniaxial test data between the materials tested at UBC and Ballard, it is expected that this difference will extend to the equibiaxial and planar tension behaviours. Unfortunately, the equibiaxial and planar tension tests could not be completed at UBC. Considering the Ballard and UBC uniaxial tension stress data at the same strain level showed similar trends but different magnitudes, an attempt was made to develop a conversion factor to scale the Ballard uniaxial data to match the UBC data at

the same strain level. The scale factor,  $a$ , was calculated as the following.

$$f_{U,UBC} = af_{U,Ballard} \quad \text{Eq 4-5}$$

The equation for the Mooney-Rivlin constitutive model applied to the Ballard uniaxial data is:

$$f_{U,Ballard} \approx 2(1 - \lambda_U^{-3})(\lambda_U C_{10,U,Ballard} + C_{01,U,Ballard}) \quad \text{Eq 4-6}$$

Substituting this equation into Equation 4-5 gives:

$$f_{U,UBC} = af_{U,Ballard} \approx a(2(1 - \lambda_U^{-3})(\lambda_U C_{10,U,Ballard} + C_{01,U,Ballard})) \quad \text{Eq 4-7}$$

where  $f_{U,Ballard}$  is the nominal stress provided by Ballard,  $f_{U,UBC}$  is the nominal stress measured at UBC, and  $C_{10,U,Ballard}$  and  $C_{01,U,Ballard}$  are material constants evaluated for the Ballard uniaxial tension data.

The nominal stress – strain data measured at UBC was used with Equation 4-7 to derive the scale factor  $a$  for each strain level. Table 4-8 shows the resulting values for  $a$ . Table 4-8 shows that the scale factor changes with strain level but not significantly. This technique demonstrates that it is feasible to scale the Ballard data using a simple global scale factor to reach the magnitude of the UBC data for all strain levels in the uniaxial tests. The average of the scale factors for the different strain levels was considered as the global scale factor. The measured UBC data and the scaled Ballard data using the global scale factor are compared in Figure 4-18. After scaling, the measured Ballard uniaxial data agrees with the UBC data.

**Table 4-8 Scale factor for Ballard – UBC uniaxial tension data conversion at different strain levels**

Strain level	0.2	0.4	0.6	0.8	1.0	Average
$a$	1.7352	1.7164	1.7664	1.8132	1.8586	1.7780
$R^2$	0.82349	0.95896	0.97434	0.97175	0.96459	n/a

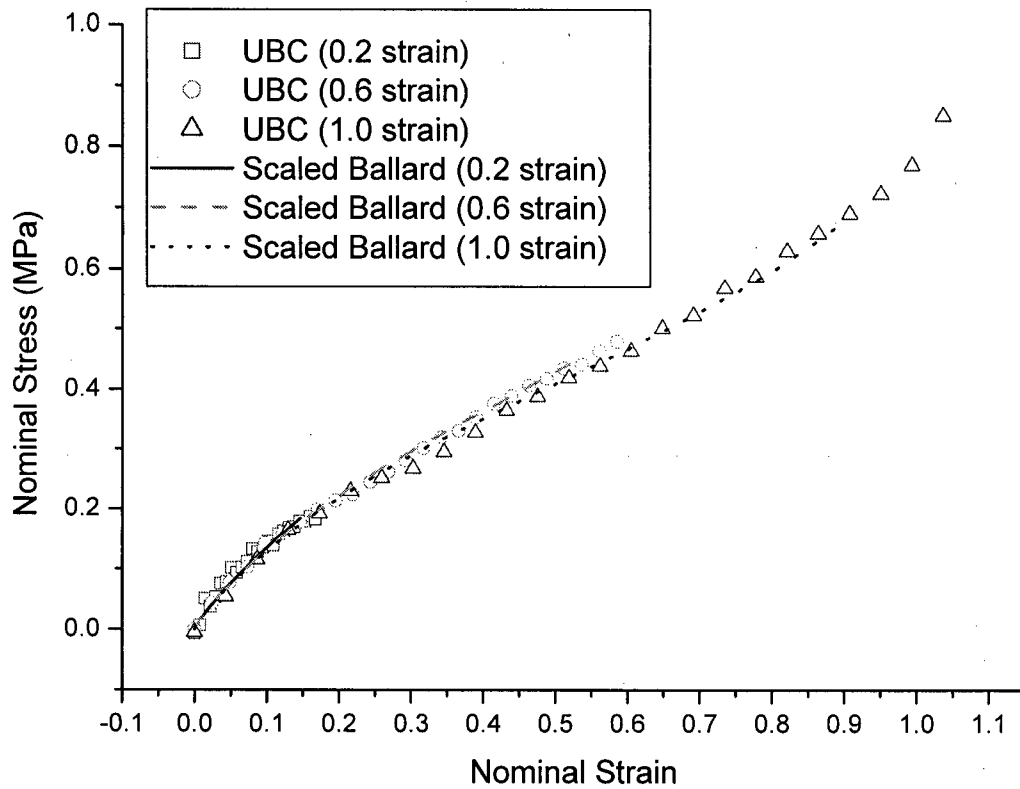


**Figure 4-18 Comparison of measured UBC data and the scaled Ballard data using the global scale factor in uniaxial tension tests**

In the absence of data to the contrary, it was assumed the global scale factor evaluated with uniaxial tension data was applicable for equibiaxial and planar tension data conversions. Thus, the following equation can be written for the equibiaxial tension data:

$$f_{B,UBC} = af_{B,Ballard} \quad \text{Eq 4-8}$$

Using the Mooney-Rivlin constitutive model evaluated for the Ballard uniaxial data gives:

$$f_{B,Ballard} \approx 2(\lambda_B - \lambda_B^{-5})(C_{10,B,Ballard} + \lambda_B^2 C_{01,B,Ballard}) \quad \text{Eq 4-9}$$

With substitution, the nominal equibiaxial stress expected for the material tested at UBC is given by the equation:

$$\begin{aligned}
f_{B,UBC} &= af_{B,Ballard} \approx a(2(\lambda_B - \lambda_B^{-5})(C_{10,B,Ballard} + \lambda_B^2 C_{01,B,Ballard})) \\
&= 2(\lambda_B - \lambda_B^{-5})(aC_{10,B,Ballard} + \lambda_B^2(aC_{01,B,Ballard})) \\
&= 2(\lambda_B - \lambda_B^{-5})(C_{10,B,UBC} + \lambda_B^2 C_{01,B,UBC})
\end{aligned}
\tag{Eq 4-10}$$

where  $f_{B,Axel}$  is the nominal equibiaxial stress measured by Ballard,  $f_{B,UBC}$  is the estimated nominal stress for the silicone tested at UBC,  $C_{10,B,Ballard}$  and  $C_{01,B,Ballard}$  are the material constants evaluated for the Ballard equibiaxial tension data, and  $C_{10,B,UBC}$  and  $C_{01,B,UBC}$  are equibiaxial material constants estimated for the silicone tested at UBC.

Equation 4-10 established an approach to estimate the Mooney-Rivlin equibiaxial tension material constants for the silicone tested at UBC, i.e.,  $C_{10,B,UBC} = aC_{10,B,Ballard}$  and  $C_{01,B,UBC} = aC_{01,B,Ballard}$ . Following a similar procedure, the Mooney-Rivlin planar tension material constants for the silicone tested at UBC were estimated using  $(C_{10} + C_{01})_{S,UBC} = a(C_{10} + C_{01})_{S,Ballard}$  (subscript S refers to planar tension). The estimated equibiaxial and planar tension constants are shown in Tables 4-9 and 4-10.

**Table 4-9 Estimated Mooney-Rivlin equibiaxial tension material constants at different strain levels for silicone tested at UBC**

Strain level	$C_{10}$ (MPa)	$C_{01}$ (MPa)
0.1	0.2744	1.04E-15
0.2	0.2608	1.17E-15
0.4	0.2418	1.78E-18
0.6	0.2071	0.0168
0.8	0.1752	0.0294
1.0	0.1724	0.0312

**Table 4-10 Estimated Mooney-Rivlin planar tension material constants at different strain levels for silicone tested at UBC**

Strain level	$C_{10} + C_{01}$ (MPa)
0.2	0.2343
0.4	0.2070
0.6	0.1992
0.8	0.1931
1.0	0.1909
2.0	0.1987

Though the material constants for equibiaxial and planar tensions estimated from the Ballard constants with the global scale factor are approximate, they provided a reference point for the unavailable experiments.

Material constants evaluated (or estimated) for different testing conditions are compared in Figure 4-19 for the silicone tested at UBC.

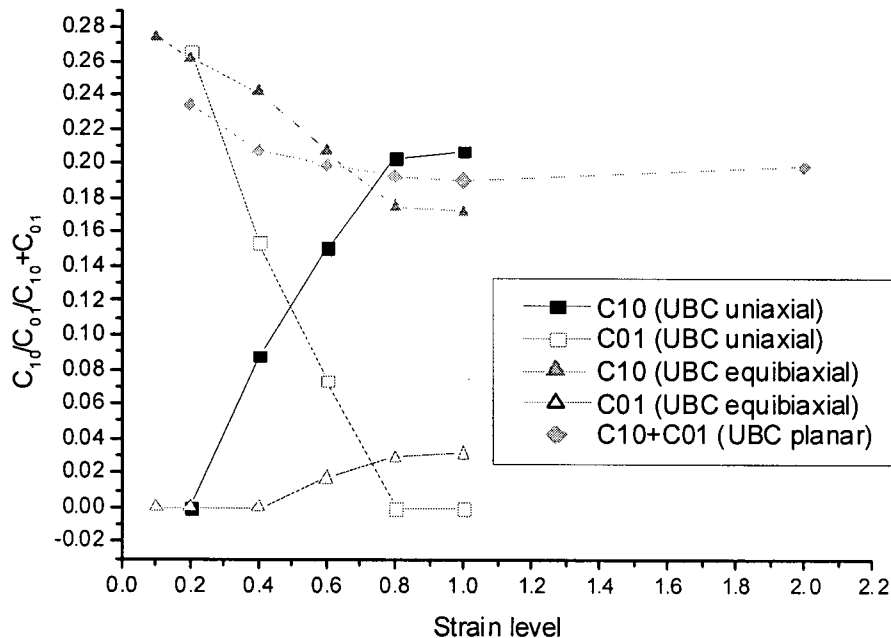


**Figure 4-19 Material constants evaluated or estimated for different testing conditions for the silicone tested at UBC**

### 4.3 SUMMARY

In order to characterize the material behaviour, Ballard Power Systems Inc. provided experimental data of a set of characterization tests for a silicone elastomer (Lot A), including uniaxial tension, equibiaxial tension and planar tension tests. Employing the Mooney-Rivlin constitutive model, material constants were developed for the different deformation modes and different strain levels individually. The material constants were calculated through least-square curve fitting using Origin. For all three deformation modes, the calculated material responses based on the Mooney-Rivlin constitutive model indicates a reasonable representation of the measured data at low or medium strain (<100%). However, large deviations occur at the highest strain level tested (200%). The material constants obtained for the three different loading modes show dependencies on testing conditions, including deformation modes and loading history.

Uniaxial tension tests were conducted at UBC with dogbone samples cut from silicone sheets (Lot B) provided by Ballard Power Systems Inc. The Mooney-Rivlin constants evaluated using the measured data showed a trend similar to that exhibited by the Ballard uniaxial tension samples. However, the data measured at UBC and Ballard differed in magnitude. It was assumed that the properties of the silicone changed significantly from lot to lot. Equibiaxial and planar tension tests could not be conducted at UBC. Therefore, a procedure was established to estimate the equibiaxial and planar material constants for the new silicone sheets from the Ballard data to provide a reference characterization for these unavailable experiments.

## **5 EXPERIMENTAL MEASUREMENTS**

During the three standard mechanical characterization tests for elastomeric materials, the deformation within the gauge-length of the sample is uniform, i.e. the strain magnitude and deformation mode do not change with location. Moreover, the three principal strain components have simple correlations with each other. However, for most real components under operational loading, the deformation is not as simple. Non-uniform and multiaxial strain states are expected. In order to investigate non-uniform and multiaxial strain, two types of samples, a tapered dogbone sample and a cross sample, were designed for experimental measurements. As demonstrated in the following sections, the deformation of the tapered dogbone sample is non-uniform, while the deformation of the cross sample is non-uniform and multiaxial.

In this work, samples were cut from the silicone sheets (Lot B) provided by Ballard Power Systems Inc. for these experimental measurements. Mechanical tests were conducted with tapered dogbone samples (in uniaxial tension) and cross samples (in biaxial tension). Both tests were conducted with a low strain rate and the material response obtained was considered to be equilibrium response.

### ***5.1 UNIAXIAL TENSION TEST FOR TAPERED DOG-BONE SAMPLE***

#### ***5.1.1 Testing Method***

A tapered dogbone sample was designed based on the regular straight dogbone sample used for uniaxial tension tests. In these samples the gauge-length width was tapered to produce non-uniform strain conditions. Based on the sample geometry, the expected reaction force and available instrumentation, these samples were tested on the Minimat 2000 (Rheometrics Scientific Inc.) A rule die was used to cut the tapered dogbone samples from the silicone sheets with the geometry shown in Figure 5-1.

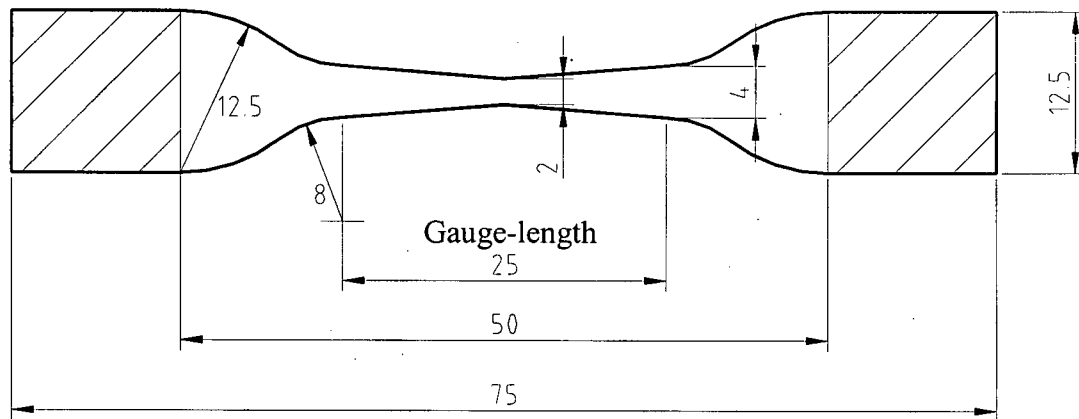


**Figure 5-1** Geometry of tapered dogbone sample in UBC uniaxial tension test (unit: mm, Sample thickness=1.0mm)

The testing setup (including load cell, strain rate and testing temperature) for the tapered dogbone samples were the same as those described for the straight dogbone samples in Chapter 4. The testing procedure was similar, except for the addition of one step: when the maximum strain was reached at each strain level on the fifth cycle, the crosshead position was held for 100sec. During this period, the forces were recorded. The average measured force during this hold was considered the reaction force at the maximum strain for the strain level. This additional step was added to provide more accurate measurement of the reaction force at each strain maximum by giving enough data to calculate an average force. After measuring the force for each strain level, samples were unloaded to zero displacement and then loaded to a higher strain level. The displacements applied in the gauge length were 2.5mm, 5.0mm, 7.5mm, 10.0mm, 12.5mm and 15.0mm. In total, five samples were tested.

Similar to the procedure used for the straight dogbone samples, a caliper was used to measure the displacement. The same template described in Chapter 4 was used to mark the tapered dogbone samples with lines at known distances. A marked tapered dogbone sample is shown in Figure 5-2. The shaded areas shown in Figure 5-1 were used for gripping. When the sample was strained to a particular strain level for the fifth time, the strain was held and the displacement between the different reference lines was measured

using a caliper. Figure 5-3 shows the locations of reference lines and indicates the distances that were measured (the original distances are marked in the parentheses in mm). Pictures of the deformed samples were also taken for further analysis of the strain profile.

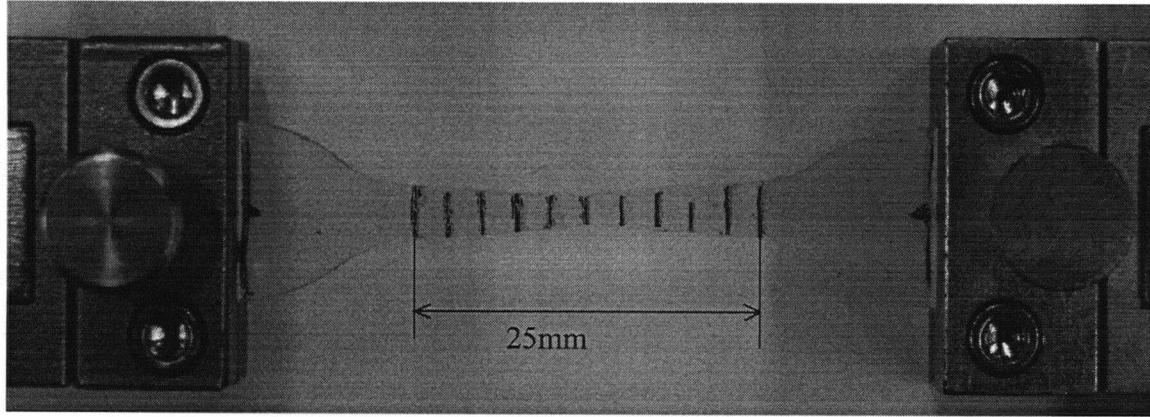


Figure 5-2 Marked tapered dogbone sample for UBC uniaxial tension tests

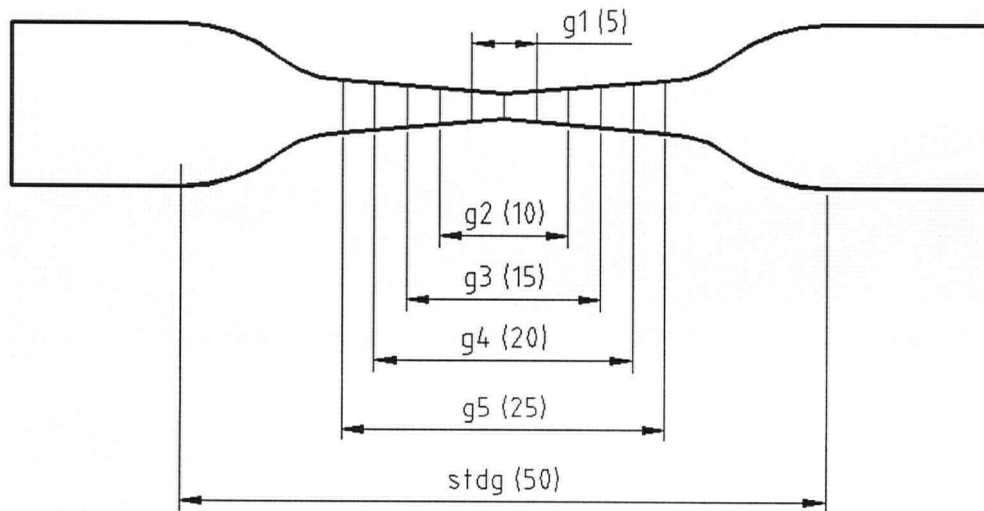
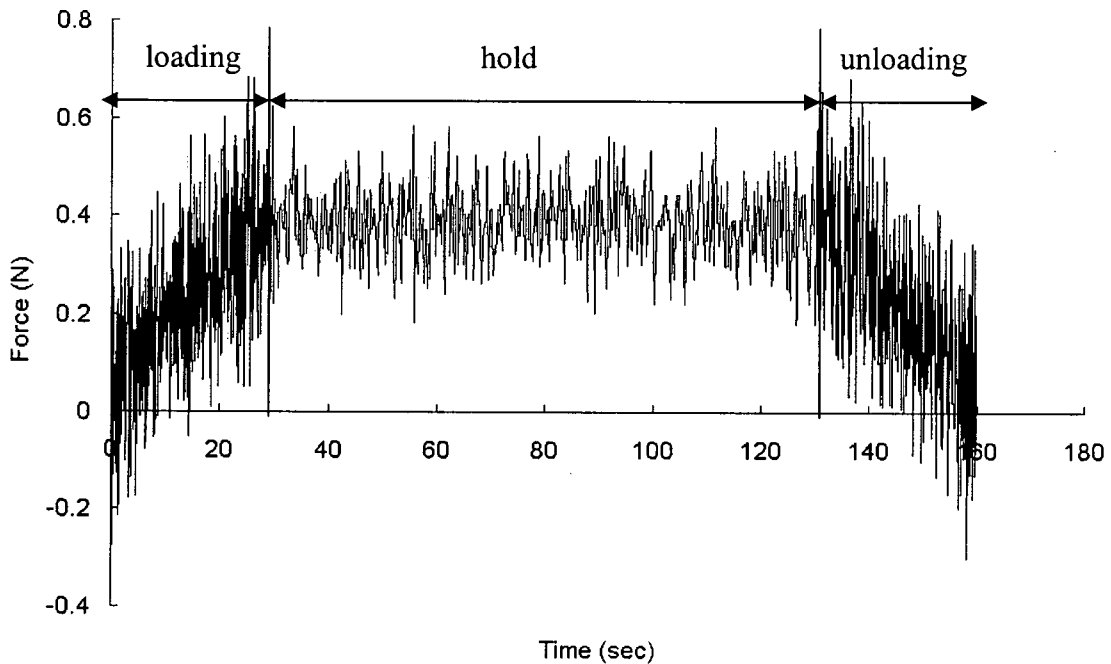


Figure 5-3 Locations of reference lines from where the distances were measured in uniaxial tension of tapered dogbone sample

### 5.1.2 Experimental Results

The measured force-time (or force-displacement) curve exhibited considerable oscillations. The force – time profile measured for one sample when a 2.5mm

displacement was applied to the gauge length is given in Figure 5-4 as an example. Considering the noise shown in Figure 5-4, measuring the force at a specific time was unreliable and does not give accurate information about the instantaneous force. To evaluate the maximum force at each strain level, an average force was calculated from the data measured during the 100s hold. The measured average reaction forces at different displacements are shown in Figure 5-5. The displacements plotted on X-axis were measured across “stdg” as marked in Figure 5-3. The data measured from the five tested samples shows the force-displacement correlation consistently.



**Figure 5-4 Force-time profile for a 2.5mm gauge-length displacement in uniaxial tension of tapered dogbone sample**

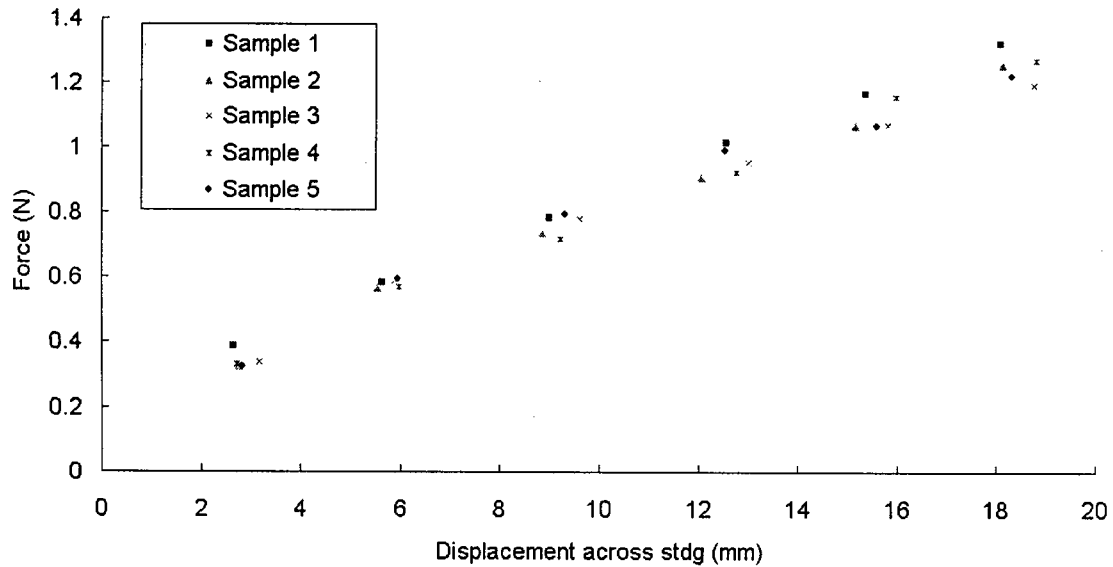


**Figure 5-5 Measured reaction force – displacement results for uniaxial tension of tapered dogbone sample**

In addition to forces, the distances between the different reference lines were measured within the gauge-length area (referring to Figure 5-3). These distance measurements are shown in Figure 5-6. Figure 5-7 shows an example of a deformed sample when a 15mm displacement was applied to the gauge-length area. Figure 5-7 shows that the initially evenly distributed lines in the gauge-length area are no longer equidistant. The interval in the center area is larger than the interval in the outer area. These distances shown in Figure 5-6 increase linearly with the increment of the stdg displacement approximately. However, the incremental rates (reflected by the slopes of different straight lines) are different.

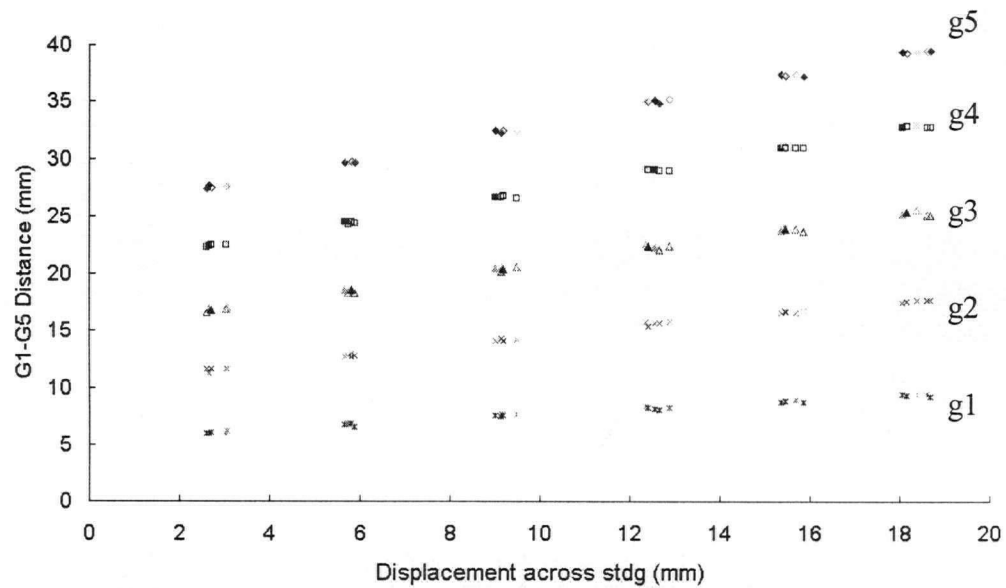


Figure 5-6 Measured distances between different reference lines throughout the deformed tapered dogbone sample

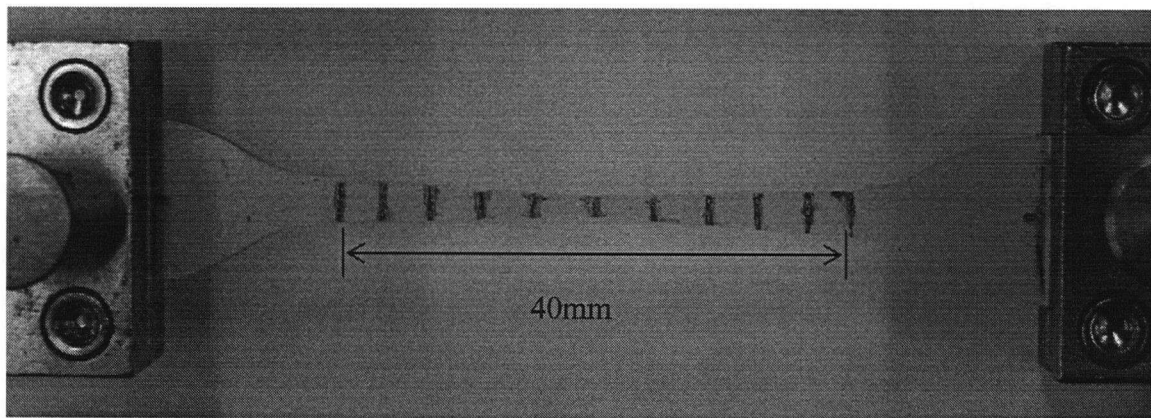
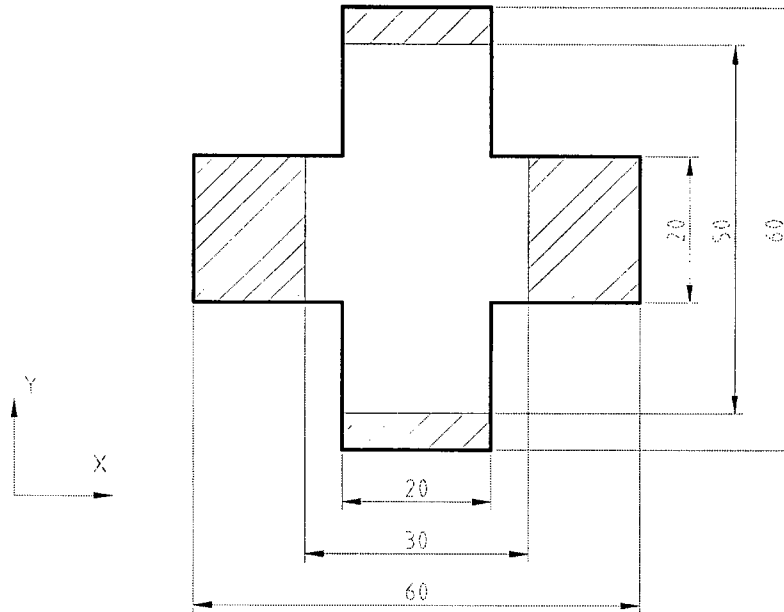


Figure 5-7 Photograph of deformed tapered dogbone sample in uniaxial tension with a 15mm displacement applied to the gauge-length area (marked as g5 in Figure 5-3)

## 5.2 BIAXIAL TENSION TEST FOR CROSS SAMPLE

### 5.2.1 Testing Method

A rule die was provided by Ballard for cutting cross samples from the silicone sheets with the geometry shown in Figure 5-8.



**Figure 5-8 Geometry of cross sample in UBC biaxial tension test (unit: mm, Sample thickness=1.0mm)**

The cross samples were designed with four tabs, which made it possible to load these samples biaxially. By applying different loads to the two perpendicular directions, a multiaxial strain, which is none of the three standard strain types, was expected. Unfortunately, robust facilities were not available to perform this biaxial loading. Instead, a custom grip was designed to pre-load samples in one direction before they were loaded in another direction. Considering the sample geometry, the expected reaction forces and available instrumentation, the cross samples were tested using a MTS load frame (MTS Systems Corporation) with an Instron controller (Instron Corporation) available at UBC. A 5000N load cell and a crosshead speed was 2mm/s were used. Testing temperature was about 20-23°C. The testing temperature was slightly higher compared with that during the other UBC tests.

The cross samples were loaded in two directions using a special grip designed to pre-load the sample in the x-direction and the MTS testing machine to load in the y-direction. The grip was formed with two different halves (the geometry of the grip is given as the appendix). Four bolts linked two grip sections together to form the pre-loading grip. By



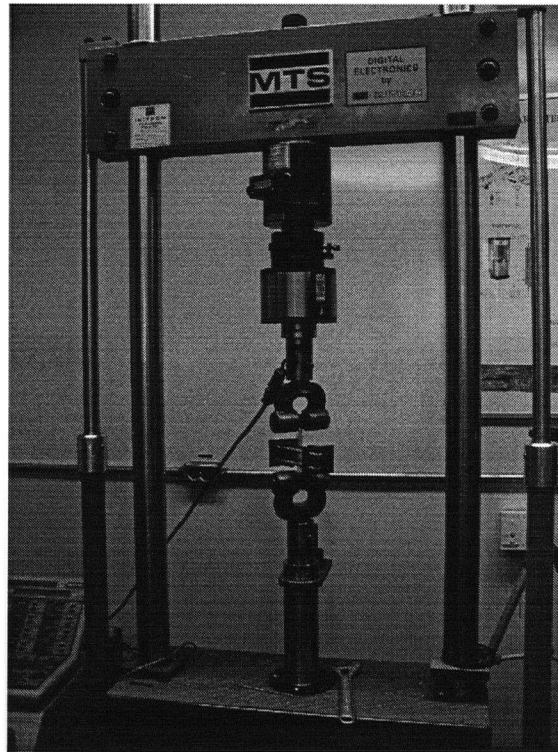


Figure 5-10 Photograph of the biaxial tension experiment setup at UBC

In order to quantitatively demonstrate the deformation without video or contact extensometers, the cross samples were marked with reference lines before testing. The line pattern marked on the cross samples formed a reference “web” as shown in Figure 5-11. The original distance between each adjacent line was 5mm.

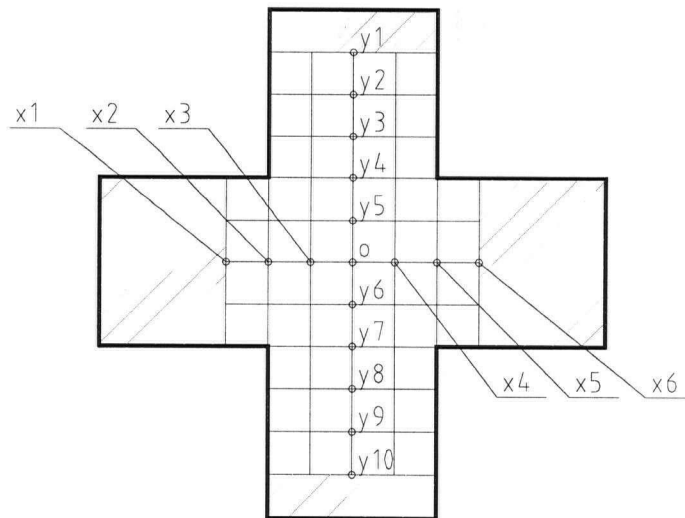


Figure 5-11 Marked cross sample in biaxial tension

The cross samples were initially pre-conditioned on the MTS machine in the x-direction. Although the strain in the loading direction was not uniform, the average strain was defined by normalizing the length change of the gauge-length by its original length for further reference. The displacements measured between points x1 and x6 in the x-direction were 6mm, 12mm and 18mm. The corresponding pre-conditioning strains were 20%, 40% and 60%. After the pre-condition procedure, the samples were placed in the crosswise grips, whose positions were adjusted according to the pre-conditioning strain. After pre-loading, the samples were loaded in the y-direction by the MTS machine. The test procedure for loading the cross samples in the y-direction was similar to that of loading the tapered dogbone samples. The cross samples were loaded to a particular strain level followed by a complete unloading to zero displacement five times. At the maximum displacement for each strain level on the fifth cycle, the crosshead position was held for 50s. The average measured force was calculated as the reaction force at the maximum displacement for each strain level. The displacements measured between points y1 and y10, as marked in Figure 5-11, were 10 mm, 20mm, 30mm, and 40mm. The average strain was calculated using the applied displacement and the original gauge-length in the y-direction. The corresponding strains were 20%, 40%, 60% and 80%. A total of three samples were tested in this manner.

One drawback of the testing method was that the crosswise grips blocked access to the sample during test. Thus it was difficult to use a caliper to measure the deformation in the samples. Only the distance between y1 and y10 (referring to Figure 5-12) could be reliably measured by a caliper. For the other locations, deformations were calculated from pictures. A scientific image processing software, Quartz PCI 4.0 (Quartz Imaging Corporation), was used to measure distance from picture.

### **5.2.2 Experimental Results**

Details of the cross sample tests are summarized in Table 5-1. It should be noted that not all desired strain levels in y-direction were completed in these experiments because some samples failed before completing the fifth loading cycle at 40mm displacement in the y-direction. These samples were failed near the MTS machine grips. The grips used in this

test were not designed for use in testing elastomers. The main drawback was that the friction between the gripped area and the sample surface was not high enough. Additionally, the crosswise grips blocked access to the sample, which made the gripped areas in the y-direction very small. In order to prevent the sample from slipping out of the grip, a high clamping force was applied to the sample via the grips. The sharp edge of the grip created small cuts in the sample. After several loading-unloading cycles, the small cuts resulted in sample failure. Figure 5-12 shows an example of sample failure in progress. Figure 5-12 also demonstrates another drawback of this testing method: no support of the crosswise grips could be provided during testing, therefore the weight of the crosswise grips must be considered.

**Table 5-1 Summary of accomplished tests in biaxial tension of cross sample**

(a) x displacement = 6mm (20% strain)

Y Disp. (mm)	Sample		
	C1	C2	C3
10 (20% strain)	✓	✓	✓
20 (40% strain)	✓	✓	✓
30 (60% strain)	broken during the 5th loading	✓	✓
40 (80% strain)		broken during the 3rd unloading	broken during the 4th unloading

(b) x displacement = 12mm (40% strain)

Y Disp. (mm)	Sample		
	C1	C2	C3
10 (20% strain)	✓	✓	✓
20 (40% strain)	✓	✓	✓
30 (60% strain)	✓	broken during the 2nd unloading	✓
40 (80% strain)	broken during the 1st unloading		broken during the 1st loading

(c) x displacement = 18mm (60% strain)

Y Disp. (mm)	Sample		
	C1	C2	C3
10 (20% strain)	✓	✓	✓
20 (40% strain)	✓	✓	✓
30 (60% strain)	✓	✓	✓
40 (80% strain)	broken during the 3rd loading	✓	✓

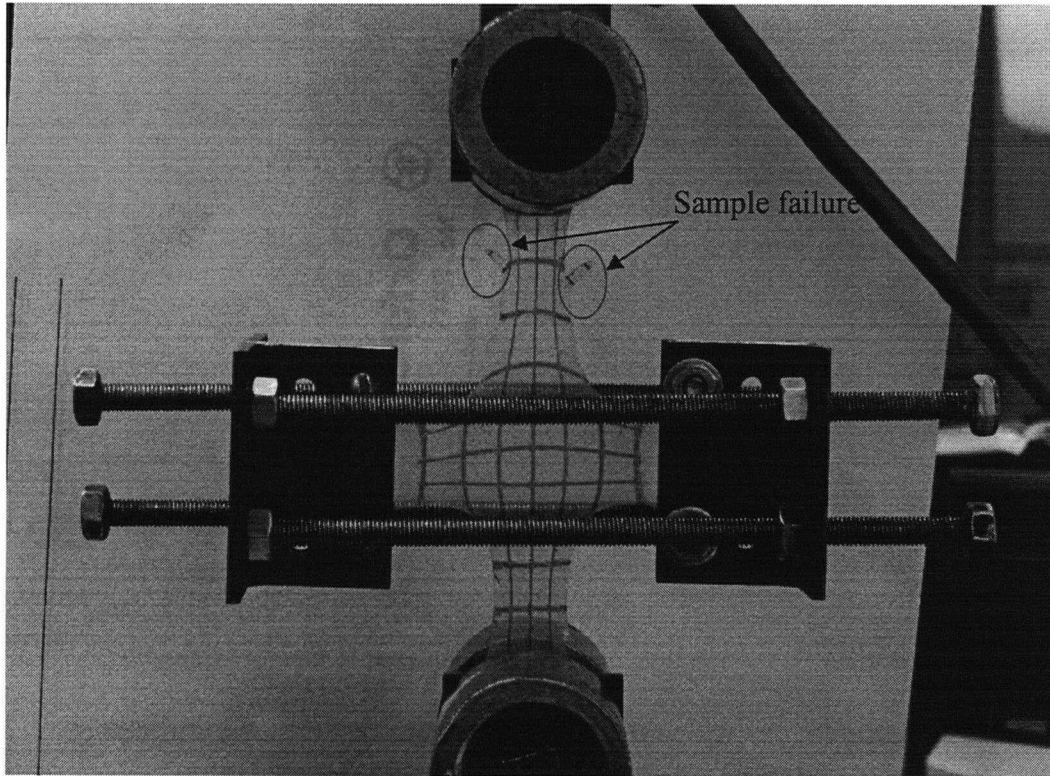


Figure 5-12 Sample failure in progress in biaxial tension tests

The measured reaction forces for different displacements are shown in Figure 5-13. The displacements plotted on X-axis were measured between points y1 and y10 as marked in Figure 5-11.

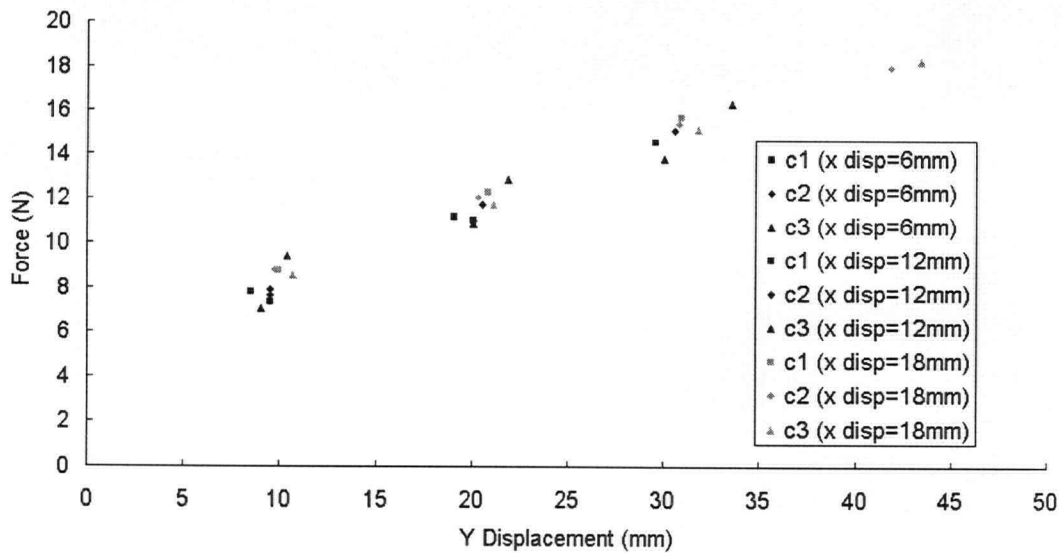
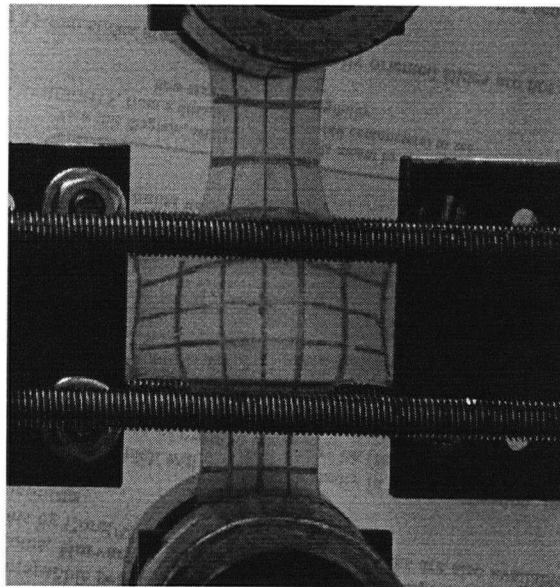
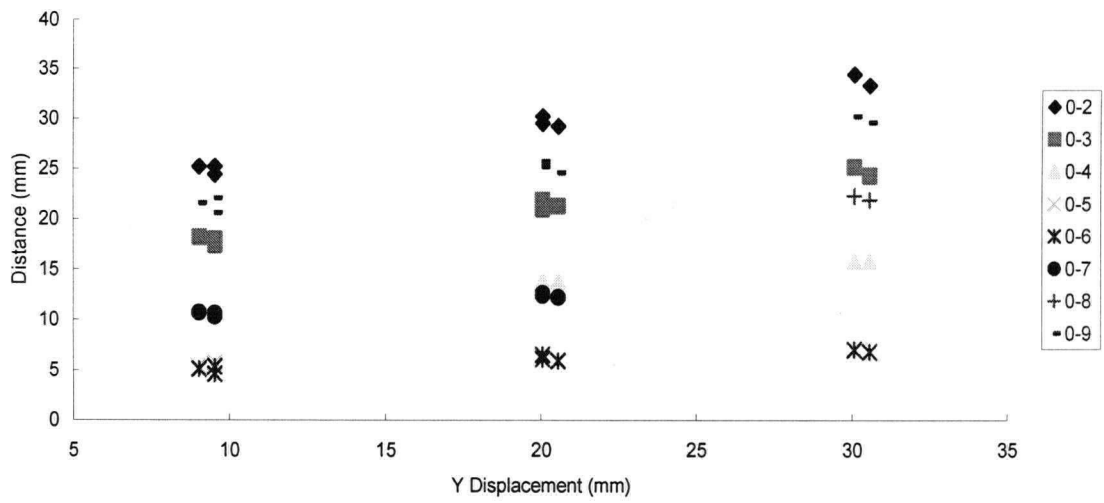


Figure 5-13 Measured reaction force – displacement results for biaxial tension of cross sample

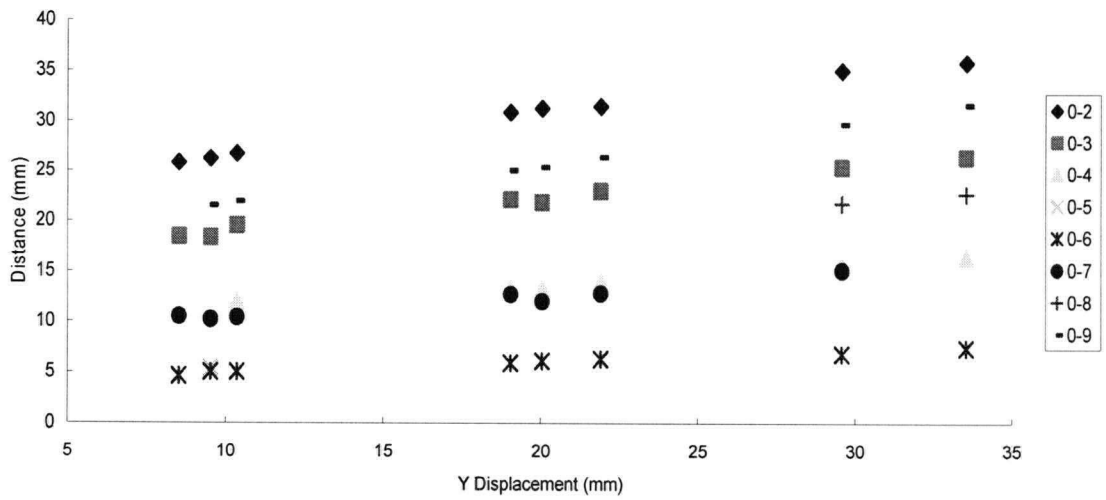
Figure 5-14 shows a photograph of the deformed cross sample. The initially identical squares are skewed. The squares at different location are deformed to different shapes, which demonstrates that the deformation is non-uniform and multiaxial. Distances between the reference lines within the gauge-length area were measured from digital pictures (referring to Figure 5-11). The results of these measurements are shown in Figure 5-15. The name of each series shown in the legend indicates the starting and ending points of the distance measured. For example, “0-2” means the distance was measured between “0” and “y2” (referring to Figure 5-11). The distances shown in Figure 5-15 increase approximately linearly with the increment of the displacement in the y-direction. However, the incremental rates (reflected by the slopes of different straight lines) were different.



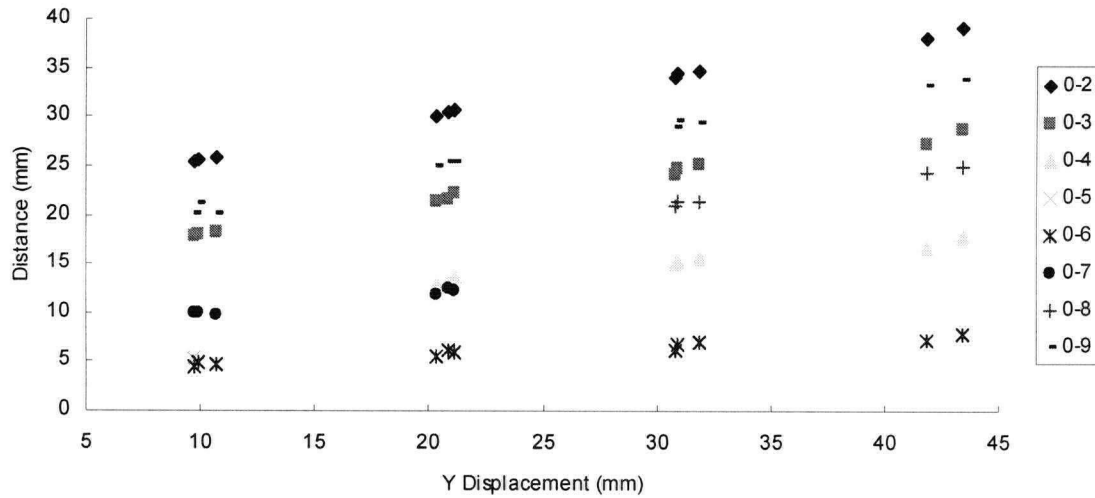
**Figure 5-14** Photograph of a deformed cross sample in biaxial tension



(a) X displacement = 6mm



(b) X displacement = 12mm



(c) X displacement = 18mm

**Figure 5-15 Measured distances across different reference points throughout the deformed cross samples**

### 5.3 SUMMARY

The tapered dogbone samples and cross samples were cut from silicone sheets provide by Ballard using rule dies. They were designed to exhibit non-uniform and multiaxial deformations. The tapered dogbone samples were tested on the Minimat, while the cross samples were tested on the testing machine using a specially designed grip to apply the crosswise displacement. After obtaining stable behaviours, the force-displacement correlations and sample deformations were measured during both experiments. The measured results will be compared with numerical results and more details will be discussed in Chapter 7.

## **6 MODEL DEVELOPMENT**

Similar to the constitutive material properties of an elastomeric material, the evolution of stress and strain is nonlinear in mechanical analysis for a component, i.e. the relationship between the applied loads and the deformation response is not constant. Strain dependence of the constitutive material behaviour is the major source of this nonlinearity. The finite element method (FEM) provides a convenient procedure to mathematically model the mechanical behaviour of an elastomeric material. The finite element method is a computer-aided engineering technique for obtaining approximate numerical solutions to boundary value problems which predict the response of physical systems subjected to external loads. It is based on the principle of virtual work<sup>37</sup>. A domain of interest is discretized into an assembly of finite elements. Approximating functions based on nodal values of the physical field variable are sought and used to describe the variation within an element. In a mechanical analysis, the unknowns are the nodal degrees of freedom, such as displacements, rotations. In FEM, piece-wise approximation of physical fields in the elements provides good precision even with simple approximating functions.<sup>38</sup>

ABAQUS, was employed as a solution platform for the current investigation. ABAQUS was chosen because it provides highly developed non-linear solution capabilities and a well-documented method for extending the program's capabilities via user written subroutines.

Two techniques, a non-uniform strain technique and a strain partitioning technique, were proposed to extend the capability of the standard Mooney-Rivlin constitutive model. The non-uniform strain technique is needed to characterize the non-uniform strain within the deformed sample, while the strain partitioning technique is used to characterize the multiaxial strains within the deformed sample. Together, these techniques provide a useful tool to describe constitutive behaviour of elastomeric materials during non-uniform and multiaxial deformation conditions. Taking the Mooney-Rivlin constitutive model with the special techniques as an input, a mathematical mechanical model was developed to predict the stress development in an elastomer component as it is deformed.

## **6.1 GENERAL MECHANICAL MODEL FORMULATION**

In an FEM mechanical analysis, the solution variables, stored as a vector at the nodes, are the components of displacement and rotation. Prescribed forces are defined as loads and prescribed displacements are defined as boundary conditions. In order to calculate the evolution of stress and strain, it is necessary to satisfy the differential equations of equilibrium based on a force balance on an elemental volume and to satisfy the conditions of compatibility based on the displacement field at every point within the body.

ABAQUS uses a modified Newton solution method to solve the nonlinear equilibrium equations and ensure overall equilibrium of the solution<sup>28</sup>. The modified Newton method is an incremental solution algorithm that employs a series of piecewise linear FEM approximation to approach a solution. An acceptable solution is obtained when the change in incremental solutions becomes small relative to some tolerance. The reader is referred to the text by Zienkiewicz and Taylor for a complete explanation and discussion of the issues relating to the finite element solution procedure<sup>39</sup>. A detailed description of the application of the FEM to mechanical analysis will not be presented because the algorithm was not developed during the course of this research project.

In order to predict mechanical behaviours of an elastomeric material, ABAQUS provides a specific material module, called hyperelastic constitutive material model. The constitutive model describing basic material behaviour is used as an input of a mechanical model to calculate the deformation within the geometry by satisfying prescribed forces and boundary conditions. The constitutive models available in ABAQUS for nearly incompressible elastomeric materials are all based on strain energy functions. A user can choose one of the available standard strain energy functions. The material constants in the chosen strain energy function are determined by direct input or regression analysis using experimental data. Although the constitutive material behaviour changes with loading variables, the standard constitutive models available in ABAQUS do not provide a means to alter the material constants during an analysis. When a standard hyperelastic material constitutive model is employed, the strain energy is calculated at each integration point during each time increment using the pre-defined

material constants. Beyond providing the standard constitutive models, ABAQUS allows users to design user-subroutine to calculate the strain energy function according to any form. In this manner, the user-subroutine option provides the possibility to improve the constitutive model accuracy by modifying strain energy functions or the way they are applied. As discussed in the following sections, two techniques were developed to extend the capability of the standard Mooney-Rivlin constitutive model.

In order to simplify description, when the standard Mooney-Rivlin constitutive model is combined with the two proposed techniques, it is referred to as the modified Mooney-Rivlin constitutive model. However, no new form of strain energy function is proposed. The modified Mooney-Rivlin constitutive model means applying the standard Mooney-Rivlin model in a unique way.

## **6.2 NON-UNIFORM STRAIN TECHNIQUE**

ABAQUS provides the standard Mooney-Rivlin hyperelastic constitutive material model as a built-in material model. In order to use this constitutive model, material constants or experimental data for one or more particular deformation modes must be provided as an input before an analysis. When material constants, evaluated for a certain strain level, are used incorrectly, large errors may occur. Figure 6-1 gives an example of the error which may be introduced by using inappropriate material constants, where the calculated (taking Equation 4-1) and measured stress-strain curves for a strain of 1.0 from the Ballard uniaxial tension tests are compared. The calculated curves are based on the Mooney-Rivlin constitutive model with material constants evaluated at strains of 0.2 and 1.0. The calculated stress-strain curve taking the material constants at the strain of 0.2 shows a large deviation from the measured stress-strain curve.

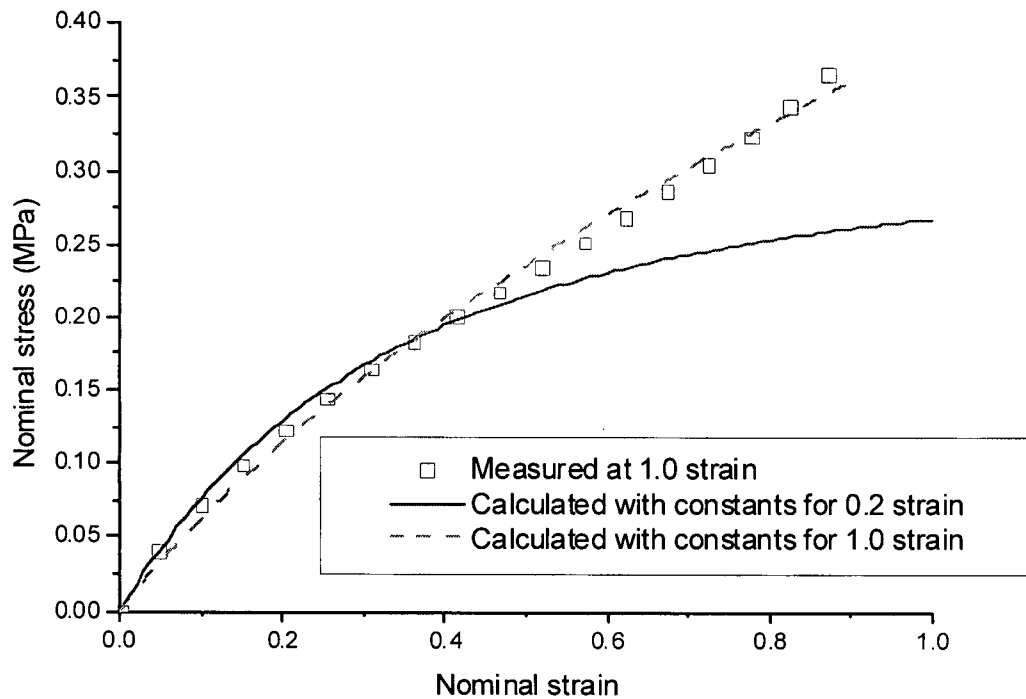


**Figure 6-1 Comparison of the measured and the calculated stress-strain curves in Ballard uniaxial tension tests**

The three standard characterization tests (uniaxial, equibiaxial, and planar tensions) are designed to produce uniform strain within the gauge-length of a sample. For these tests uniform material constants can be used with minimum difficulty. However, in non-idealized cases, such as exist in complex geometry or for non-uniform loading, strain distribution may result. As discussed in Chapter 5, Figure 5-7 shows the deformation of the tapered dogbone sample is a simple example exhibiting a non-uniform strain distribution.

Since the material constants in the standard Mooney-Rivlin constitutive model are independent of the strain levels experienced during an analysis, it gives good representation only when the strain is uniform within the deformed body. Furthermore, since the appropriate material constants must be selected prior to a run, the strain level must be determined before numerical simulation. Predetermination of the strain level is

not realistic for most components under operational loading. Using the tapered dogbone sample as an example, when a particular displacement was applied to the gripped ends, it is difficult to predict the strain level before numerical simulation or experiment. In order to deal with this problem, the material constants should be determined locally according to the local strain level. This method is being called the non-uniform strain technique.

An ABAQUS user-subroutine was developed to apply the non-uniform technique with the standard Mooney-Rivlin constitutive model. By determining the local strain level at each integration point at each time step and selecting the appropriate material constants, the need to determine the strain levels and specify the constants in advance is avoided. To apply the non-uniform strain technique, a set of standard material constants evaluated for a range of strains is interpolated locally based on the strain level at each material integration point within the computation domain. If the local strain level is  $\varepsilon$ , the series of strain levels performed in the standard material characterization tests in a particular deformation mode is  $\varepsilon_i$  ( $i=1..N$ ,  $N$  is the number of tested strain levels), and  $C_{10,i}$  and  $C_{01,i}$  are the Mooney-Rivlin material constants evaluated at the strain level of  $\varepsilon_i$ , then the local material constants,  $C_{10}$  and  $C_{01}$ , are determined as:

$$\begin{aligned}
 C_{10} &= C_{10,1}, C_{01} = C_{01,1}; \varepsilon < \varepsilon_1 \\
 C_{10} &= C_{10,i-1} + (\varepsilon - \varepsilon_{i-1}) \frac{C_{10,i} - C_{10,i-1}}{\varepsilon_i - \varepsilon_{i-1}}, C_{01} = C_{01,i-1} + (\varepsilon - \varepsilon_{i-1}) \frac{C_{01,i} - C_{01,i-1}}{\varepsilon_i - \varepsilon_{i-1}}; \varepsilon_{i-1} < \varepsilon < \varepsilon_i \\
 C_{10} &= C_{10,N}, C_{01} = C_{01,N}; \varepsilon > \varepsilon_N
 \end{aligned}
 \tag{Eq 6-1}$$

### 6.3 STRAIN PARTITIONING TECHNIQUE

In addition to the maximum strain levels experienced, an elastomeric material's response varies with deformation mode. When material constants evaluated at a particular deformation mode are used incorrectly, large errors may result. As demonstrated in Figure 6-2, the measured equibiaxial material response is different than the calculated response (using Equation 4-3) for material constants evaluated for uniaxial tension (Ballard tests at 0.8 strain).

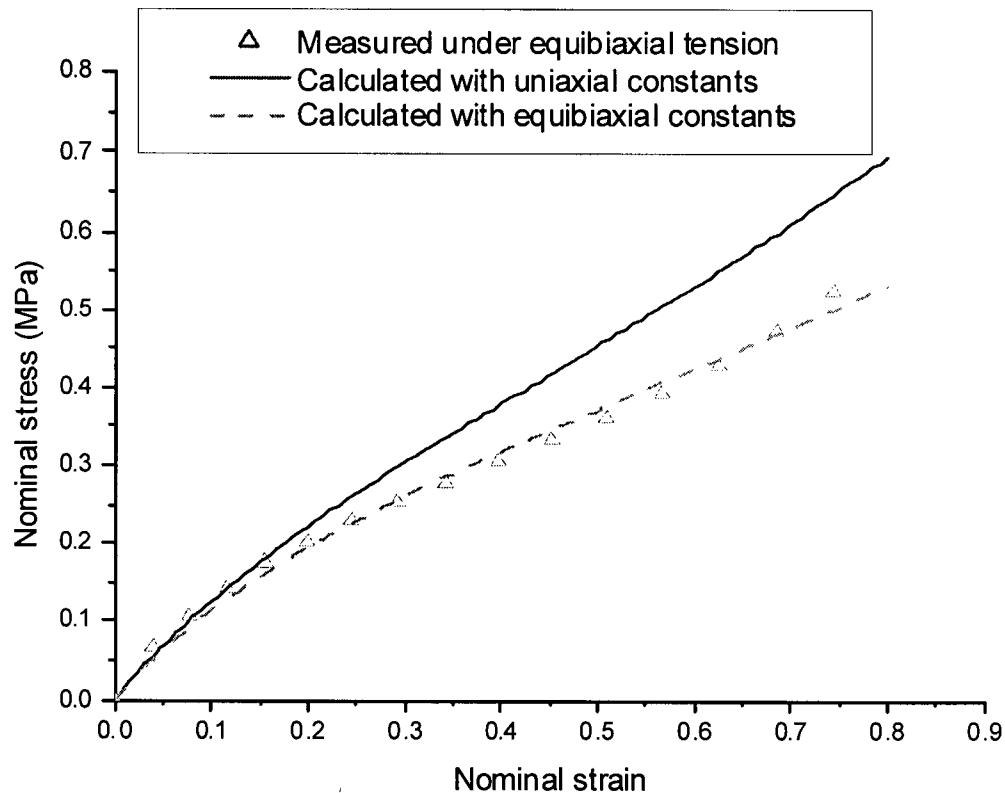


**Figure 6-2 Comparison of measured and calculated stress-strain curves in the Ballard equibiaxial tension tests**

The standard Mooney-Rivlin constitutive model built in ABAQUS does not vary the material constants according to the deformation mode during an analysis. In order to define the appropriate material constants, the deformation mode must first be determined. For components with simple geometry under simple loading, the deformation mode falls into one of the three standard deformation modes. However, it is often difficult to tell the deformation mode for a complex geometry and/or for complicated operational loading conditions. In these cases, the strain state may not fall completely into one of the three standard types. The deformation of the cross sample, shown in Figure 5-14, is an example of the complex deformation modes which can evolve.

An arbitrary deformation can be represented by the principal stretches. As material behaviour changes with deformation mode, it is desirable to evaluate the material

behaviour in an arbitrary deformation according to the material behaviours in the standard deformations. The idea of breaking an arbitrary deformation into components showing the effects of the three standard deformations comes up, which is called the strain partitioning technique. Applying this technique, a general deformation represented by three principal stretches is partitioned into stretch components, each of which corresponds to one of the three basic deformation modes. Since the strain energy is additive, it is possible to calculate the total strain energy from the partitioned strain energies. If the general deformation is one of the standard types, the partitioned results should reflect only this type of deformation. Otherwise, the partitioned results should reflect a combination of different deformations.

In order to partition an arbitrary deformation represented by principal nominal stretches  $(\lambda_1, \lambda_2, \lambda_3, \text{ where } \lambda_1 \geq \lambda_2 \geq \lambda_3)$ , into the form of three standard deformation stretches, the component stretch directions are defined as shown in Figure 6-3.

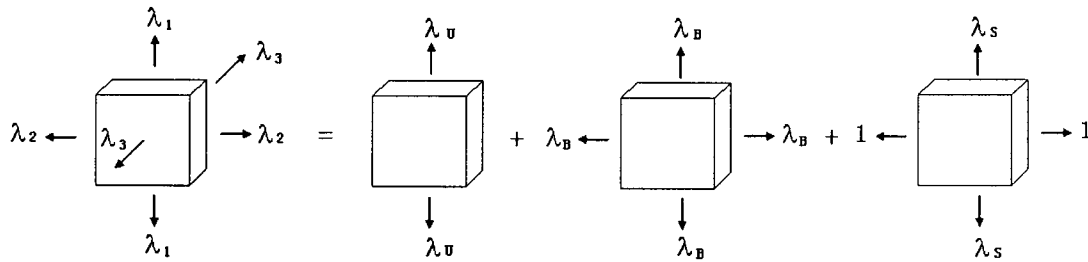


**Figure 6-3 Stretch component directions (the subscript U refers to uniaxial tension, B refers to equibiaxial tension and S refers to planar tension)**

If the component stretch directions are defined as shown in Figure 6-3, the following equations can be written

$$\lambda_1 = 1 + (\lambda_U - 1) + (\lambda_B - 1) + (\lambda_S - 1) \tag{Eq 6-2}$$

$$\lambda_2 = 1 + (1/\sqrt{\lambda_U} - 1) + (\lambda_B - 1) \tag{Eq 6-3}$$

$$\lambda_3 = 1 + (1/\sqrt{\lambda_U} - 1) + (1/\lambda_B^2 - 1) + (1/\lambda_S - 1) \tag{Eq 6-4}$$

$\lambda_U, \lambda_B$  and  $\lambda_S$  represent the amount of each standard deformation. With the help of Maple (Maplesoft Co.), the analytical solutions of Equations 6-2 - 6-4 can be found. According to the analytical solutions given by Maple, in the form of a symbolic expression in terms of  $\lambda_1, \lambda_2, \lambda_3$ , an algorithm was developed to find the individual standard stretches,  $\lambda_U, \lambda_B$  and  $\lambda_S$ .

Assuming additivity of the strain energy, once  $(\lambda_1, \lambda_2, \lambda_3)$  is partitioned, the strain energy  $W$  of the arbitrary deformation mode can be calculated according to the following expression.

$$W = W_U + W_B + W_S \quad \text{Eq 6-5}$$

The strain energy components of the partitioned deformations can be calculated taking material constants evaluated for standard tests. For the three basic loading modes,  $W_U, W_B$ , and  $W_S$  can be calculated according to the following equation:

$$W_X = C_{10,X}(I_{1,X} - 3) + C_{01,X}(I_{2,X} - 3) \quad \text{Eq 6-6}$$

where

$$X=U, B, S$$

$$I_{1,U} = \lambda_U^2 + 2/\lambda_U, \quad I_{2,U} = \lambda_U^{-2} + 2\lambda_U$$

$$I_{1,B} = 2\lambda_B^2 + \frac{1}{\lambda_B^4}, \quad I_{2,B} = \frac{2}{\lambda_B^2} + \lambda_B^4$$

$$I_{1,S} = I_{2,S} = \lambda_S^2 + \frac{1}{\lambda_S^2} + 1$$

$C_{10,X}$  and  $C_{01,X}$  are the material constants for the three standard tests.

### 6.3.1 Multiple Partitioned Results

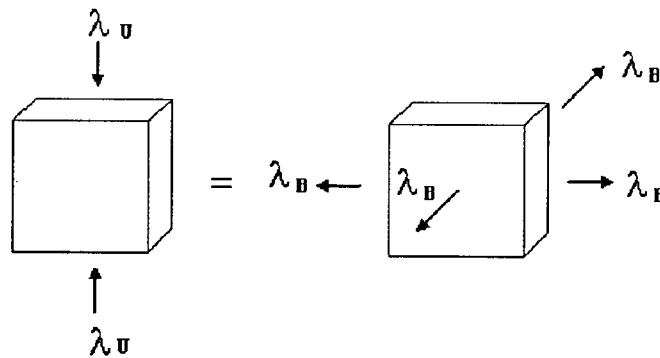
The set of nonlinear equations, Equations 6-2 – 6-4, must be solved to determine the partitioned stretches. For certain conditions, solving these equations results in multiple solutions. In order to apply the strain partitioning technique correctly, the most reasonable solution must be determined. A set of rules have been developed to choose the solution:

- (1) Only real number solutions are considered. Complex number solutions are ignored.
- (2) Solutions with tensile partitioned stretches ( $\lambda_X \geq 1$ ,  $X=U, B$ , and  $S$ ) are preferred: the solution with the maximum number of tensile partitioned stretches will be chosen. This rule reflects that only tensile tests have been conducted for standard deformation modes. Compressive components may introduce error.
- (3) The solution with the largest uniaxial tension component is favoured: if two solutions have the identical number of tensile partitioned stretches, the solution with the larger  $\lambda_U$  will be chosen. This reflects that the measured data for uniaxial tension is generally more accurate compared with that for equibiaxial tension and planar tension.

### 6.3.2 Equivalent Deformation Modes

Only standard tensile tests have been conducted to characterize the material behaviour. The material constants for compressive deformations are not available. However, in some cases having a compressive component of the partitioned deformation cannot be avoided. For compressive strains, equivalent tensile deformation modes have been defined as shown in Figure 6-6.

Figure 6-6 shows the compressive deformation modes and the equivalent tensile deformation cases. If compressive components are found in partitioned stretch results, the equivalent tensile deformations are sought. Following this conversion, the partitioned strain energy component is evaluated according to the material constants for the strain level at the equivalent deformation.



(a) Uniaxial compression,  $\lambda_B = \frac{1}{\sqrt{\lambda_U}}$

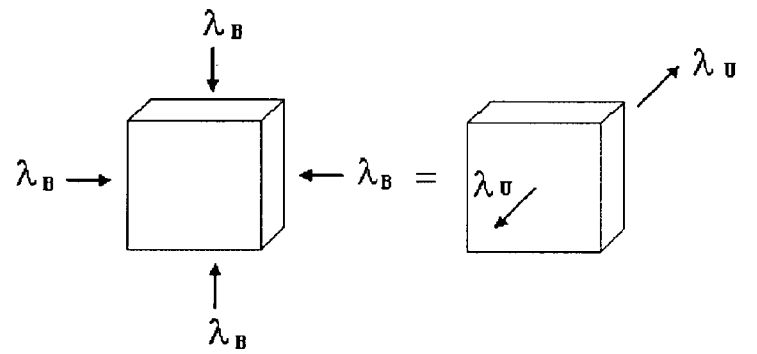
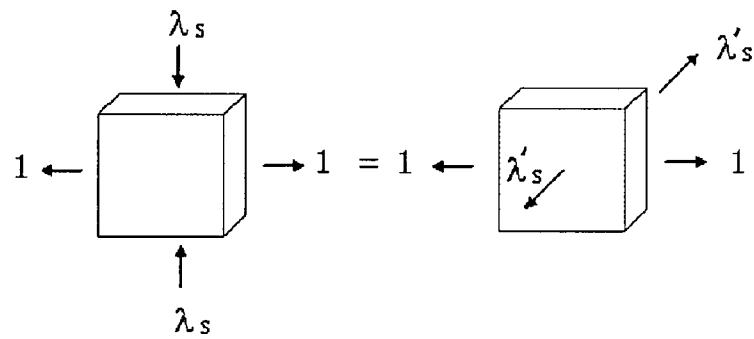
(b) Equibiaxial compression,  $\lambda_U = \frac{1}{\lambda_B^2}$ (c) Planar compression,  $\lambda'_S = \frac{1}{\lambda_S}$ 

Figure 6-4 Equivalent deformation modes

### 6.3.3 Example Application of Strain Partitioning Technique

Take  $(\lambda_1, \lambda_2, \lambda_3) = (4, 0.5, 0.5)$  as an example to show how the strain partitioning technique works. These stretches represent a special case: the three components corresponding to uniaxial tension test. Solving Equations 6-4 – 6-6, the following solutions are obtained:

$$\{ \lambda_U = .1318418017 + .1013282567 * I, \quad \lambda_B = -.8218718290 + .7891731157 * I, \\ \lambda_S = 6.690030027 - .8905013724 * I \},$$

$$\{ \lambda_U = .1318418017 - .1013282567 * I, \quad \lambda_B = -.8218718290 - .7891731157 * I, \\ \lambda_S = 6.690030027 + .8905013724 * I \},$$

$$\{ \lambda_U = 2.160342598, \lambda_B = .8196401365, \lambda_S = 3.020017265 \},$$

$$\{ \lambda_U = 4., \lambda_B = 1., \lambda_S = 1. \}$$

Considering the rules set up for multiple partitioned results, the first two solutions are ignored according to Rule 1 and the third solution is ignored according to Rule 2. Only one valid solution remains, which is  $(\lambda_U, \lambda_B, \lambda_S) = (4, 1, 1)$ . This solution indicates that there is only uniaxial tension in the partitioned result as expected. This simple case demonstrates the capability of the partitioning algorithm.

For stretch tensors, where the three components  $\lambda_1$ ,  $\lambda_2$  and  $\lambda_3$  have simple correlations with each other as in one specific standard test, uniaxial tension for example, the strain partitioning algorithm always give partitioned component stretches as  $\lambda_U > 1$  and  $\lambda_B = \lambda_S = 1$ , which corresponds to the pure uniaxial tension state. Given the pure biaxial or planar tension deformations as an input, the partitioned results will demonstrate the state of biaxial tension or planar tension accordingly.

If the strain partitioning technique is used in a case experiencing strain distribution, the non-uniform strain technique and the strain partitioning technique are combined together: first the local strains are retrieved at each integration point at each time step and then partitioned into varying amounts of the standard deformation.  $C_{10,x}$  and  $C_{01,x}$  in Equation 6-6 are determined by interpolation according to the partitioned strain components. The procedure adopted to calculate material constants according to local strain levels is similar to that described in Section 6.2 for the non-uniform strain technique.

Based on the above analysis, a user subroutine was written for ABAQUS to apply the strain partitioning technique to the standard Mooney-Rivlin constitutive model. The implementation of the strain partitioning technique in a user-subroutine actually incorporates the non-uniform strain technique. The strain partitioning user subroutine is capable of solving the partitioned strain and calculating the total strain energy based on the partitioned results for both uniform and non-uniform deformations.

## **6.4 SUMMARY**

Two techniques, a non-uniform strain technique and a strain partitioning technique, were developed. The non-uniform strain technique is capable of handling strain distribution and the strain partitioning technique is capable of handling multiaxial strain.

With the help of user-subroutine, the Mooney-Rivlin constitutive model can be used together with the two techniques as an input in a mechanical model for an elastomer component deformation analysis. The non-uniform strain user-subroutine provides a constitutive model by applying the standard Mooney-Rivlin strain energy function with the non-uniform strain technique. The strain partitioning user-subroutine provides a constitutive model by applying the standard Mooney-Rivlin strain energy function with both the non-uniform strain and strain partitioning techniques.

Using a modified constitutive model as an input, a mechanical model is expected to demonstrate a more realistic representation for a non-uniform and/or multiaxial deformation case.

## **7 MODEL APPLICATION AND VALIDATION**

Two techniques were developed to predict the elastomeric material behaviour in non-uniform and multiaxial deformations in Chapter 6. Constitutive model was established by applying Mooney-Rivlin strain energy function with these techniques. The application of the proposed constitutive model in a mechanical model of the tapered dogbone sample and cross sample is now discussed. A description of the element meshes, initial and boundary conditions, and the results of the analysis will be presented. To validate these techniques, the calculated deformation and reaction forces are compared with those experimentally measured.

### ***7.1 TENSILE TEST OF A TAPERED DOGBONE SAMPLE***

As previously discussed, the tapered dogbone sample was chosen as the test piece for validation of the non-uniform strain technique. Considering the shape of the tapered dogbone samples, the dominant deformation mode within the loaded sample was assumed to be uniaxial tension with non-uniform magnitudes at different locations. Applying the non-uniform strain technique, the material constants employed in the simulation were altered according to the local strain levels in an effort to make the modified Mooney-Rivlin constitutive model more accurate than the standard one in this non-uniform strain case.

#### ***7.1.1 Mesh***

Applying planes of symmetry across the three orthogonal centerlines (X-Y, Y-Z and X-Z planes), the geometry of the tapered dogbone sample was approximated with the 1/8<sup>th</sup> section shown in Figure 7-1. The geometry was discretized into first-order 8-noded brick elements (the element type is C3D8H in ABAQUS) using ABAQUS/CAE with an element length of 0.5mm. The resulting mesh for the sample contained 624 nodes and 255 elements.

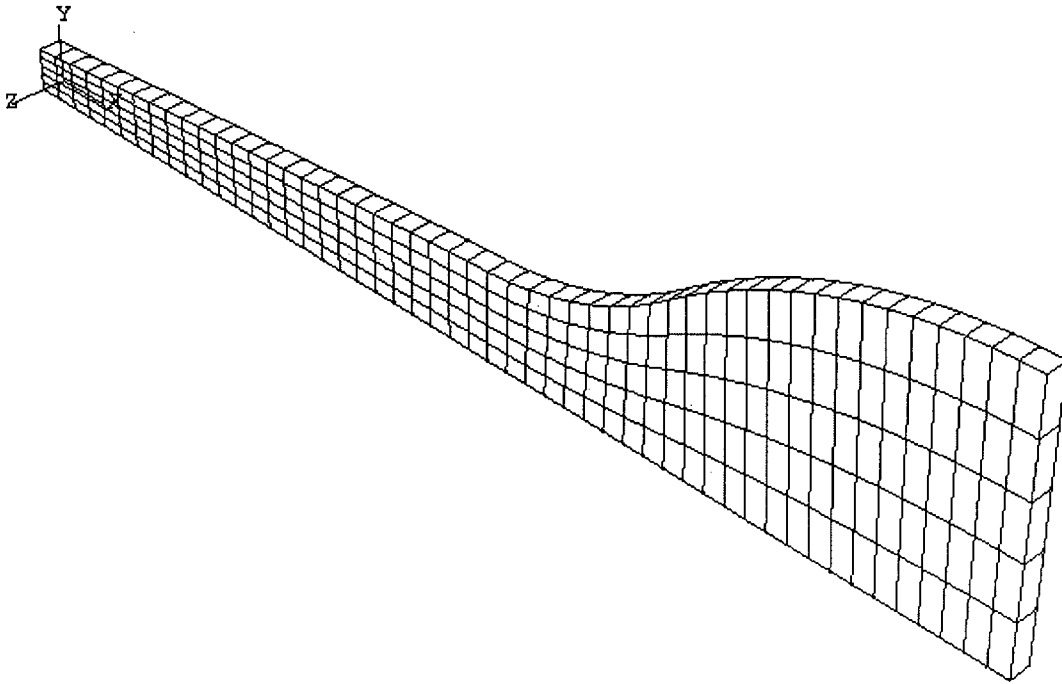


**Figure 7-1 Tapered dogbone sample simplified to a 1/8<sup>th</sup> section and meshed with 8-node brick elements**

### ***7.1.2 Initial and Boundary Conditions***

The tapered dogbone sample was assumed to be strain-free at the beginning of the analysis. Boundary conditions restricting displacement were applied to the nodes on the orthogonal planes bisecting the sample to simulate the symmetry present within the sample.

A single step displacement was applied in ABAQUS to the gripped section of the sample to simulate the applied uniaxial load. On the gripped end, the displacement in the direction normal to the plane ramped to 10mm, corresponding to a 20mm displacement applied across the gauge-length, “stdg” (referring to Figure 5-3).

### ***7.1.3 Predictions and Comparisons to Measured Data***

The modified Mooney-Rivlin constitutive model with the non-uniform strain technique described in Chapter 6 was employed to simulate the uniaxial tension experienced by the tapered dogbone sample tested at UBC. The non-uniform strain technique allowed the

constitutive material behavior to evolve with the maximum strain experienced. In this case, the deformation mode was predominantly uniaxial tension everywhere..

The predicted deformation within the sample employing the non-uniform strain technique is shown in Figure 7-2 as contours of nominal principal strain. As expected, the maximum principal nominal strain varies from 1.009 to  $5.0 \times 10^{-2}$ . The predicted deformed sample shape and a picture taken during the deformation experiments are compared in Figure 7-3. The predicted and measured sample profiles are similar, which gives a qualitative validation of the non-uniform strain technique.

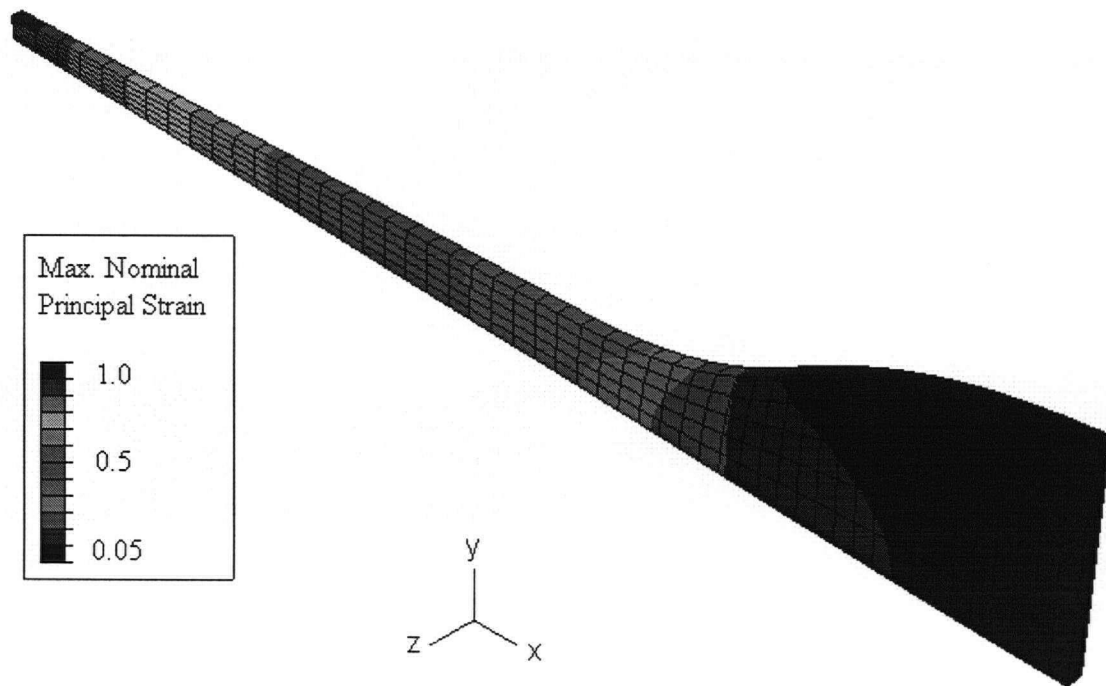


**Figure 7-2 Predicted strain distribution employing the non-uniform strain technique within the deformed tapered dogbone sample**

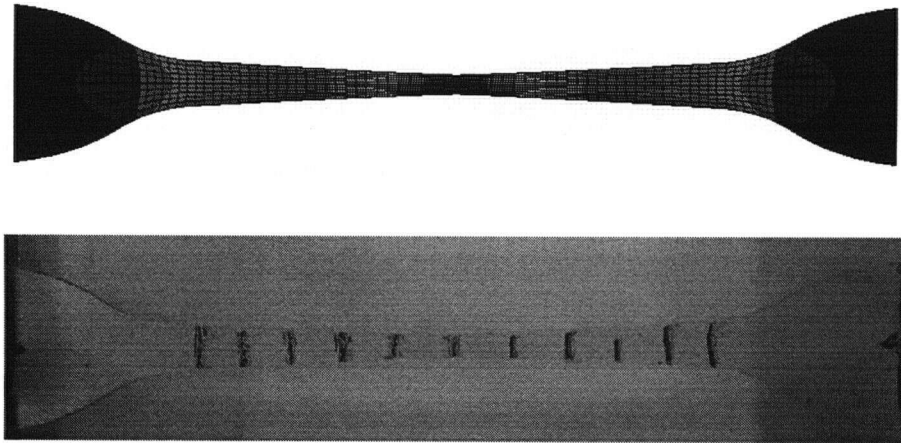


**Figure 7-3 Comparison of the predicted deformed tapered dogbone sample profile and the picture**

As described in Chapter 5, the lengths of different sections were measured during the experiments to give a quantitative representation of the sample deformation (referring to Figure 5-3). The predicted lengths of the same sections were output from ABAQUS and are plotted in Figure 7-4 with the measurements. Figure 7-4 shows that the predictions agree with the measurements. The measured distances increased with the displacement across stdg, but the increasing gradients (corresponding to the slope of each curve) are different.

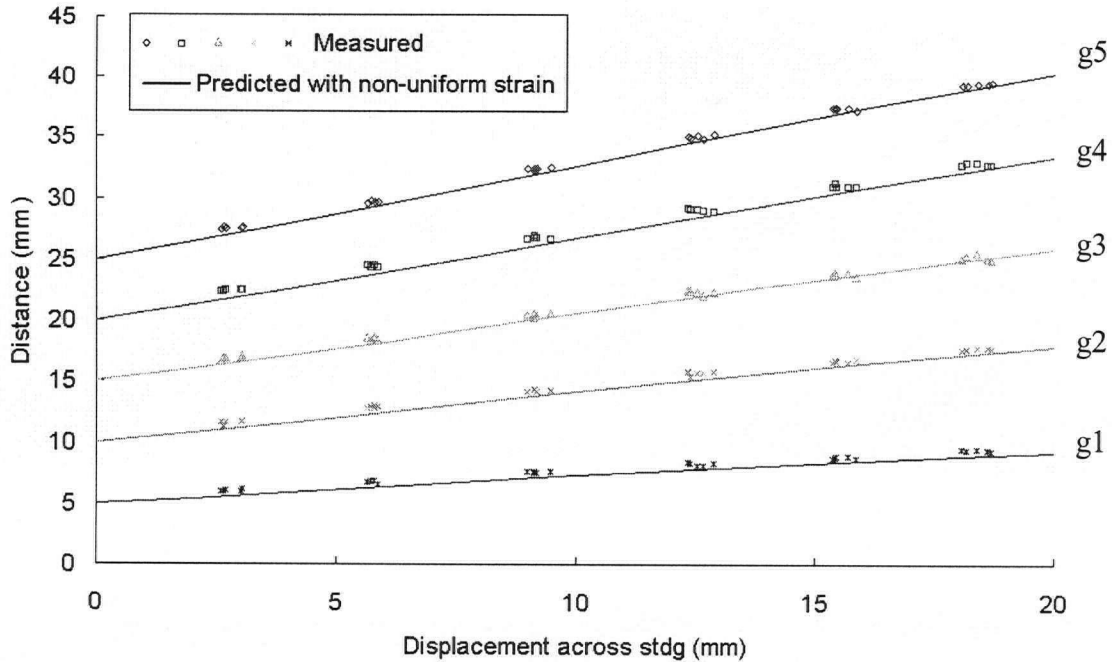


**Figure 7-4 Comparison of the measured deformation and the predicted deformation employing the modified Mooney-Rivlin constitutive model with the non-uniform strain technique for the tapered dogbone sample**

The primary advantage of the modified Mooney-Rivlin constitutive model with the non-uniform strain technique is to avoid having to determine the strain level before performing an analysis. This capability makes this technique more flexible than the standard technique and allows a more accurate representation of cases with non-uniform strain distributions as compared with the standard Mooney-Rivlin constitutive model. As discussed in Section 6.2, the inappropriate use of material constants may result in errors. The predicted strain contour shown in Figure 7-2 demonstrates the variation of local strain ( $1.009$  to  $5.0 \times 10^{-2}$ ). The bounding uniaxial tensile test data is for strain levels of 1.0 and 0.2. Employing the standard Mooney-Rivlin constitutive model with the material constants evaluated at 1.0 and 0.2 strain levels, the predicted deformations are displayed in Figure 7-5. The predictions for these two cases show that employing the standard Mooney-Rivlin constitutive model with the material constants evaluated at 0.2 strain results in larger deviations from the experimental data. The predictions employing the material constants evaluated at 1.0 strain were similar to those made using the non-uniform strain technique.

By employing the standard Mooney-Rivlin constitutive model with the material constants evaluated at 0.2 strain level in the numerical analysis, the model is actually employing material constants evaluated at a lower strain levels to represent material response at a higher strain level. Though applying the material constants evaluated at higher strain levels to lower strain levels will introduce error, generally the error is not as large. The reason for the smaller error is that the material constants evaluated at higher strain levels use a larger range of data in regression analysis. Though the material response at higher strain levels is different from that at lower strain levels, generally speaking, this difference is smaller than that incurred by employing invalidated material constants evaluated at a lower strain level to a high strain level. Comparing the predictions of different constitutive models, the standard Mooney-Rivlin constitutive model with the material constants evaluated at 0.2 strain level gives the poorest result, while the Mooney-Rivlin constitutive model modified with the non-uniform strain technique gives the best result.

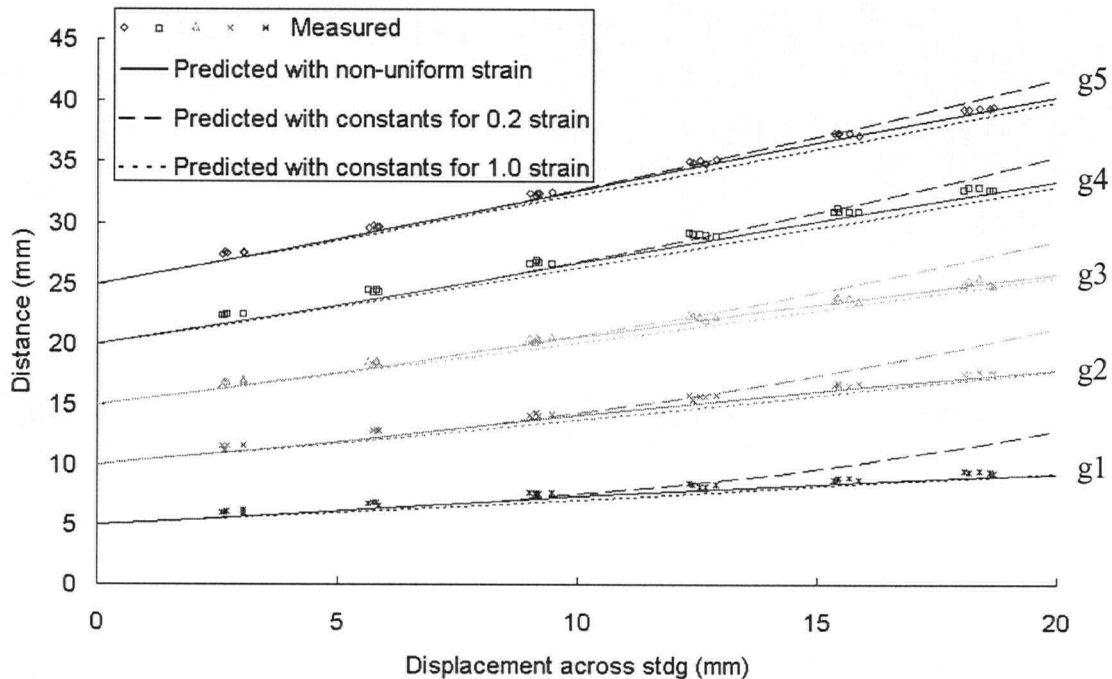


**Figure 7-5 Comparison of the measured deformation and the predicted deformation employing the standard and modified Mooney-Rivlin constitutive models for the tapered dogbone sample**

Employing the non-uniform strain technique, the predicted reaction force at each strain level is plotted in Figure 7-6 with the measured data. The predicted forces agree with the

measured forces, which provides further validation of the capability of the non-uniform strain technique. Predictions employing the standard Mooney-Rivlin constitutive model with the material constants evaluated at 0.2 and 1.0 strains respectively are also plotted in Figure 7-6. Comparing the predictions with different constitutive models, the standard Mooney-Rivlin constitutive model with the material constants evaluated at 0.2 strain level gives the poorest result, while the Mooney-Rivlin constitutive model modified with the non-uniform strain technique gives the best result. The prediction with material constants evaluated at 1.0 strain shows a poorer performance at low strains compared with the prediction employing the non-uniform strain technique, though they give similar results in deformation prediction. The reason for the different prediction qualities is similar to the previous discussion on predicted deformations.

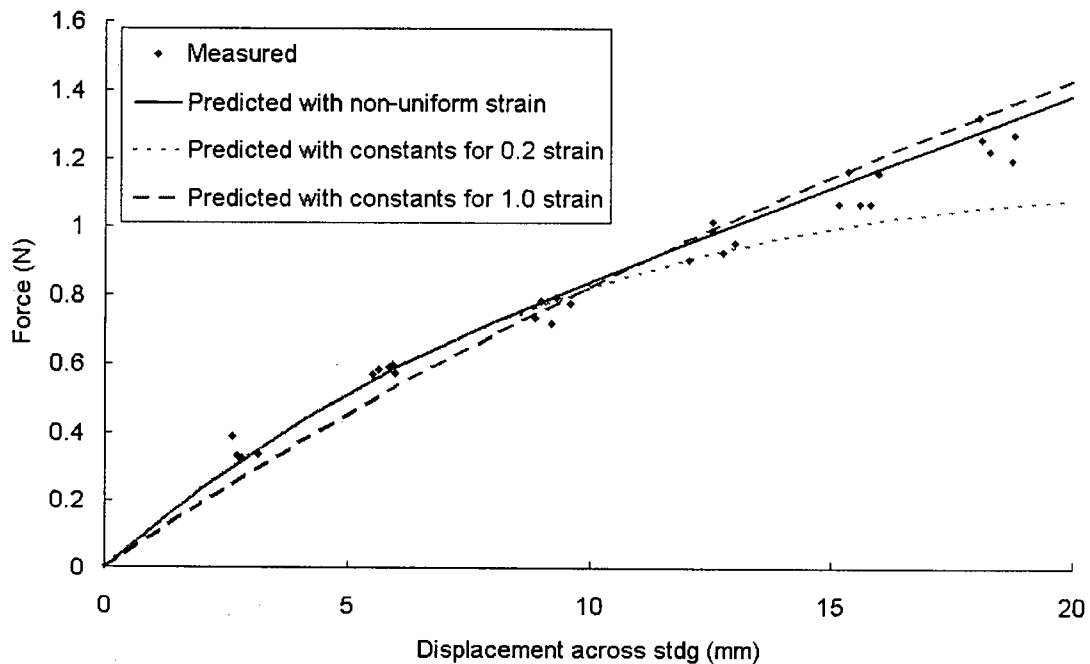


**Figure 7-6 Comparison of the measured reaction force and the predicted reaction force employing the standard and modified Mooney-Rivlin constitutive model for the tapered dogbone sample**

## 7.2 BIAXIAL TEST OF A CROSS SAMPLE

### 7.2.1 Mesh

Applying planes of symmetry (X-Y and Y-Z planes), the geometry of the cross sample was approximated with the 1/4<sup>th</sup> section shown in Figure 7-7. The geometry was discretized into first-order 8-noded brick elements (the element type is C3D8H in ABAQUS) using ABAQUS/CAE with an element length of 1mm. The resulting mesh for the sample contained 1332 nodes and 600 elements.

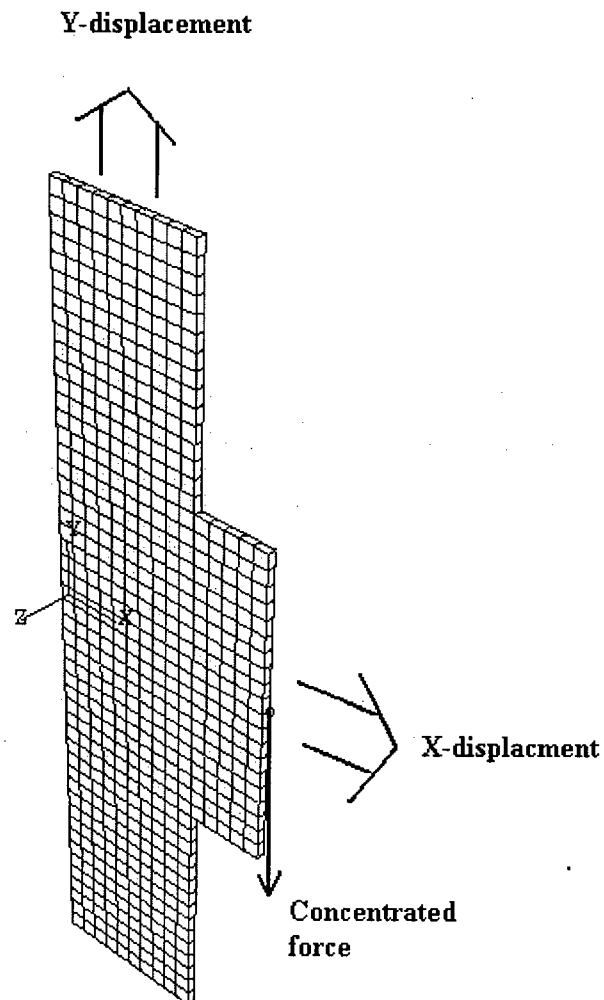


Figure 7-7 Cross sample simplified to a 1/4<sup>th</sup> section and meshed with 8-node brick elements

### **7.2.2 Initial and Boundary Conditions**

The cross sample was assumed to be strain-free at the beginning of the analysis. Boundary conditions restricting displacement were applied to the nodes on the orthogonal planes bisecting the sample to simulate the symmetry present within the sample.

An ABAQUS mechanical model with three loading steps was created to simulate the biaxial loading of the cross sample. During the first step, displacements were applied to the right end (the gripped end along the x-direction) to particular values, i.e. 3mm, 6mm and 9mm, corresponding to the displacements of 6mm, 12mm and 18mm applied to the gauge-length in the x-direction. These displacements simulate the crosswise deformation applied by the crosswise grip. During the second step, the weight of the crosswise grip was applied. The weight of the grip was applied as a negative concentrated force in the y-direction on the center point of the right end. The y-displacements of all nodes on the right end were constrained to be the same in order to simulate the position constraint induced by the crosswise grip. During the first two steps the positions of the top and bottom ends were fixed at their initial location to maintain the initial length in the y-direction. During the third step, a ramped displacement was applied to the top gripped end in the y-direction to 40mm. The displacement in the y-direction of the bottom gripped end was constrained to simulate the conditions in the testing machine.

### **7.2.3 Predictions and Comparisons to Measured Data**

The modified Mooney-Rivlin constitutive model using the strain partitioning technique described in Chapter 6 was employed to simulate the biaxial tension experienced by the cross samples tested at UBC. The strain distribution within the deformed sample and predicted reaction forces will be presented and compared with the measured data.

For the cross sample, different displacements were applied along the crosswise direction (the x-direction as shown in Figure 7-7). Only the predictions for a 6mm x-displacement are discussed in this section as the predictions for 12mm and 18mm x-displacements showed similar results.

Employing the strain partitioning technique, the predicted maximum nominal principal strain contours are plotted on the deformed mesh in Figure 7-8. As shown in Figure 7-8, not only are the magnitudes of deformation different at different locations, but the deformation modes are also different as the elements within the sample were deformed to different shapes. The final deformed mesh showing the deformed sample profile is compared to a picture taken during the experiments in Figure 7-9. The predicted and measured sample profiles match each other giving a qualitative validation of the strain partitioning technique.

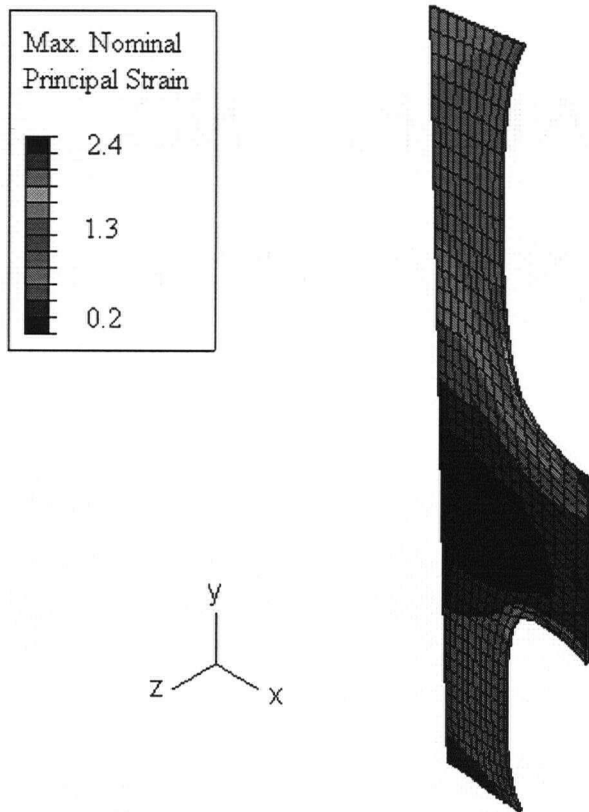


**Figure 7-8 Predicted strain distribution within the deformed cross sample employing the strain partitioning technique (x-displacement=6mm, y-displacement=30mm)**

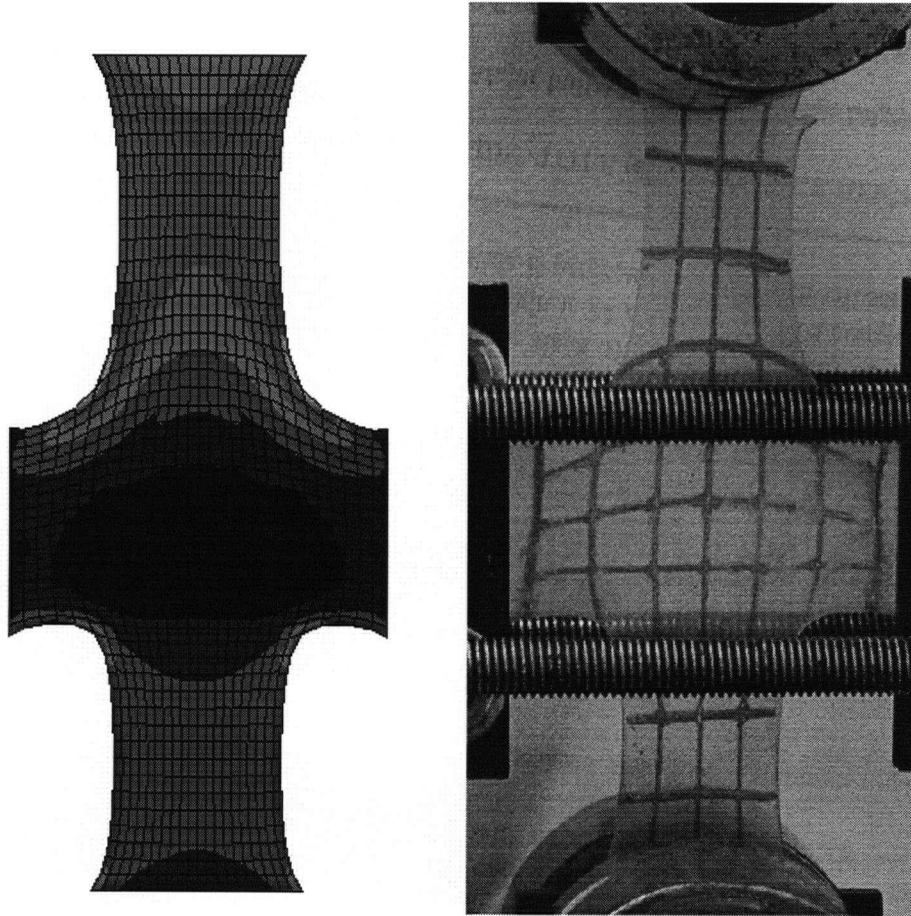


**Figure 7-9 Comparison of the predicted deformed cross sample profile and the picture (x-displacement=6mm, y-displacement=30mm)**

As described in Chapter 5, the lengths of the different sections along the y-direction were measured during the experiments to give a quantitative representation of the sample deformation (referring to Figure 5-11). The predicted lengths for a 6mm x-displacement are plotted in Figure 7-10 with the measured lengths. Figure 7-10 shows that the predicted data agree with the measured data.

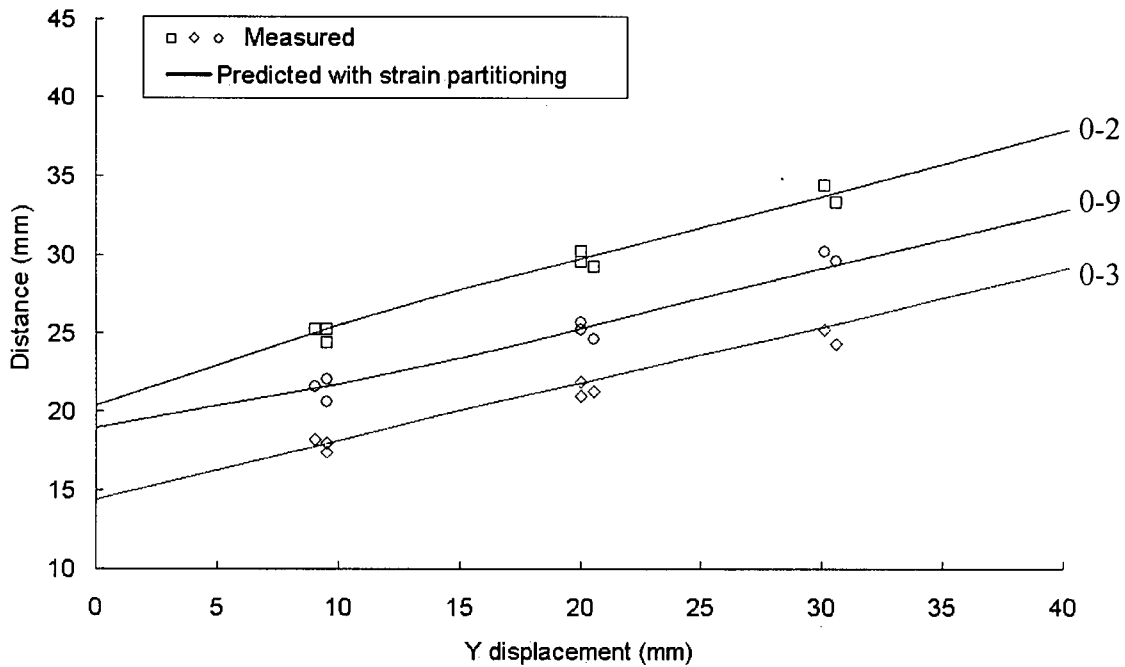


**Figure 7-10 Comparison of the measured deformation and the predicted deformation employing the modified Mooney-Rivlin constitutive model with the strain partitioning technique for the cross sample**

By determining the deformation mode locally, the strain partitioning technique provides a solution capable of describing multiaxial strain within a deformed sample. The implementation of the strain partitioning technique actually incorporates the non-uniform strain technique, so the strain partitioning technique characterizes not only the different deformation modes, but also the different strain magnitudes at each location. Compared with the non-uniform strain technique, the strain partitioning technique is more advanced in solving non-uniform and multiaxial problems. Employing the non-uniform strain technique without considering the deformation mode may result in error.

Incorrectly employing the non-uniform Mooney-Rivlin material constants in the prediction of the cross sample is demonstrated in Figure 7-11. Based on the experimental setup of the cross sample, it could be assumed that the deformation within the cross sample would be similar to equibiaxial tension. However, the predicted deformation response with the non-uniform equibiaxial material constants shows a large deviation from the experimental data as shown in Figure 7-11. The prediction with the strain

partitioning technique gives a better representation of the experimental data. For a sample with complex geometry or in complex deformation, it is difficult to predict the deformation mode before an analysis. Actually, the predominant deformation mode within the deformed cross sample is uniaxial tension in the y-gauge-length area. More discussions will be presented in the next section.

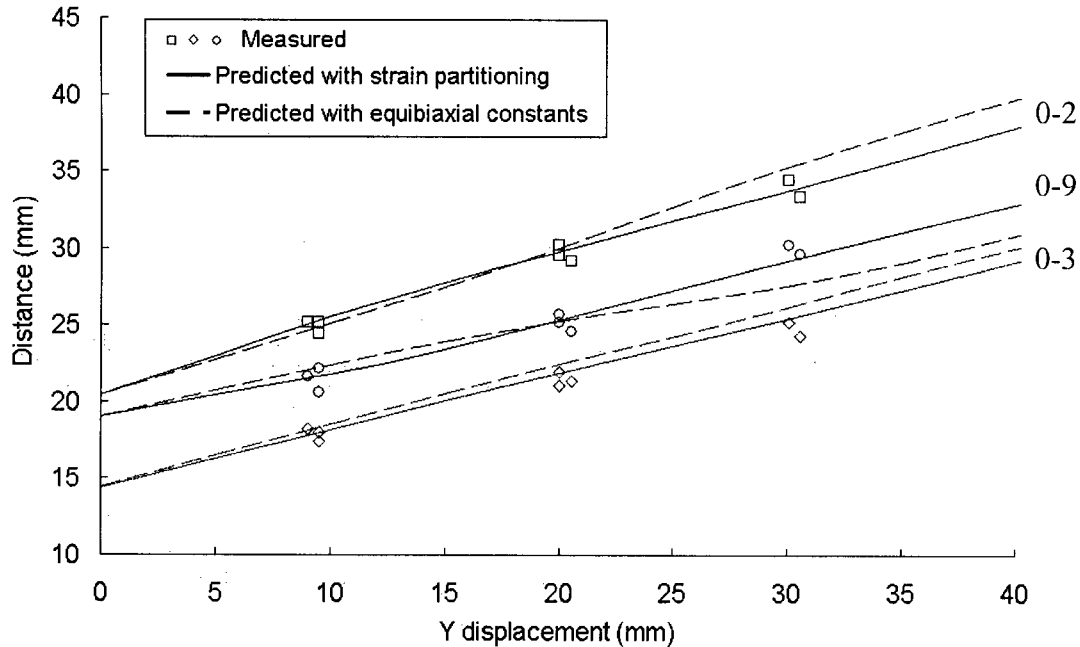


**Figure 7-11 Comparison of the measured deformation and the predicted deformation employing the different modified Mooney-Rivlin constitutive models for the cross sample**

Employing the strain partitioning technique, the predicted reaction forces are plotted in Figure 7-12 with the measured data. It should be noted that at the zero y-displacement, the reaction force is not zero for two important reasons. First, the weight of the grip results in a reaction force in the y-direction. Second, applying a displacement in the crosswise direction (the x-direction) results in a contraction in the loading direction (the y-direction). The contraction in the y-direction contributes to the initial load as the positions of the top and bottom grips were fixed. As displayed in Figure 7-12, the predicted forces agree with the measured forces at all three strain levels, which validates the accuracy of the strain partitioning technique. The predictions employing the strain partitioning technique are also compared with the predictions employing the non-uniform equibiaxial constants in Figure 7-12. The non-uniform equibiaxial predictions deviate

from the experimental data. By characterizing the non-idealized multiaxial deformation mode as well as the non-uniform strain distribution, the predictions with the strain partitioning technique give a better representation of the experimental data. Employing the modified Mooney-Rivlin constitutive model with the strain partitioning technique, the need to pre-determine the strain level and deformation mode before an analysis is run can be avoided. This provides the potential for a more accurate and realistic prediction of a complex component deformation under operational loading conditions.

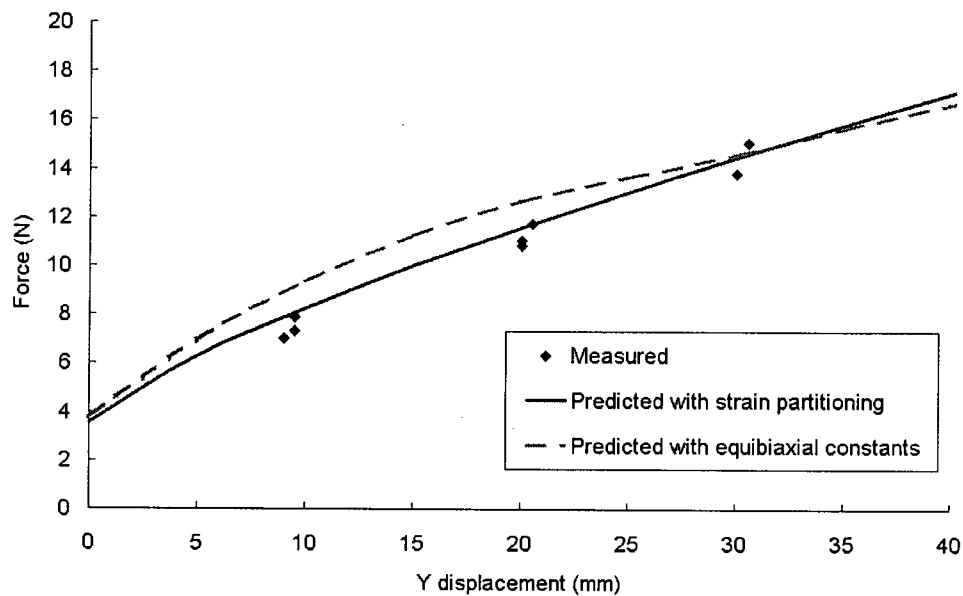


**Figure 7-12 Comparison of the measured reaction force and the predicted reaction force employing the different modified Mooney-Rivlin constitutive models for the cross sample**

## 7.2.4 Discussion of Cross Sample Results

### 7.2.4.1 Effect of Crosswise Displacement

Applying different displacements in the crosswise direction (the x-direction) resulted in different contractions in the loading direction (the y-direction). As the gripped ends in the y-direction were held, displacements in the x-direction introduced initial loads in the y-direction. As larger displacements were applied in the crosswise direction, higher initial reaction forces were experienced in the loading direction. Figure 7-13 displays the measured and predicted reaction forces for different x-displacements. The predicted reaction forces show the effect of the crosswise displacement, i.e. at the same y-

displacement, the predicted reaction force for an 18mm x-displacement is the highest.

The difference between the measured reaction forces for the different x-displacements is more difficult to discern considering the scattered data distribution. Four possible reasons for the scatter in the measured data are:

- (1) Scatter is partially caused by the slipping of the sample in the grip. As the amount of the slippage was difficult to characterize, it was difficult to ensure the same y-displacement in each loading case.
  - (2) The actual y-displacement of each section was measured with a caliper as described in Chapter 5. The reference lines were drawn on the cross samples by hand, which may introduce error.
  - (3) Samples began to failure near the grips during the testing as described in Chapter 5. The progressive failure of the samples affected the measured force.
  - (4) The ratio of measured force to maximum rated load of the load cell was low. Thus, the resolution in the force data may not be sufficient to show subtle differences. Additionally, at these low loads machine noise from the hydraulic systems affects the measured forces.
- Considering these issues, the overall comparison between the predicted and measured data is reasonable.

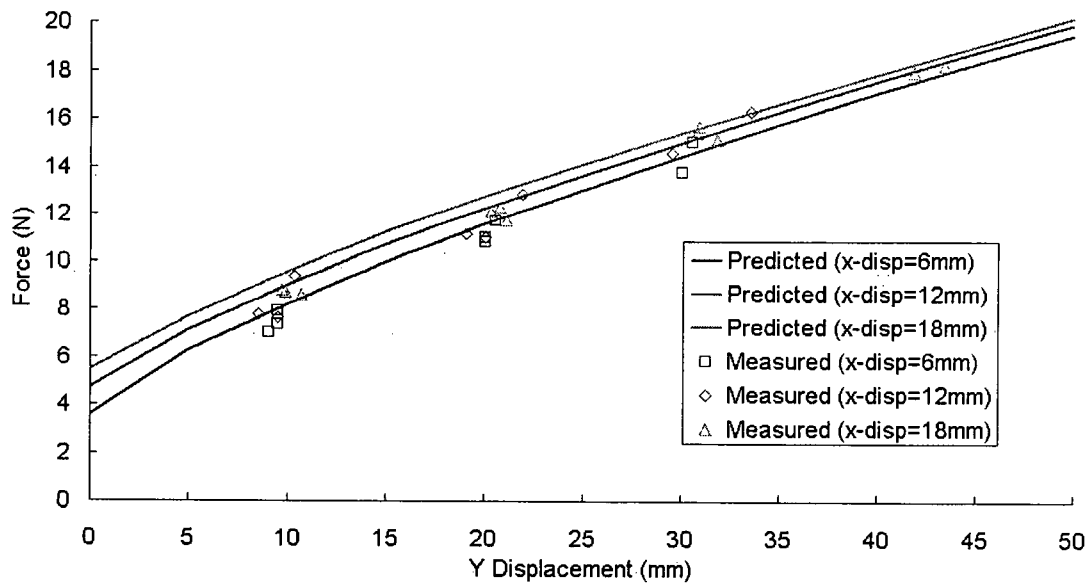


**Figure 7-13 Comparison of the measured reaction forces and the predicted reaction forces employing the strain partitioning technique for different x-displacements for the cross sample**

#### 7.2.4.2 Effect of Crosswise Grip

The biaxial tension tests were designed to produce a non-standard deformation. There were two features necessary to accomplish this goal: first, the gauge-length in each direction was designed to be the same; second, the applied loads in the two perpendicular directions were varied to simulate a wide variety of deformation modes. The gauge-lengths in the different directions affect the deformation mode. For example, if the gauge-length in the primary loading direction (y-direction) is much longer than that in the crosswise direction (x-direction), the crosswise load will have limited impact on the reaction force in the loading direction. In this case, the predominant deformation mode in the gauge-length area in the y-direction will be uniaxial tension. Thus, the gauge-lengths in the loading direction and the crosswise direction were designed to be identical to eliminate this shape effect.

The magnitude of load also affects the predominant deformation mode. If the load in the y-direction is much higher than that in the crosswise direction, the predominant deformation mode in the gauge-length area in the y-direction will be uniaxial tension. The desired cross sample has the geometry shown in Figure 7-14. The shaded areas were proposed for gripping the sample. Assuming the desired sample is deformed in a testing machine designed for biaxial loading (i.e. the custom crosswise grip used in this study is not needed to apply the crosswise load), the reaction forces for this loading condition, shown in Figure 7-15, have been predicted using the different constitutive models. As demonstrated in Figure 7-15, when the x-displacement (6mm) and the y-displacement are similar ( $y\text{-displacement} \leq 20\text{mm}$ ), the predictions using the strain partitioning technique are different from the predictions employing the non-uniform strain technique with material constants evaluated for the standard deformation modes. This difference indicates that there is no dominant deformation mode within the sample although it is near to uniaxial. In contrast, if the y-displacement is much larger than the x-displacement, the dominant deformation mode in the gauge-length area in the y-direction becomes uniaxial tension. This shift is reflected in the predicted reaction forces where the strain partitioning technique result is very close to that predicted with uniaxial constants when the y-displacement exceeds 20mm.

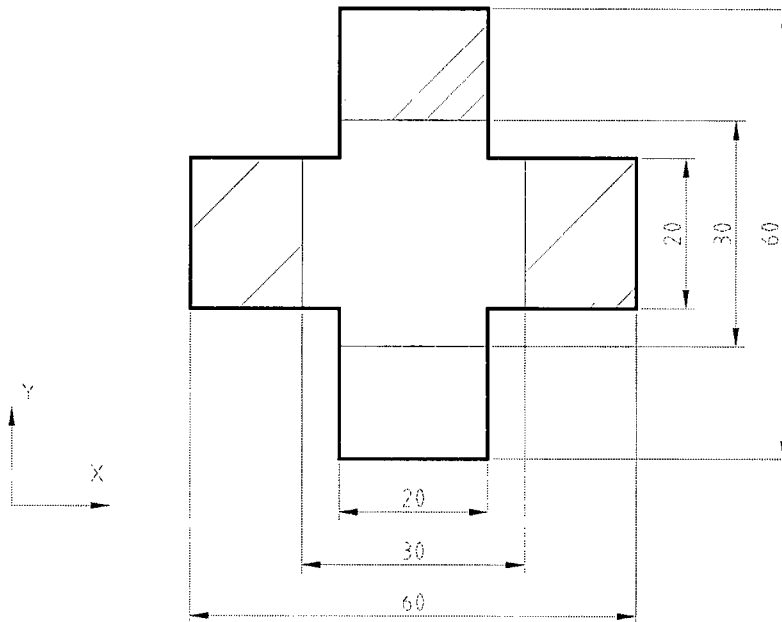


Figure 7-14 Geometry of the desired cross sample

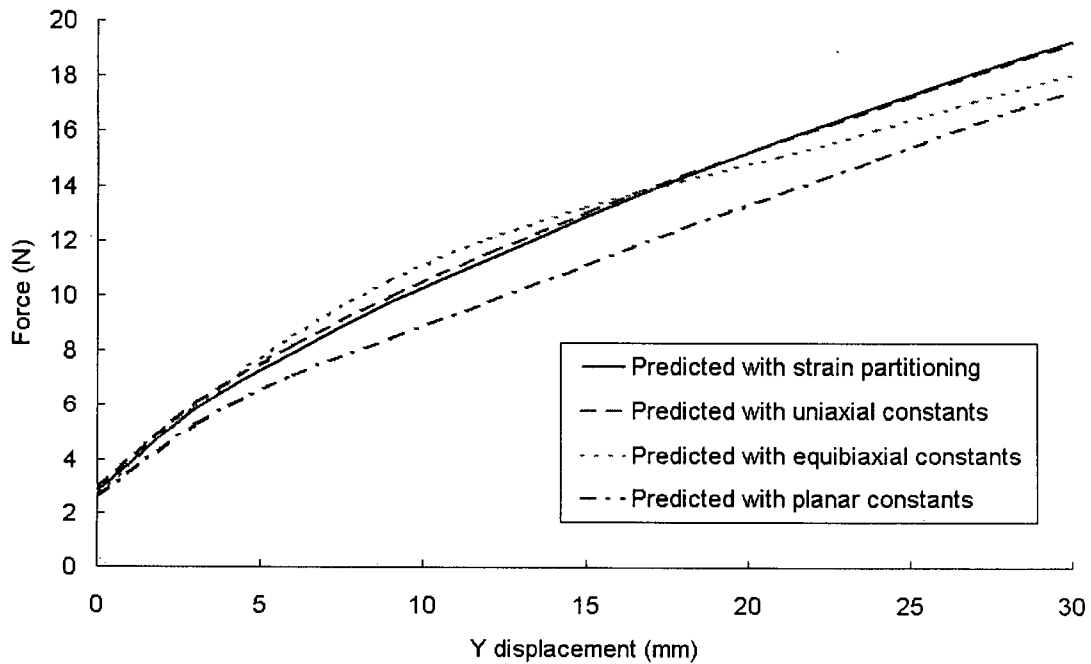
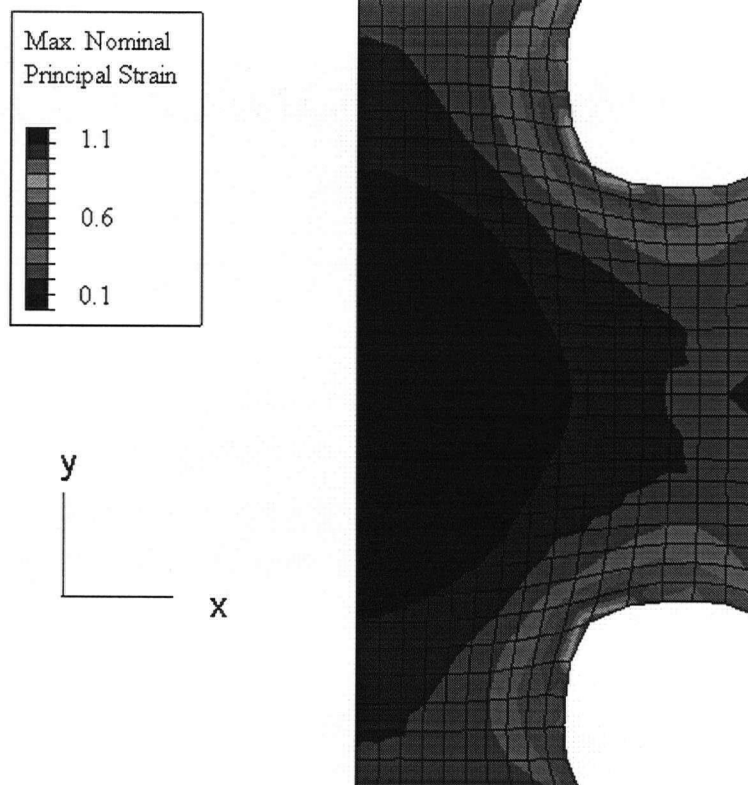


Figure 7-15 Comparison of the predicted reaction forces employing the modified Mooney-Rivlin constitutive models with the non-uniform strain and the strain partitioning techniques individually for the cross sample ( $x$ -displacement=6mm)

It should be noted that even when the x-displacement is equal to the y-displacement (6mm), the deformation mode within the sample is not equibiaxial tension as demonstrated in Figure 7-16. As shown in Figure 7-16, approximately the mesh within the square center area deforms equibiaxially while deformation of the mesh near the constrained gripped ends and within the boundary area of the center and the tab is complicated and can not be represented by one of the standard types. For a complex geometry like the cross sample, the deformation mode is difficult to predict even if the loading condition is simple.



**Figure 7-16 Predicted strain distribution within the deformed desirable cross sample (x-displacement=6mm, y-displacement=6mm)**

In the absence of an appropriate testing facility to load samples in two perpendicular directions, the biaxial tension tests for this investigation were accomplished with the purpose-built crosswise grip. Unfortunately, the deformation conditions deviated from the desired biaxial test. First, no support was available to balance the weight of the grip. Second, the bolts in the grip assembly blocked access to the cross sample, which reduced

the available area to grip the sample in the loading direction. With a smaller grip area, a higher clamping force had to be applied to prevent the sample from slipping. The increased clamp force was responsible for sample failure (referring to Chapter 5).

The grip weight was considered as a load. The addition of the grip weight could be considered advantageous since it acts to complicate the loading condition. However, under this complex loading condition, it is difficult to predict the deformation mode within the cross sample, further supporting the need for the use of a strain partitioning technique.

The comparison of the measured and predicted reaction forces for the real cross sample is shown in Figure 7-17. Figure 7-17 demonstrates the prediction with the strain partitioning technique is almost identical to the prediction with non-uniform uniaxial constants, i.e. uniaxial tension mode is predominant within the y-gauge-length area as the crosswise grip affects the deformation mode.

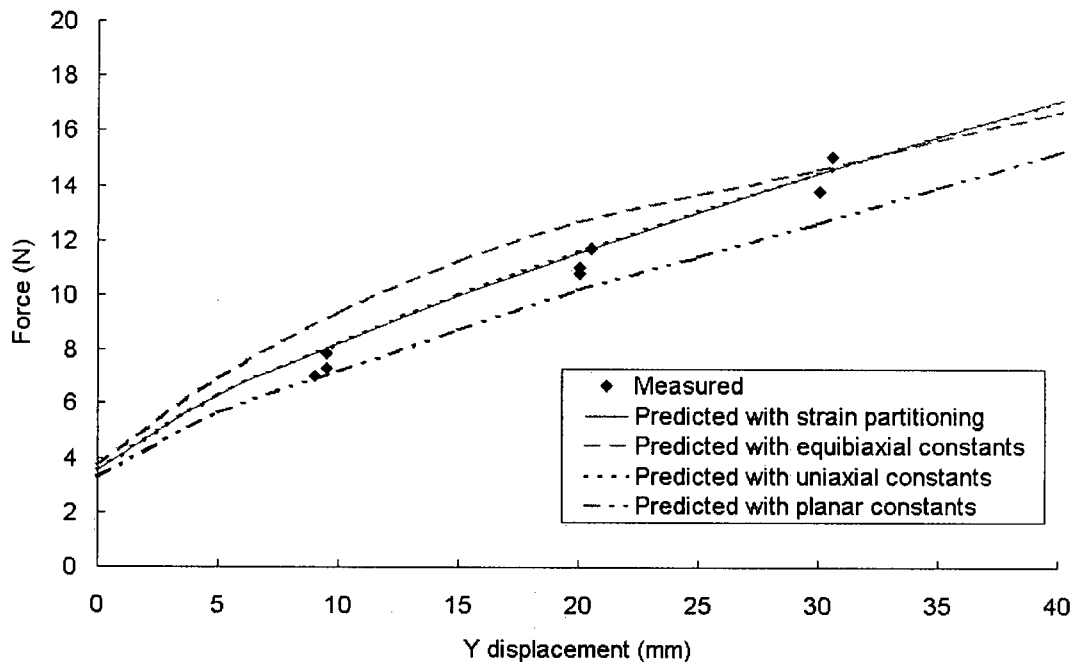


**Figure 7-17 Comparison of the predicted reaction forces employing the modified Mooney-Rivlin constitutive models with the non-uniform strain and the strain partitioning techniques individually for the cross sample (x-displacement=6mm)**

### **7.3 SUMMARY**

The two techniques formulated in Chapter 6 were used to predict the evolution of displacements and reaction forces in the tapered dogbone and cross samples. Prior to presenting the results, the geometry, initial and boundary conditions employed for each case were summarized.

The tapered dog-bone sample was used to validate the non-uniform strain technique. The deformation mode within the deformed sample was predominantly uniaxial tension with non-uniform strain magnitudes at different locations. The modified Mooney-Rivlin constitutive model with the non-uniform strain technique characterizes the non-uniform strain distribution by taking the local strain level as a parameter to select the material constants. Employing the non-uniform strain technique, the predicted displacements and forces agreed with the measured data, which validates the accuracy and applicability of this technique.

The cross sample was used to produce non-uniform strain and multiaxial deformation conditions in one sample. The strain partitioning technique was used to predict this behaviour. The modified Mooney-Rivlin constitutive model with the strain partitioning technique characterizes the non-uniform and multiaxial strain distribution by retrieving the local strains, partitioning the multiaxial strains into varying amount of the three standard types and selecting the material constants according to the partitioned results. Employing the strain partitioning technique, the predicted displacements and forces agreed with the measured data, which validates the accuracy and applicability of the strain partitioning technique.

## **8 SUMMARY AND CONCLUSIONS**

This research project has focused on developing mathematical constitutive models capable of predicting the stable mechanical response of elastomeric materials in non-uniform and/or multiaxial deformation at low or medium strain (<100%). When these models are incorporated in a mechanical model as an input, they improve its accuracy and adaptability in non-uniform and/or multiaxial deformations. These constitutive models will aid in understanding the stable response of elastomeric materials used for seals in fuel cells by developing an improved understanding of the deformation response to help in predicting seal integrity and improve the overall reliability of PEM fuel cell systems.

In order to generate the data necessary for constitutive model characterization, a series of tests were performed on a candidate seal material, silicone elastomer. Experimental data of a complete series of characterization tests, including uniaxial tension, equibiaxial tension, and planar tension, was provided by Ballard Power Systems Inc. for the silicone elastomer. The experimental data showed that the material response changes with maximum strain and deformation mode. The experimental data was used to fit the standard Mooney-Rivlin strain energy function for each deformation mode and strain level tested. For each individual strain level and deformation mode, the resulting material constants are unique.

Additional uniaxial tension tests were conducted for a different batch of silicone at UBC. The uniaxial response of the material from the two different lots behaved differently. A similar difference in behaviour was expected for equibiaxial and planar tension tests. Unfortunately, without appropriate facilities, equibiaxial tension and planar tension could not be performed at UBC. The material behaviours in equibiaxial and planar tensions for the new silicone were estimated by scaling the data of the old silicone with appropriate factors based on the variation of the uniaxial responses.

The constitutive material behaviour, which is a part of the input of the mechanical model, is defined in terms of a strain energy function. Constitutive models incorporating the

maximum strain experienced and deformation mode were derived by modifying the standard Mooney-Rivlin strain energy function with two techniques, a non-uniform strain and a strain partitioning technique. In the non-uniform strain technique, the local strain energy is determined according to the local maximum strain level experienced during an analysis. This alleviates the need of determining the maximum strain before an analysis in order to select the appropriate set of material constants. Compared to the predictions using the standard Mooney-Rivlin strain energy function, the predictions using the non-uniform strain technique were expected to give better results for a component experiencing non-uniform strain conditions. In the strain partitioning technique, the strain energy for multiaxial deformation conditions is determined by partitioning the arbitrary multiaxial strain into varying amounts of three standard deformations. This eliminates the need of determining the deformation mode before an analysis. Together, these techniques were expected to provide more realistic deformation predictions for elastomeric materials experiencing non-uniform and multiaxial deformation.

Two mechanical tests were designed to provide the data necessary to validate the non-uniform strain and strain partitioning techniques. The first test, a tapered dogbone sample, exhibited varying amounts of uniaxial tensile deformation within the gauge-length area when stretched. Model predictions using the non-uniform strain technique showed improved results over predictions using the standard Mooney-Rivlin strain energy function for this sample. The second test, on a cross sample, included loading in two perpendicular directions with different amounts of displacements. These deformation conditions resulted in a complicated strain state in the sample: both strain level and deformation mode changed with locations. Model predictions using the strain partitioning technique showed more accurate results in this sample compared with predictions using the standard Mooney-Rivlin strain energy function. Without robust facilities to perform biaxial loading, the cross sample test was run in a testing machine with uniaxial loading capability and a crosswise grip was used to provide an additional load in the crosswise direction. The purpose-built crosswise grip affected the sample deformation mode and resulted in a predominantly uniaxial deformation mode. However, this unanticipated complication in the loading condition supports the need for the strain partitioning

technique as it clearly shows that the deformation mode need not be determined prior to an analysis.

In the two tests, mechanical model predictions using the proposed constitutive models fit the experimental results. Compared with the predictions using the standard Mooney-Rivlin strain energy function, the predictions using the modified Mooney-Rivlin strain energy functions provide more accurate results for elastomeric materials experiencing non-uniform and multiaxial deformation. These constitutive models will aid in understanding the stable response of seal materials used in the Ballard fuel cells.

### ***8.1 RECOMMENDATIONS FOR FUTURE WORK***

The material constants of the new silicone for equibiaxial and planar tensions, tested in uniaxial tension at UBC, were estimated from the material constants of the silicone tested by Ballard. Equibiaxial and planar characterization tests should be conducted to validate this estimation. Further more, tests for samples with complex geometries should be performed in order to provide further validation of the accuracy and adaptability of the strain partitioning technique. Failure tests are also desirable for providing information for seal failure analysis.

The modified strain energy function developed during this investigation only considers the maximum strain level experienced and deformation mode. To complete the description of equilibrium behaviour, it is important to consider the effect of temperature. In order to use the current mechanical model, material characterization tests have to be conducted at the same temperature as experienced by the real component. If the operational temperature changes, characterisation tests must be redone. A constitutive model incorporating temperature as a parameter will help to reduce the characterization tests needed and provide a more accurate prediction for components experiencing temperature gradient.

In order to develop a mechanical model with the capability to predict material response under arbitrary loading condition, time has to be incorporated as a parameter. The stress-

strain behavior of elastomeric materials is strongly dependent on time. The time dependence results in numerous experimentally observed phenomenon including rate-dependence, stress relaxation, and hysteresis during cyclic loading. Few constitutive models are time-dependent and they all have complex forms. It is desirable to establish a time-dependent constitutive model with a simple form, so it can be incorporated into commercial finite element analysis software. A time-dependent constitutive model will greatly extend the range of model adaptability.

## **REFERENCES**

1. L.R.G. Treloar: *The Physics of Rubber Elasticity*, 3rd ed., Clarendon Press, Oxford, 1975.
2. A. Ciesielski: *An Introduction to Rubber Technology*, Rapra Technology Limited, Shrewsbury, UK, 1999.
3. "<http://www.eng.ku.ac.th/~mat/MatDB/MatDB/source/Struc/polymers/synrub/synrub.htm>", Jan 1st, 2005.
4. M. Mikkola, in [www.hut.fi/Units/AES/studies/specials/mikkola1.pdf](http://www.hut.fi/Units/AES/studies/specials/mikkola1.pdf) eds. (2000).
5. "General Graphics and Information", *Ballard Power Systemes Inc.*
6. "[http://www.fueleconomy.gov/feg/fcv\\_PEM.shtml](http://www.fueleconomy.gov/feg/fcv_PEM.shtml)", Jan 1st, 2005.
7. *ABAQUS/Standard User's Manual*, Hibbitt, Karlsson & Sorensen, Inc, Pawtucket, USA.
8. K. Miller: "Testing Elastomers for Hyperelastic Material Models in Finite Element Analysis", *Axel Products Inc. Documents*, <http://www.axelproducts.com/pages/Downloads.html>, 2000.
9. L. Mullins: "Softening of Rubber by Deformation", *Rubber Chemistry and Technology*, 1969, vol. **42**, pp. 339-62.
10. L. Mullins and N.R. Tobin: "Theoretical model for the elastic behavior of 8lller-reinforced vulcanized rubbers", *Rubber Chemistry and Technology*, 1947, vol. **30**, pp. 551-71.
11. M.A. Johnson and M.F. Beatty: "The Mullins effect in uniaxial extension and its influence on transverse vibration of rubber string", *Continuum Mechanics and Thermodynamics*, 1993, vol. **5**, pp. 83-115.
12. K. Miller: "Experimental Loading Conditions Used to Implement Hyperelastic and Plastic Material Models", *Axel Products Inc. Documents*, <http://www.axelproducts.com/pages/Downloads.html>.
13. J.D. Ferry: *Viscoelastic Properties of Polymers*, 2nd ed., John Wiley & Sons, Inc., 1970.
14. J.S. Bergstrom and M.C. Boyce: "Constitutive Modelling of the Time-dependent and Cyclic Loading of Elastomers and Application to Soft Biological Tissues", *Mechanics of Materials*, 2001, vol. **33**, pp. 523-30.
15. J.A. Popio: PhD thesis, Energetically Based Phenomenological Constitutive Model for Rubber(PhD thesis), University of Akron (August, 2000).
16. J.S. Bergström and M.C. Boyce: "Constitutive Modeling of the Large Strain Time-dependent Behavior of Elastomers ", *Journal of the Mechanics and Physics of Solids*, 1998, vol. **46**, pp. 931-54.
17. M.C. Boyce and E.M. Arruda: "Constitutive Model of Rubber Elasticity: A Review", *Rubber Chemistry and Technology*, 2000, vol. **73**, pp. 504-23.
18. M.C. Wang and E. Guth: "Statistical Theory of Networks of Non-Gaussian Flexible Chains", *The Journal of Chemical Physics*, 1952, vol. **20**, pp. 1057-184.
19. P.J. Flory and J. John Rehner: "Statistical Mechanics of Cross-Linked Polymer Networks I. Rubberlike Elasticity", *The Journal of Chemical Physics*, 1943, vol. **11**, pp. 512-20.
20. E.M. Arruda and M.C. Boyce: "A three-dimensional constitutive model for the

- large stretch behavior of rubber elastic materials", *Journal of the Mechanics and Physics of Solids*, 1993, vol. **41**, pp. 389-412.
21. A.N. Gent: "A New Constitutive Relation for Rubber", *Rubber Chemistry and Technology*, 1996, vol. **69**, pp. 59-62.
  22. J. Lambert-Diani and C. Rey: "New phenomenological behavior laws for rubbers and thermoplastic elastomers", *European Journal of Mechanics - A/Solids*, 2003, vol. **18**, pp. 1027-43.
  23. M. Mooney: "A Theory of Large Elastic Deformation", *Journal of Applied Physics*, 1940, vol. **11**, pp. 567-624.
  24. R.W. Ogden: "Large Deformation Isotropic Elasticity - On the Correlation of Theory and Experiment for Incompressible Rubberlike Solids", *Proceedings of the Royal Society of London. Series A, Mathematical and Physical Sciences*, 1972, vol. **326**, pp. 565-84.
  25. K.C. Valanis and R.F. Landel: "The Strain-Energy Function of a Hyperelastic Material in Terms of the Extension Ratios", *Journal of Applied Physics*, 1967, vol. **38**, pp. 2997-3002.
  26. O.H. Yeoh: "Some Forms of the Strain Energy Function for Rubber", *Rubber Chemistry and Technology*, 1993, vol. **66**, pp. 754-72.
  27. R.S. Rivlin: "Large Elastic Deformations of Isotropic Materials. IV. Further Developments of the General Theory", *Philosophical Transactions of the Royal Society of London. Series A, Mathematical and Physical Sciences*, 1948, vol. **241**, pp. 379-97.
  28. *ABAQUS Theory Manual*, Hibbitt, Karlsson & Sorensen, Inc, Pawtucket, USA.
  29. G. Marckmann, E. Verron, L. Gornet, G. Chagnon, P. Charrier and P. Fort: "A theory of network alteration for the Mullins effect", *Journal of the Mechanics and Physics of Solids*, 2002, vol. **50**, pp. 2011 – 28.
  30. C. Miehe: "Discontinuous and continuous damage evolution in Ogden-type large-strain elastic materials", *European Journal Of Mechanics - A/solids*, 1995, vol. **14**, pp. 697-720.
  31. R.W. Ogden and D.G. Roxburgh: "A Pseudo-Elastic Model for the Mullins Effect in Filled Rubber", *Proceedings of the Royal Society of London. Series A*, 1999, vol. **455**, pp. 2861-77.
  32. J.S. Bergström and M.C. Boyce: "Large Strain Time-dependent Behavior of Filled Elastomers", *Mechanics of Materials*, 2000, vol. **32**, pp. 627-44.
  33. J.S. Bergström and M.C. Boyce: "Constitutive Modelling of the Time-dependent and Cyclic Loading of Elastomers and Application to Soft Biological Tissues", *Mechanics of Materials*, 2001, vol. **33**, pp. 523-30.
  34. W.-F. Chen and A.F. Saleeb: *Constitutive Equations for Engineering Material*, 2nd ed., Elsevier, Amsterdam, The Netherlands, 1994.
  35. H. Menderes and A.W.A. Konter: Proceedings of the First European Conference on Constitutive Models for Rubber, Dorfmann and Muhr, eds., Vienna, 1999.
  36. L. Mullins: "Softening of Rubber by Deformation", *Rubber Chemistry and Technology*, 1969, vol. **42**, pp. 339 - 62.
  37. *Nonlinear Finite Element Analysis of Elastomers*, MARC Analysis Research Corporation, 1996.
  38. G.P. Nikishkov: *Introduction to the Finite Element Method (Lecture Notes)*,

- University of Aizu, 2004.
39. O.C. Zienkiewicz and R.L. Taylor: *The Finite Element Method*, 4th ed., McGraw-Hill Book Co., 1994.

**APPENDIX**

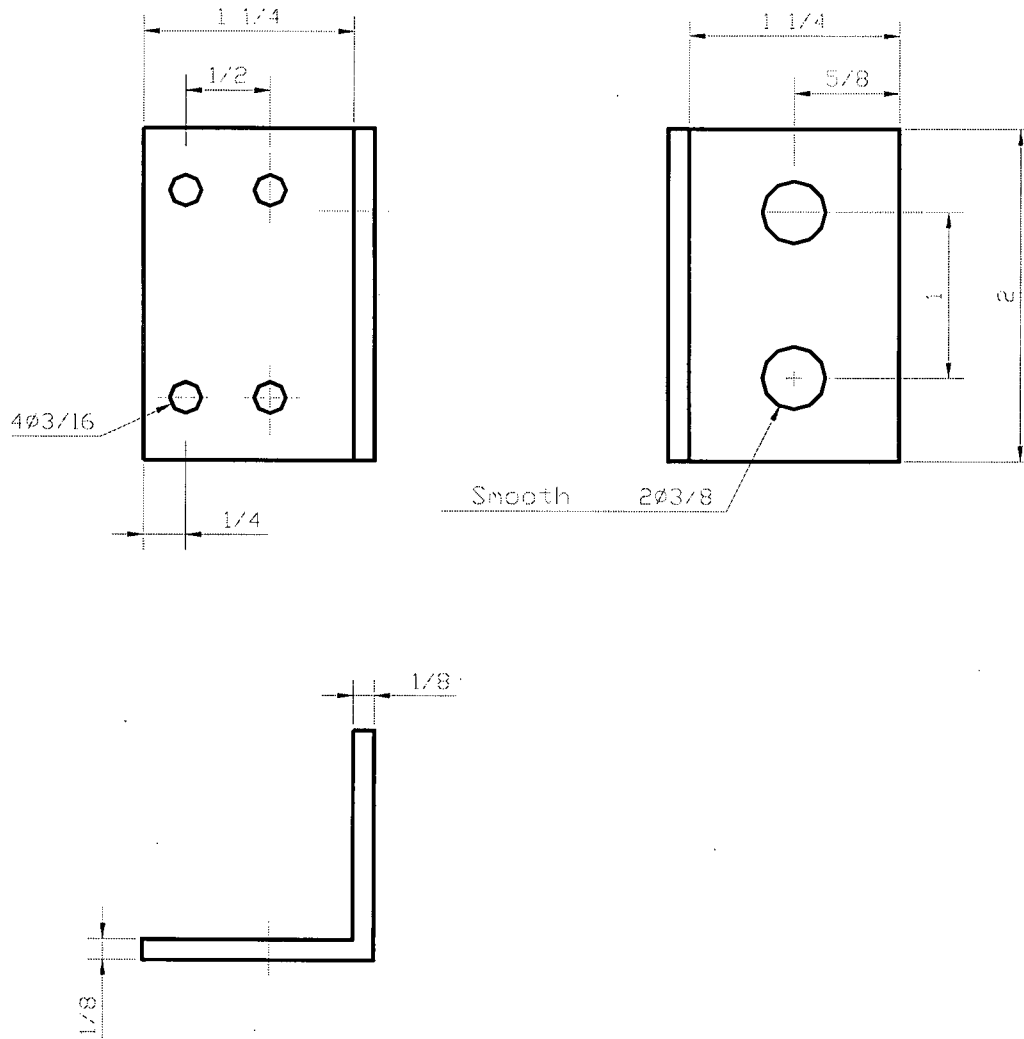


**Figure A-1 A half of crosswise grip with smooth holes (unit: inch)**

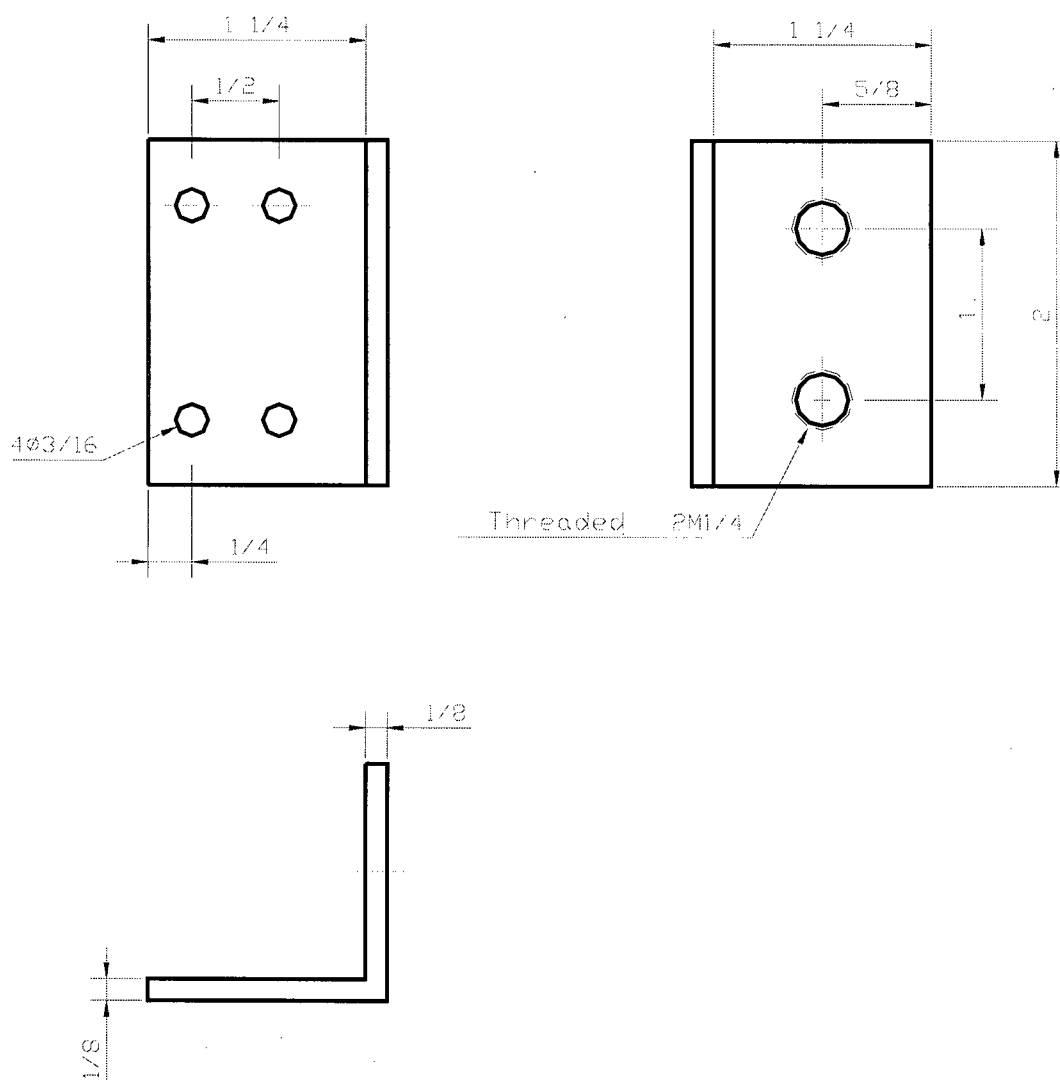


Figure A-2 A half of crosswise grip with threaded holes (unit: inch)